Summer 8-2020

Characterization of Human Pyrroline-5-Carboxylate Reductase Enzymes Responsible for L-Proline Biosynthesis

Sagar Patel
University of Nebraska - Lincoln, sagar.patel1185@huskers.unl.edu

CHARACTERIZATION OF HUMAN PYRROLINE-5-CARBOXYLATE REDUCTASE ENZYMES RESPONSIBLE FOR L-PROLINE BIOSYNTHESIS

by

Sagar Mahendrakumar Patel

A DISSERTATION

Presented to the Faculty of

The Graduate College at the University of Nebraska

In Partial Fulfillment of Requirements

For the Degree of Doctor of Philosophy

Major: Biochemistry

Under the Supervision of Professor Donald F. Becker

Lincoln, Nebraska

August, 2020

CHARACTERIZATION OF HUMAN PYRROLINE-5-CARBOXYLATE REDUCTASE ENZYMES RESPONSIBLE FOR L-PROLINE BIOSYNTHESIS

Sagar M. Patel, Ph.D.

University of Nebraska, 2020

Advisor: Donald F. Becker

Pyrroline-5-carboxylate reductases (EC 1.5.1.2) are important housekeeping enzymes of L-proline biosynthesis, which generate L-proline and influence redox cycling of NAD(P)H/NAD(P)$^+$ to support cellular growth in all domains of life. Structural evidence from X-ray crystal structures of HsPYCR1 (PDB codes 5UAT, 5UAU, and 5UAV) shows both NADPH bound in the N-terminal Rao-Rossmann fold motif and an important hydrogen bond or proton donor role for Thr238 with L-P5C. A Thr238Ala mutation results in a 10-fold loss in catalytic efficiency with varied L-P5C relative to the wild-type enzyme, thus indicating an important role for Thr238 during catalysis. For HsPYCR2, Henri-Michaelis-Menten kinetic analysis reveals a 164-fold loss in catalytic efficiency for the Arg119Cys mutant, with varied L-P5C and fixed NADH, relative to wild-type HsPYCR2. Profound effects on thermostability and secondary structure characteristics of the Arg251Cys mutant were determined by thermal shift assays and circular dichroism spectroscopy, respectively. Product(s) inhibition kinetics collectively indicate NADP$^+$ and NAD$^+$ are mixed noncompetitive inhibitors against NADPH and NADH, respectively, whereas L-proline is a competitive inhibitor against L-P5C. Taken together, these findings support a sequential-

ordered binding enzyme mechanism of L-P5C binding first followed by NAD(P)H-binding.

The ability of HsPYCR1 and 2 for reverse enzyme activity was observed with L-T4C as the reducing substrate. Structural evidence of a HsPYCR1—L-T4C binary complex, reverse direction saturation kinetics for both isozymes, and inhibition kinetics showing L-proline as a competitive inhibitor versus L-T4C, all indicate L-T4C shares the same active site as L-proline. Upon further evaluation of reverse direction reactions, we discovered association reactions between tris(alkyl)phosphine compounds and NAD^+. Stopped-flow absorbance kinetics demonstrated rapid and reversible NAD^+—tris(alkyl)phosphine nonenzymatic reactions with optimal absorbance at 334 nm for the reaction product. NMR spectroscopy identified a covalent adduct between the phosphorus of tris(2-carboxyethyl)phosphine or tris(3-hydroxypropyl)phosphine interacting at the C4 of the dihydronicotinamide ring of NAD^+. Ultimately, this thesis dissertation provides strong structural and kinetic insights into human pyrroline-5-carboxylate reductase enzymes responsible for L-proline biosynthesis.

DEDICATION

To my parents, Mahendra and Jyotsna, and to my brother, Vishal. Thank you all for your continued support and precious encouragement throughout this doctoral training experience.

ACKNOWLEDGEMENTS

I formally acknowledge my thesis supervisory committee: Donald F. Becker, Ph.D.; Mark A. Wilson, Ph.D.; Oleh Khalimonchuk, Ph.D.; Jiri Adamec, Ph.D.; and Liangcheng Du, Ph.D. I deeply appreciate the sound guidance and understanding these faculty advisors provided to me over the years. In particular, I am grateful to Dr. Becker for his patience, encouragement, compassion, friendly advice, and support for matters both in and out of the lab. I have been privileged and honored in this Ph.D. training experience under the keen and insightful tutelage of Dr. Becker.

I extend thanks to Dr. Javier Seravalli, Dr. David Holding, Dr. Thomas Clemente, Dr. Daniel Schachtman, Dr. Jaekwon Lee, Dr. Paul Black, and Dr. Concetta C. DiRusso, Dr. Thomas G. Smith, and Dr. Martha Morton (all from University of Nebraska-Lincoln), Dr. John J. Tanner (University of Missouri-Columbia), as well as Dr. Stephen J. Mayclin and Dr. Thomas E. Edwards (Seattle Structural Genomics Center for Infectious Disease). Throughout the years, I appreciate Dr. Seravalli's assistance for application and analysis of HPLC-MS of samples, access to the Holding lab's mini plate spinner and MyiQ Single-Color Real-Time PCR Detection System for fluorescent-based protein thermal shift assays, access to both the Clemente lab's and the Schachtman lab's freeze-dry vacuum lyophilization systems for concentration of purified proteins, access to the Lee lab's automated glass test tube fraction collector, and access to both the Black lab's and DiRusso lab's Synergy 2 Multi-Mode Plate-

Reader. Dr. Thomas G. Smith and Dr. Martha Morton were instrumental in performing all the NMR spectroscopy experiments and data analysis of the reaction product of NAD^+ and tris(alkyl)phosphine compounds. In the study pertaining to those NMR experiments, the X-ray crystal structure of SDR soaked with 5 mM $NADP^+$ and 1 mM TCEP was graciously provided by Dr. Stephen J. Mayclin and Dr. Thomas E. Edwards. The [pKA8H/HsPYCR2] expression vector construct for our recombinant protein purifications was kindly provided by former Becker lab member Dr. Xinwen Liang (currently at Penn State University). Special thanks is given to former and current members of the Becker lab (Dr. Shelbi L. Christgen, Dr. Benjamin W. Arentson, Dr. Lu Zhang, Brandon Thelen, Yizi Mao, and Huong Trinh), to Dr. George Grady, and to members of the Tanner lab (Dr. Kyle Stiers, Emily M. Christensen, Ashley C. Campbell, Dr. David A. Korasick, and Dr. Li-Kai Liu) for their guidance, discussions, and support with experiments and data analysis.

Additionally, I extend sincere thanks to members of the Redox Biology Center, the Department of Biochemistry, and the Center for Biotechnology in the Beadle Center here at the University of Nebraska-Lincoln. Specifically, the following administrative staff members: Paula Adams, Carol Hegel, Diana Bonham, Rita Yeggy, Leann Galusha, Lisa Vonfeldt, Teresa Loseke, Leslie Acree, Alan Muthersbaugh, and Andrew Loseke, have provided significant aid and clarification of matters with administrative documents, lab item ordering and shipping procedures, Beadle Center conference room reservations, and dealing with outside vendors for lab products and services. Simply put, I have grown

more as a conscientious and responsible scientist well aware of his lab resources due to the unwavering support from these administrative staff members.

TABLE OF CONTENTS

Page

LIST OF ABBREVIATIONS

5'-HIAAL	5-hydroxyindole-3-acetic acid
5'-HITCA	(4R)-2-[3'-(5'-hydroxyindoly1)-methyl]-1,3-thiazolidine-4-carboxylic acid
5-HT	5-hydroxytryptamine
CD	circular dichroism
CNS	central nervous system
CoQ1	coenzyme Q1
CSF	cerebrospinal fluid
DL-T2C	DL-thiazolidine-2-carboxylate
DTT	dithiothreitol
EDTA	ethylenediamine tetraacetic acid
ESC	embryonic stem cell
ETC	electron-transport chain
GSALDH	L-glutamic-γ-semialdehyde dehydrogenase, a.k.a. ALDH4A1
HEPES	2-[4(2-hydroxyethyl)piperazin-1-yl] ethanesulfonic acid
HPLC	high performance liquid chromatography
HsPYCR1 or 2	human pyrroline-5-carboxylate reductase 1 or 2
IPTG	isopropyl β-D-thiogalactopyranoside
KSHV	Kaposi's sarcoma-associated herpesvirus
L-Cys	L-cysteine
L-GSAL	L-glutamic-γ-semialdehyde
L-P5C	L-Δ^1-pyrroline-5-carboxylate
L-Pro	L-proline

L-T4C	L-thiazolidine-4-carboxylate, a.k.a. L-thioproline
L-THFA	L-tetrahydro-2-furoic acid
$NAD(P)^+$	oxidized dihydronicotinamide adenine dinucleotide (phosphate)
NAD(P)H	reduced dihydronicotinamide adenine dinucleotide (phosphate)
NMR	nuclear magnetic resonance
o-AB	*o*-aminobenzaldehyde
OAT	L-ornithine aminotransferase
P5CS	L-Δ^1-pyrroline-5-carboxylate synthetase, a.k.a. ALDH18A1
PBS	phosphate buffered saline
PMSF	phenylmethylsulfonyl fluoride
PRODH	L-proline dehydrogenase
PYCR	L-Δ^1-pyrroline-5-carboxylate reductase
RNS	reactive nitrogen species
ROS	reactive oxygen species
SDR	short-chain dehydrogenase/reductase
TCEP	tris(2-carboxyethyl)phosphine
THPP	tris(3-hydroxypropyl)phosphine
TPCOR	L-thiazolidine-4-and-L-pyrroline-5-carboxylate oxidoreductase
Tris	tris(hydroxymethyl)aminomethane
β-OG	β-octyl-D-glucopyranoside
HLD10	hypomyelinating leukodystrophy type 10

LC-ESI-MRM	liquid chromatography-electrospray ionization-multiple reaction monitoring

LIST OF FIGURES

Page

LIST OF TABLES

Page

Chapter 1

Introduction to L-proline biosynthesis in humans

INTRODUCTION

Biochemical and bioenergetic aspects of cellular metabolism rely upon the presence and function of proteins, which are assembled based on the cellular supply of amino acids. Among the 20 common amino acids in humans, L-proline is distinguished as being the only proteinogenic imino acid due to both its amine nitrogen and its side chain covalently linked to the alpha carbon as a five-membered pyrrolidine ring. L-proline is a nonessential amino acid in humans with L-glutamate and L-arginine serving as the primary sources for de novo biosynthesis of L-proline as shown in Fig. 1.1.

In the 1960s, L-Δ^1-pyrroline-5-carboxylate reductase (PYCR) activity was characterized from animal sources such as rat and bovine tissues.[1] The reaction of PYCR was observed strongly favoring the direction of L-proline formation with little appreciable reversible activity.[1] It was then proposed that in mammals the reduction of L-glutamate to L-proline proceeds through a reaction pathway that is distinct from that of the oxidation of L-proline to L-glutamate (Fig. 1.1).[1] Over the years, structural and biochemical studies have confirmed that in human mitochondria, L-glutamate initially is reduced to L-glutamic-γ-semialdehyde (L-GSAL) by the bifunctional enzyme ALDH18A1 (synonymous with L-Δ^1-pyrroline-5-carboxylate synthetase (P5CS)), which possesses an ATP-dependent glutamate-5-kinase domain and a NAD(P)H-dependent L-glutamyl-γ-5-phosphate reductase domain (Fig. 1.1).[2] Upon nonenzymatic dehydration, the open-chain L-GSAL molecule undergoes ring closure to form L- Δ^1-pyrroline-5-carboxylate (L-

P5C). Next, the NAD(P)H-dependent PYCR enzyme functions to reduce L-P5C into L-proline (Fig. 1.1).[3]

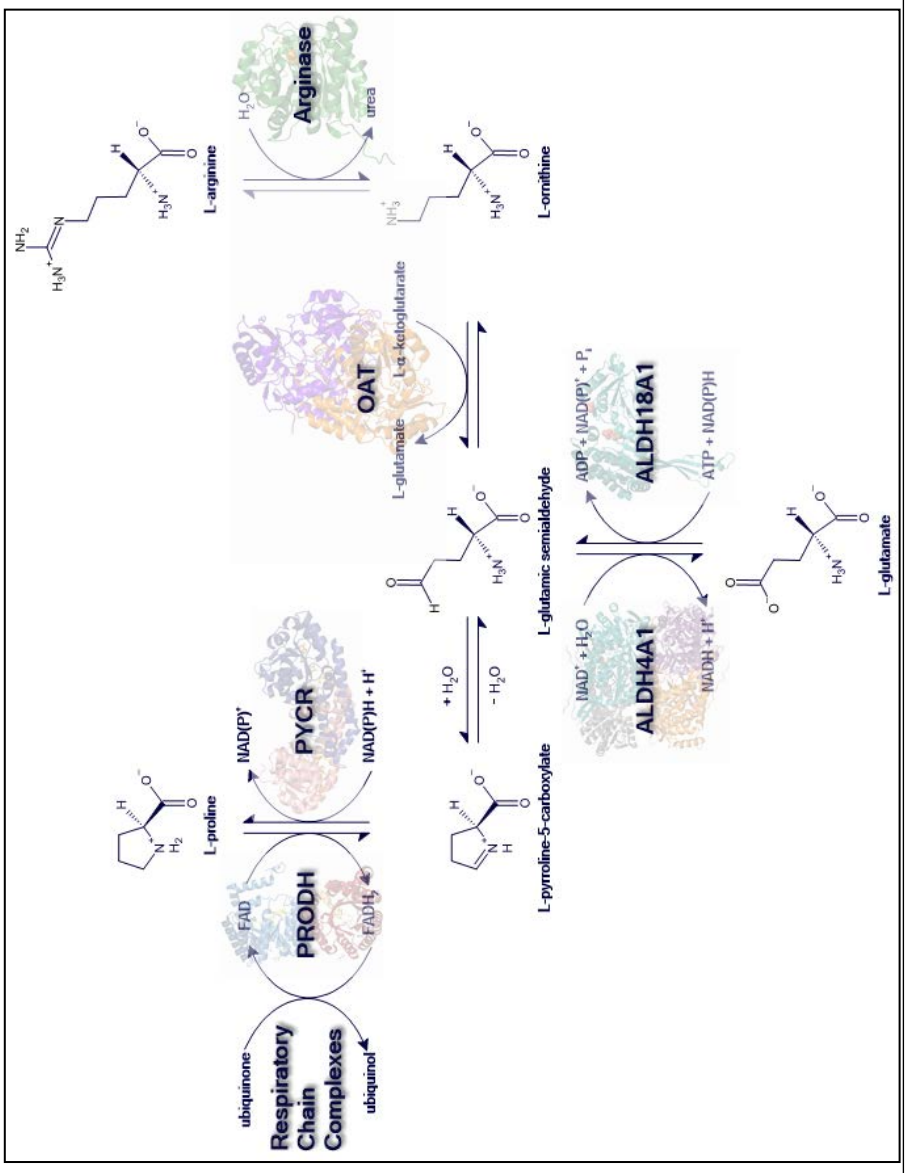

Figure 1.1. Enzymatic reactions of L-proline and L-arginine metabolism in the mitochondrion. Background translucent protein images are PyMol renderings of following X-ray crystal structures: dimeric TtPRODH (PDB: 2EKG), dimeric HsPYCR1 (PDB: 5UAV), tetrameric HsALDH4A1 (PDB: 4OE5), monomer of L-glutamyl-γ-5--phosphate reductase domain of HsALDH18A1 (PDB: 2H5G), dimeric HsOAT (PDB: 2OAT), and monomeric human Arginase (PDB: 6Q92).

A distinct pathway exists for the conversion of L-proline back to L-glutamate. The first step of L-proline oxidation into L-P5C is catalyzed by the FAD-dependent enzyme L-proline dehydrogenase (PRODH).[4] L-P5C is then dehydrated nonenzymatically into L-GSAL, which is subsequently oxidized by the NAD^+-dependent enzyme ALDH4A1 (synonymous with L-GSAL dehydrogenase (GSALDH)) to yield L-glutamate.[4] L-glutamate itself has several fates, some of which include enzymatic conversion into L-glutamine, entry into the citric acid cycle as L-α-ketoglutarate, or directly functioning as an excitatory amino acid neurotransmitter in the central nervous system. All of these potential fates for L-glutamate explain how L-proline metabolism is linked to overarching processes of central metabolism such as bioenergetics, anaplerotic reactions replenishing citric acid cycle intermediates, and cell signaling.[5]

The coupling of L-proline metabolism to regulatory networks suggests a versatility beyond that of the L-proline requirement for protein synthesis. For instance, Hancock et al. (2016) utilized a PRODH-expressing DLD colorectal cancer cell model and mouse mitochondria to demonstrate that PRODH mediates the transfer of electrons from L-proline directly to coenzyme Q1 (CoQ1).[6] The subsequent electron transfer from CoQ1 to the electron-transport chain (ETC) Complexes III and IV occurs during acute nutrient deprivation.[6] Elevated PRODH expression can eventually lead to downregulation of ETC component proteins through production of reactive oxygen species (ROS).[6] These findings corroborate earlier observations that the initial catabolism of L-proline by PRODH modulates cellular bioenergetics and ATP generation in vivo. In a study by Liu et al. (2015) using a P493 human B lymphoma cancer cell line,

genetic knockdown of P5CS and all three PYCRs hindered the oxidative arm of the pentose phosphate pathway as evidenced by a marked decrease in both NAD^+ and $NADP^+$ levels that were not rescued by exogenous treatment with L-proline or L-P5C.[7] Thus, it seems that an important function of L-proline biosynthetic enzymes is to drive cellular bioenergetics through the pentose phosphate pathway via shuttling of $NAD(P)^+$, not necessarily for ATP generation but to help provide the cell with ribose-5-phosphate for the synthesis of pyridine nucleotides. In the context of cell signaling, D'Aniello et al. (2015) provide the first evidence that mouse embryonic stem cell (ESC) identity depends on the autoregulatory loop between L-Pro biosynthetic enzymes (P5CS and PYCR1) and the Gcn2-Eif2α-Atf4 amino acid starvation response pathway.[8] Herein, the authors concluded that L-Pro starvation, either intrinsic or pharmacological inhibition of prolyl-tRNA synthetase by halofuginone, activates autophagy and signals massive apoptosis.[8] Hence, L-Pro is a multifaceted imino acid that influences aspects of cellular bioenergetics and cell signaling with the aid of its L-proline metabolic machinery.

The other primary source for L-proline biosynthesis is L-arginine (Fig. 1.1). Both groups Mepham et al. (1966) and Yip et al. (1972) confirmed in rats and goats that the enzymatic composition of the lactating mammary gland is poised for the metabolic conversion of L-arginine into L-proline.[9,10] Building upon those findings, structural and biochemical studies have established that in human mitochondria, L-arginine initially undergoes catalytic hydrolysis by Mn^{2+}-dependent arginase to yield urea and L-ornithine.[11] Next, two half-transamination reactions catalyzed by pyridoxal-5-phosphate-dependent enzyme L-ornithine

aminotransferase (OAT) converts L-ornithine and L-α-ketoglutarate substrates into L-GSAL and L-glutamate products, respectively.[12] This intersection at L-GSAL reveals how L-arginine metabolism contributes to L-proline synthesis. Within the mammalian system, glucocorticoid hormones, such as cortisol and corticosterone, differentially regulate intestinal L-proline and L-ornithine production from L-glutamine and L-arginine sources to provide substrates for the synthesis of extracellular matrix proteins, i.e. collagen, and of polyamines.[13]

CLINICAL CORRELATIONS WITH ALTERED PYCR EXPRESSION AND FUNCTION

In humans, altered PYCR expression and function has been associated with several cancers and tumor growths, neurodegenerative diseases, and cutaneous and connective tissue diseases. Humans have three genes encoding isozymes PYCR1, PYCR2, and PYCRL (a.k.a. PYCR3).[14] Isozymes PYCR1 and PYCR2 are mitochondrial whereas PYCRL is cytosolic, and they have varied sensitivities to product inhibition, which contributes to their specialized function in proline metabolism.[14] The functional consequences of depleting PYCR1, PYCR2, and PYCRL have implicated proline metabolism in various pathologies, including cancers like melanoma, breast cancer, prostate cancer, esophageal tumors, lung metastasis, and Kaposi's sarcoma-associated herpesvirus (KSHV) – mediated tumorigenesis, along with cases of acute pancreatitis, hyperprolinemia, schizophrenia, hypomyelinating leukodystrophy type 10 with microcephaly, and cutis laxa.[5,15,16] Human PYCR1 and 2 (HsPYCR1 and 2) have been separately implicated in specific cancers: non-small cell lung cancer, viral-related hepatocellular carcinoma, papillary renal cell carcinoma, melanoma, breast and

prostate cancers, esophageal squamous cell carcinoma, KSHV – mediated tumorigenesis, lung adenocarcinoma, and colorectal cancer.[15,17,18,19,20,7,21,22,23,24,25] Also, studies have shown all three human PYCR isozymes are transcriptionally up-regulated by the *c-MYC* oncogene in many types of cancers.[5,15,7] A study by Olivares et al. (2017) found that the collagen in the extracellular matrix of the tumor microenvironment of pancreatic ductal adenocarcinoma cells serves as a critical nutrient reserve of L-proline that fuels the citric acid cycle and prolongs tumor cell survival under restrictive nutrient conditions.[26] Thus, L-proline biosynthesis promotes tumorigenesis particularly through the activity of HsPYCR1 and 2.

Another set of pathologies linked to L-proline biosynthesis concerns neurodegenerative and psychiatric diseases. For instance, animal-based studies have revealed that alterations in the reactions of L-arginine and L-proline metabolism that are involved in neurotransmission have been identified as strong contributors to the progression of schizophrenia.[27] In Zaki et al.'s (2016) study on PYCRs in lethal microcephaly and failure to thrive pathologies, HsPYCR2 was proposed to promote redox cycling of NAD(P)H/NAD(P)$^+$ to support cellular growth and neuronal development.[28] In a landmark study, Nakayama et al. (2015) found that in human patients affected with specific neurological phenotypes of hypomyelination and microcephaly, there was a strong genetic linkage with individual HsPYCR2 missense mutations R119C and R251C.[29] Despite the phenotypic overlap between autosomal recessive disorders of HsPYCR1 and 2 mutations in terms of microcephaly, global developmental delay, and joint hyperlaxity, mutations in HsPYCR1 uniquely lead to cutis laxa type IIB

(OMIM # 612940)[30,31] whereas mutations in HsPYCR2 uniquely lead to genetic hypomyelinating leukodystrophy type 10 with microcephaly (OMIM # 616420).[28,29,32] Therefore, dysfunctions in HsPYCR2 are more strongly associated with neurodegenerative diseases than dysfunctions in HsPYCR1.

Cutaneous and connective tissue diseases have been associated with HsPYCR1 dysfunctions. Collagen is a structural scaffold protein found in all connective tissue, bone, and the extracellular matrix of the human body. The most abundant amino acid in collagen is L-proline, thus collagen is often considered as a L-proline reservoir. Studies on the role of collagen in fibrotic diseases and tumorigenesis are therefore often linked to L-proline metabolism.[33] In a study by Reversade et al. (2009), cultured skin fibroblasts were examined from individuals with mutations in HsPYCR1 and afflicted with autosomal recessive cutis laxa.[31] The mutations in HsPYCR1 were shown to cause aberrant mitochondrial morphology and dysfunction.[31] These observations provided new insights into how HsPYCR1 deficiency could contribute to progeroid changes in connective tissues besides disrupting L-proline biosynthesis.[31] In addition to L-proline biosynthesis, important research has focused on understanding post-translational modifications of L-proline in collagen. Prolyl-4-hydroxylase and prolyl-3-hydroxylase have a non-heme iron center that catalyzes the addition of an oxygen atom at the C4 and C3 positions of the pyrrolidine ring of peptidyl L-proline, respectively, using L-α-ketoglutarate and O_2. Early work by Englard et al. (1986), involved in vivo studies supporting a mechanism proposed by Hanauske-Abel et al. (1982) in which L-ascorbate from the endoplasmic reticulum lumen acts as an effective reductant of the iron center to replenish the ferrous form after

each catalytic cycle of the prolyl hydroxylase enzymes.[34]

SUMMARY

Although L-proline is a nonessential amino acid in humans, its importance spans the realms of protein synthesis, bioenergetics, structural scaffolding in the extracellular environment, and cell signaling.[5] De novo biosynthesis of L-proline stems from two major sources: L-glutamate and L-arginine. Dysfunctional expression or activity of HsPYCR1 and 2 have been linked to human pathological conditions including various cancers and tumors, neurodegenerative and psychiatric disorders, and cutaneous and connective tissue diseases. Taken together, this dissertation aims to provide a clear understanding of the molecular mechanisms of L-proline biosynthesis with structural and functional in vitro characterization of human PYCR1 and PYCR2.

REFERENCES

[1] PEISACH, J., and STRECKER, H. J. (1962) The interconversion of glutamic acid and proline. V. The reduction of delta 1-pyrroline-5-carboxylic acid to proline, *J Biol Chem 237*, 2255-2260.

[2] Phang, J. M. (1985) The regulatory functions of proline and pyrroline-5-carboxylic acid, *Curr Top Cell Regul 25*, 91-132.

[3] Christensen, E. M., Patel, S. M., Korasick, D. A., Campbell, A. C., Krause, K. L., Becker, D. F., and Tanner, J. J. (2017) Resolving the cofactor-binding site in the proline biosynthetic enzyme human pyrroline-5-carboxylate reductase 1, *Journal of Biological Chemistry 292*, 7233-7243.

[4] Hu, C. A., Bart Williams, D., Zhaorigetu, S., Khalil, S., Wan, G., and Valle, D. (2008) Functional genomics and SNP analysis of human genes encoding proline metabolic enzymes, *Amino Acids 35*, 655-664.

[5] Phang, J. M. (2019) Proline Metabolism in Cell Regulation and Cancer Biology: Recent Advances and Hypotheses, *Antioxid Redox Signal 30*, 635-649.

[6] Hancock, C. N., Liu, W., Alvord, W. G., and Phang, J. M. (2016) Co-regulation of mitochondrial respiration by proline dehydrogenase/oxidase and succinate, *Amino Acids 48*, 859-872.

[7] Liu, W., Hancock, C. N., Fischer, J. W., Harman, M., and Phang, J. M. (2015) Proline biosynthesis augments tumor cell growth and aerobic glycolysis: involvement of pyridine nucleotides, *Sci Rep 5*, 17206.

[8] D'Aniello, C., Fico, A., Casalino, L., Guardiola, O., Di Napoli, G., Cermola, F., De Cesare, D., Tatè, R., Cobellis, G., Patriarca, E. J., and Minchiotti, G. (2015) A novel autoregulatory loop between the Gcn2-Atf4 pathway and l-Proline metabolism controls stem cell identity, *Cell Death Differ 22*, 1234.

[9] Mepham, T. B., and Linzell, J. L. (1967) Urea formation by the lactating goat mammary gland, *Nature 214*, 507-508.

[10] Yip, M. C., and Knox, W. E. (1972) Function of arginase in lactating mammary gland, *Biochem J 127*, 893-899.

[11] Grobben, Y., Uitdehaag, J. C., Willemsen-Seegers, N., Tabak, W. W., de Man, J., Buijsman, R. C., and Zaman, G. J. (2020) Structural insights into human Arginase-1 pH dependence and its inhibition by the small molecule inhibitor CB-1158, *Journal of Structural Biology: X 4*, 100014.

[12] Storici, P., Capitani, G., Müller, R., Schirmer, T., and Jansonius, J. N. (1999) Crystal structure of human ornithine aminotransferase complexed with the highly specific and potent inhibitor 5-fluoromethylornithine, *J Mol Biol 285*, 297-309.

[13] Flynn, N. E., Bird, J. G., and Guthrie, A. S. (2009) Glucocorticoid regulation of amino acid and polyamine metabolism in the small intestine, *Amino Acids 37*, 123-129.

[14] De Ingeniis, J., Ratnikov, B., Richardson, A. D., Scott, D. A., Aza-Blanc, P., De, S. K., Kazanov, M., Pellecchia, M., Ronai, Z. e., Osterman, A. L., and Smith, J. W. (2012) Functional Specialization in Proline Biosynthesis of Melanoma, *PLoS ONE 7*, e45190 EP -.

[15] Choi, U. Y., Lee, J. J., Park, A., Zhu, W., Lee, H. R., Choi, Y. J., Yoo, J. S., Yu, C., Feng, P., Gao, S. J., Chen, S., Eoh, H., and Jung, J. U. (2020) Oncogenic human herpesvirus hijacks proline metabolism for tumorigenesis, *Proc Natl Acad Sci U S A*.

[16] Iyer, S., Park, M. J., Moons, D., Kwan, R., Liao, J., Liu, L., and Omary, M. B. (2017) Clusterin and Pycr1 alterations associate with strain and model differences in susceptibility to experimental pancreatitis, *Biochem Biophys Res Commun 482*, 1346-1352.

[17] Guo, L., Cui, C., Zhang, K., Wang, J., Wang, Y., Lu, Y., Chen, K., Yuan, J., Xiao, G., Tang, B., Sun, Y., and Wu, C. (2019) Kindlin-2 links mechano-environment to proline synthesis and tumor growth, *Nat Commun 10*, 845.

[18] Gao, Q., Zhu, H., Dong, L., Shi, W., Chen, R., Song, Z., Huang, C., Li, J., Dong, X., Zhou, Y., Liu, Q., Ma, L., Wang, X., Zhou, J., Liu, Y., Boja, E., Robles, A. I., Ma, W., Wang, P., Li, Y., Ding, L., Wen, B., Zhang, B., Rodriguez, H., Gao, D., Zhou, H., and Fan, J. (2019) Integrated Proteogenomic Characterization of HBV-Related Hepatocellular Carcinoma, *Cell 179*, 1240.

[19] Wang, Q. L., and Liu, L. (2019) PYCR1 is Associated with Papillary Renal Cell Carcinoma Progression, *Open Med (Wars) 14*, 586-592.

[20] Ou, R., Zhang, X., Cai, J., Shao, X., Lv, M., Qiu, W., Xuan, X., Liu, J., Li, Z., and Xu, Y. (2016) Downregulation of pyrroline-5-carboxylate reductase-2 induces the autophagy of melanoma cells via AMPK/mTOR pathway, *Tumour Biol 37*, 6485-6491.

[21] Sun, C., Li, T., Song, X., Huang, L., Zang, Q., Xu, J., Bi, N., Jiao, G., Hao, Y., Chen, Y., Zhang, R., Luo, Z., Li, X., Wang, L., Wang, Z., Song, Y., He, J., and Abliz, Z. (2019) Spatially resolved metabolomics to discover tumor-associated metabolic alterations, *Proc Natl Acad Sci U S A 116*, 52-57.

[22] Zeng, T., Zhu, L., Liao, M., Zhuo, W., Yang, S., Wu, W., and Wang, D. (2017) Knockdown of PYCR1 inhibits cell proliferation and colony formation via cell cycle arrest and apoptosis in prostate cancer, *Med Oncol 34*, 27.

[23] Yan, K., Xu, X., Wu, T., Li, J., Cao, G., Li, Y., and Ji, Z. (2019) Knockdown of PYCR1 inhibits proliferation, drug resistance and EMT in colorectal cancer cells by regulating STAT3-Mediated p38 MAPK and NF-κB signalling pathway, *Biochem Biophys Res Commun 520*, 486-491.

[24] She, Y., Mao, A., Li, F., and Wei, X. (2019) P5CR1 protein expression and the effect of gene-silencing on lung adenocarcinoma, *PeerJ 7*, e6934.

[25] Ding, Z., Ericksen, R. E., Escande-Beillard, N., Lee, Q. Y., Loh, A., Denil, S., Steckel, M., Haegebarth, A., Wai Ho, T. S., Chow, P., Toh, H. C., Reversade, B., Gruenewald, S., and Han, W. (2020) Metabolic pathway analyses identify proline biosynthesis pathway as a promoter of liver tumorigenesis, *J Hepatol 72*, 725-735.

[26] Olivares, O., Mayers, J. R., Gouirand, V., Torrence, M. E., Gicquel, T., Borge, L., Lac, S., Roques, J., Lavaut, M. N., Berthezène, P., Rubis, M., Secq, V., Garcia, S., Moutardier, V., Lombardo, D., Iovanna, J. L., Tomasini, R., Guillaumond, F., Vander Heiden, M. G., and Vasseur, S. (2017) Collagen-derived proline promotes pancreatic ductal adenocarcinoma cell survival under nutrient limited conditions, *Nat Commun 8*, 16031.

[27] Humer, E., Probst, T., and Pieh, C. (2020) Metabolomics in Psychiatric Disorders: What We Learn from Animal Models, *Metabolites 10*.

[28] Zaki, M. S., Bhat, G., Sultan, T., Issa, M., Jung, H. J., Dikoglu, E., Selim, L., G. Mahmoud, I., Abdel-Hamid, M. S., and Abdel-Salam, G. (2016) PYCR2 mutations cause a lethal syndrome of microcephaly and failure to thrive, *Annals of neurology 80*, 59-70.

[29] Nakayama, T., Al-Maawali, A., El-Quessny, M., Rajab, A., Khalil, S., Stoler, Joan M., Tan, W.-H., Nasir, R., Schmitz-Abe, K., Hill, R. S., Partlow, Jennifer N., Al-Saffar, M., Servattalab, S., LaCoursiere, Christopher M., Tambunan, Dimira E., Coulter, Michael E., Elhosary, Princess C., Gorski, G., Barkovich, A. J., Markianos, K., Poduri, A., and Mochida, Ganeshwaran H. (2015) Mutations in PYCR2, Encoding Pyrroline-5-Carboxylate Reductase 2, Cause Microcephaly and Hypomyelination, *The American Journal of Human Genetics 96*, 709-719.

[30] Kniffin, C. L., and O'Neill, M. J. F. Online Mendelian Inheritance in Man, OMIM. CUTIS LAXA, AUTOSOMAL RECESSIVE, TYPE IIB; ARCL2B. MIM Number: 612940: 06/15/2018., Johns Hopkins University, Baltimore, MD. Online <https://omim.org/entry/612940>.

[31] Reversade, B., Escande-Beillard, N., Dimopoulou, A., Fischer, B., Chng, S. C., Li, Y., Shboul, M., Tham, P. Y., Kayserili, H., Al-Gazali, L., Shahwan, M., Brancati, F., Lee, H., O'Connor, B. D., Schmidt-von Kegler, M., Merriman, B., Nelson, S. F., Masri, A., Alkazaleh, F., Guerra, D., Ferrari, P., Nanda, A., Rajab, A., Markie, D., Gray, M., Nelson, J., Grix, A., Sommer, A., Savarirayan, R., Janecke, A. R., Steichen, E., Sillence, D., Hausser, I., Budde, B., Nürnberg, G., Nürnberg, P., Seemann, P., Kunkel, D., Zambruno, G., Dallapiccola, B., Schuelke, M., Robertson, S., Hamamy, H., Wollnik, B., Van Maldergem, L., Mundlos, S., and Kornak, U. (2009) Mutations in PYCR1 cause cutis laxa with progeroid features, *Nat Genet 41*, 1016-1021.

[32] Kniffin, C. L. Online Mendelian Inheritance in Man, OMIM. LEUKODYSTROPHY, HYPOMYELINATING, 10; HLD10. MIM Number: 616420: 10 /27/2016., John Hopkins University., Baltimore, MD. Online <https://omim.org/entry/616420>.

[33] Vasta, J. D., and Raines, R. T. (2018) Collagen Prolyl 4-Hydroxylase as a Therapeutic Target, *J Med Chem 61*, 10403-10411.

[34] Englard, S., and Seifter, S. (1986) The biochemical functions of ascorbic acid, *Annu Rev Nutr 6*, 365-406.

Chapter 2

Kinetic Analysis of wild-type HsPYCR1 and Thr238 Active Site Mutant

Portions of this research were originally published in the Journal of Biological Chemistry:

Christensen, E. M., Patel, S. M., Korasick, D. A., Campbell, A. C., Krause, K. L., Becker, D. F., and Tanner, J. J. Resolving the Cofactor Binding Site in the Proline Biosynthetic Enzyme Human Pyrroline-5-Carboxylate Reductase 1. J. Biol. Chem. (2017); 292 (17): 7233-7243.

ABSTRACT

Pyrroline-5-carboxylate reductase (PYCR) is the final enzyme in L-proline biosynthesis, catalyzing the NAD(P)H-dependent reduction of L-pyrroline-5-carboxylate (L-P5C) into L-proline (L-Pro). Mutations in the *PYCR1* gene alter mitochondrial function and cause the connective tissue disorder cutis laxa. HsPYCR1 is overexpressed in multiple cancers, and the HsPYCR1 knock-out suppresses tumorigenic growth, suggesting that HsPYCR1 is a potential cancer target. However, inhibitor development has been stymied by limited mechanistic details for the enzyme, particularly in light of a previous crystallographic study that placed the cofactor-binding site in the C-terminal domain rather than the anticipated Rao-Rossmann fold of the N-terminal domain. To fill this gap, we report X-ray crystallographic, sedimentation-velocity, and kinetics data for human PYCR1. Structures of the binary complexes of HsPYCR1 with NADPH or L-proline determined at 1.9 Å resolution provide insight into cofactor and substrate recognition. We see NADPH bound to the Rao-Rossmann fold, over 25 Å from the previously proposed C-terminal site. The 1.85 Å resolution structure of a ternary complex containing NADPH and an L-P5C/L-Pro analog, namely L-tetrahydro-2-furoic acid (L-THFA), provides a model of the Michaelis complex

formed during hydride transfer. Sedimentation velocity shows that PYCR1 forms a concentration-dependent decamer in solution, consistent with the pentamer-of-dimers assembly seen crystallographically. Steady-state kinetic and mutational analysis along with product inhibition kinetic analyses confirmed several features seen in the crystal structure, including the importance of a hydrogen bond between Thr238 and the substrate as well as limited cofactor discrimination between NADPH and NADH.

INTRODUCTION

L-proline, a unique imino acid that lacks a primary amino group, is a key building block of proteins and plays an important role in stress protection and redox balance of cells across multiple kingdoms of life.[1,2,3] From a biosynthetic standpoint, the two biological sources of L-glutamate and L-arginine converge on enzyme L-pyrroline-5-carboxylate (L-P5C) reductase (P5CR, EC 1.5.1.2), which catalyzes the final reduction of L-P5C into L-proline (L-Pro) using NAD(P)H. In humans, P5CR is known as PYCR. The human genome contains three homologous PYCR genes, PYCR1, PYCR2, and PYCRL (also known as PYCR3). The various human PYCR (HsPYCR) isoforms have specialized roles in L-Pro biosynthesis and different subcellular localizations. A study of PYCRs in melanoma cells showed that both HsPYCR1 and 2 function primarily in the L-glutamate-to-L-proline pathway, whereas HsPYCRL functions mainly in the L-arginine-to-L-proline pathway.[4] HsPYCR1 and 2 localize to mitochondria, whereas HsPYCRL is cytosolic.[4,5] Other studies have shown that HsPYCR1 and 2 are recoverable from the cytosol, suggesting the possibility that the enzymes associate with the outer mitochondrial membrane.[6]

HsPYCR has been implicated in various cancers and has emerged as a potential therapeutic target. A study of mRNA profiles from 1,981 tumors identified PYCR1 as one of the most consistently overexpressed metabolic genes across 19 different cancer types.[7] Additional studies highlight an abundance of HsPYCR1 in melanoma cells as compared with healthy melanocytes, indicating this enzyme as a potential therapeutic target in skin cancer treatment.[4,8] Similarly, depletion of PYCR1 in different types of cancers, such as breast, prostate, and renal cell carcinoma, is associated with diminished cell proliferation and tumorigenic growth.[4,9,10,11]

Deficiencies in PYCR are also linked to inherited metabolic disorders. Certain mutations in the PYCR1 gene cause the autosomal recessive connective tissue disorder cutis laxa.[5] The decrease in HsPYCR1 activity is thought to impair mitochondrial function, leading to developmental defects through increased apoptosis.[5] Mutations in the PYCR2 gene cause a developmental disorder of the brain characterized by microcephaly, hypomyelination, and reduced white matter.[12] As with cutis laxa, the pathogenicity of the disorder involves mitochondria-induced apoptosis in the central nervous system.[12]

Although X-ray crystal structures of P5CRs from microorganisms and a plant species have been characterized[13,14,15], before this work, only one X-ray structural study has been characterized and discussed previously on human P5CR. Fourteen years ago, Meng et al. (2006) reported 3.1 Å crystal structures of HsPYCR1 complexed with NADPH and NADH.[16] A major conclusion of that study was that the NAD(P)H cofactor binds to the C-terminal domain rather than in the canonical site within the N-terminal Rao-Rossmann fold domain.[16] This result is

notable because it contradicts other P5CR structures and departs from the accepted structure-function paradigm of Rao-Rossmann fold enzymes, which asserts that the cofactor binds to the N-termini of the strands of the Rao-Rossmann dinucleotide-binding fold.[17,18]

Herein we reexamine the structure of HsPYCR1 at high resolution to better establish the location of the active site and to elucidate the interactions responsible for cofactor and substrate recognition. X-ray crystal structures of binary complexes of HsPYCR1 with NADPH and L-Pro have been determined at 1.9 Å resolution. The structure of a ternary complex with NADPH and the L-P5C/L-Pro analog L-tetrahydro-2-furoic acid (L-THFA) has been obtained at 1.85 Å resolution. Furthermore, we present Furthermore, we present analytical ultracentrifugation analysis of PYCR1 in solution and steady-state kinetic data of the wild-type and active-site mutant enzymes for the forward reaction of L-P5C reduction into L-Pro, along with product inhibition kinetic analyses. In contrast to Meng et al.'s (2006) study, our electron density maps unequivocally identify the location of the cofactor-binding site and show that HsPYCR1 follows the canonical structure-function paradigm of Rao-Rossmann fold enzymes.

MATERIALS AND METHODS

Expression and purification of HsPYCR1

DNA encoding human mitochondrial PYCR1 transcript variant 1 (NCBI RefSeq number NP_001269209.1) in pET-24b(+) with codons optimized for expression in *Escherichia coli* was synthesized by GenScript Biotech Corp. The construct encodes residues 1–300 of the full-length 319-residue protein plus an N-terminal hexahistidine tag and tobacco etch virus protease cleavage site. This

construct was designed for enhanced crystallization based on unpublished PDB entry 2IZZ.

The HsPYCR1 construct was transformed into BL21(DE3)-competent *E. coli* cells and plated onto LB agar containing 50 µg/ml kanamycin. A starter culture of Luria broth medium, shaken overnight at 37 °C and 250 rpm, was used to inoculate two 1 L cultures. After 2 h of shaking at 37 °C and 250 rpm, the larger cultures were induced with 0.5 mM isopropyl thiogalactopyranoside and grown with continued shaking at 18 °C overnight. Centrifugation at 3,000 x g for 20 min at 4 °C was used to collect the cells, which were then resuspended in 50 mM HEPES, pH 7.8, 300 mM NaCl, 10 mM imidazole, and 5% (w/v) glycerol (buffer A). The resuspended pellet was stored at 80 °C until ready for purification.

A mixture of DNase I, lysozyme, and GoldBio ProBlock protease inhibitor mixture was added to thawed cells and stirred at 4 °C for 20 min. After lysing cells via sonication, cell debris was removed by centrifugation at 16,000 rpm for 1 h at 4 °C. The resulting supernatant was passed through a 0.45 µm Millex-HV syringe filter and loaded onto a 5 ml HisTrap Ni^{2+}-nitrilotriacetic acid column (GE Healthcare) pre-equilibrated in buffer A using an AKTA Pure chromatography instrument. The column was washed with buffer A supplemented with 30 mM imidazole and eluted with 300 mM imidazole. The fractions containing PYCR1 as determined by SDS-PAGE were collected and dialyzed at 4 °C overnight into dialysis buffer containing 300 mM NaCl, 2% (w/v) glycerol, 50 mM HEPES, pH 7.5. Following dialysis, the protein was concentrated to 5 ml using a centrifugal concentrator (Amicon Ultra-15) and then further purified on a HiLoad 16/600 Superdex 200 size-exclusion column (GE Healthcare) using a column buffer with

the same composition as the dialysis buffer. The His-tag was not removed.

Crystallization of HsPYCR1, crystal soaking, and X-ray diffraction data collection

Experimental conditions for growing crystals of HsPYCR1, soaking them with ligands, and X-ray diffraction of crystals with tabulated values of diffraction data collection and refinement statistics are fully explained in Christensen et al. (2017).[19] In brief, the sitting drop vapor diffusion technique was used for the crystallization of HsPYCR1, and then diffraction-quality crystals in the space groups $P2_12_12$ and C2 were grown.[19] Ligand-free $P2_12_12$ protein crystals were more amenable for ligand soaking to prepare binary complexes of HsPYCR1 with NADPH bound, HsPYCR1 with L-proline bound, and ternary complex of HsPYCR1 with NADPH and the L-P5C/L-proline analog of L-THFA bound, whereas the C2 protein crystal form was examined as the ligand-free enzyme.[19] X-ray diffraction data were collected on Advanced Light Source beamline 4.2.2 at Lawrence Berkeley National Laboratory using a Taurus-1 detector in shutterless mode, and the initial phases of crystal diffractions were calculated with molecular replacement using PHASER.[19,20]

Analytical ultracentrifugation

Sedimentation-velocity experiments were conducted with a Beckman XL-I analytical ultracentrifuge using an An50Ti rotor and a two-sector cell. Sample sedimentation was continuously monitored at 20 °C using Rayleigh interference optics at 35,000 rpm for a total of 300 scans spaced at 2-min intervals. To observe the concentration dependence of oligomerization, sedimentation-velocity experiments were performed at two different protein concentrations (0.8 and 6.0 mg/ml) as determined by the Pierce BCA protein assay.

Sedimentation-velocity data were processed using Sedfit,[21] assuming a partial specific volume of 0.73 ml/g. Analysis of the data in Sedfit allowed for the determination of apparent sedimentation coefficient (*c(S)*) and molecular mass (*c(M)*) distributions. The approximate frictional ratio for decameric HsPYCR1 was determined by allowing the value to vary in the *c(S)* calculation of the 6.0 mg/ml protein sample. The frictional ratio was refined to a value of 1.94. This value was applied to the analysis of the 0.8 mg/ml protein sample for consistency in decamer peak identification. Analyzed data were normalized and plotted using Origin 2016.

Kinetic measurements

All HsPYCR1 kinetic data were collected in triplicate using a Varian Cary BIO 50 UV-visible spectrophotometer (Agilent Technologies) following procedures adapted from previous studies.[4,14,22,13,23] PYCR enzyme activity assays were performed by measuring the L-P5C-dependent oxidation of NADPH (Sigma-Aldrich) or of NADH (Sigma-Aldrich) at 340 nm and at 380 nm, using millimolar extinction coefficients 6.22 mM^{-1} cm^{-1} and 1.314 mM^{-1} cm^{-1}, respectively.[4,24] DL-P5C was synthesized according to the protocol by Williams and Frank,[25] which involved the metaperiodation of DL-5-hydroxylysine hydrochloride at 4 °C with the reaction product purified by Dowex 50WX4 cation exchange column chromatography using 1 M HCl to elute the fractions of DL-P5C. Additional details concerning the synthesis and mass spectrometry characterization of DL-P5C are provided in Appendix Chapter 1. DL-P5C was neutralized to pH 7.5 with 1 M Tris-HCl (pH 9.0) buffer immediately before assays. NADH and NADPH stock concentrations were spectrophotometrically determined at 340 nm. Assays

(600-µl total volume) were performed in 1.5 mL rectangular polystyrene cuvettes (1 cm pathlength) (USA Scientific) at 37 °C in 0.1 M Tris-HCl (pH 7.5) reaction buffer, 0.01% Brij-35 detergent (Santa Cruz Biotechnology), 1 mM EDTA disodium salt (Fisher), using 0.006 and 0.06 µM HsPYCR1 wild-type and mutant T238A enzymes. For assays in which DL-P5C was varied, the ionic strength was maintained at approximately 450-480 mM $Tris^+Cl^-$ at each DL-P5C concentration by adding a balance of 1 M Tris-HCl (pH 7.5) buffer.[26]

Enzyme activity was calculated from the linear portion of the initial absorbance decrease using the Beer-Lambert-Bouguer law.[27,28,29] Assays were performed in triplicate and data were expressed as mean ± standard deviation. Data were fit by nonlinear regression to the Henri-Michaelis-Menten equation using SigmaPlot 12.0 (version 12.0.0.182, Systat Software) to estimate the maximal reaction velocity limit (V_{lim}) and the apparent Michaelis-Menten constant (K_M^{app}) values (value ± standard error). The K_M^{app} for L-P5C was assumed to be half the K_M^{app} value for the racemic DL-P5C mixture. The apparent catalytic turnover rate (k_{cat}^{app}) and substrate specificity constant or catalytic efficiency values (k_{cat}^{app}/K_M^{app}) were calculated from V_{lim} and K_M^{app}. Product(s) inhibition kinetics were analyzed by global fitting of the data to different inhibition models using the Enzyme Kinetics Wizard Module in SigmaPlot 12.0 and by Hanes-Woolf plot analysis. For NAD^+ product inhibition, the data fit best to a mixed inhibition (Full) model with enzyme-inhibition constants K_{IC}^{app} and $K_{IU}^{app} = \alpha(K_{IC}^{app})$ ($\alpha = 0.4728$). The mixed inhibition model had the highest squared correlation coefficient (R^2)-ranking among eight tested inhibition models. For L-Pro product inhibition, the highest R^2-ranking model was competitive inhibition (Full) (K_{IC}^{app}).

RESULTS

Tertiary and quaternary structure of HsPYCR1

High-resolution crystal structures of HsPYCR1 revealed that the protomer consists of an N-terminal α/β domain and a C-terminal α domain (Fig. 2.1A).

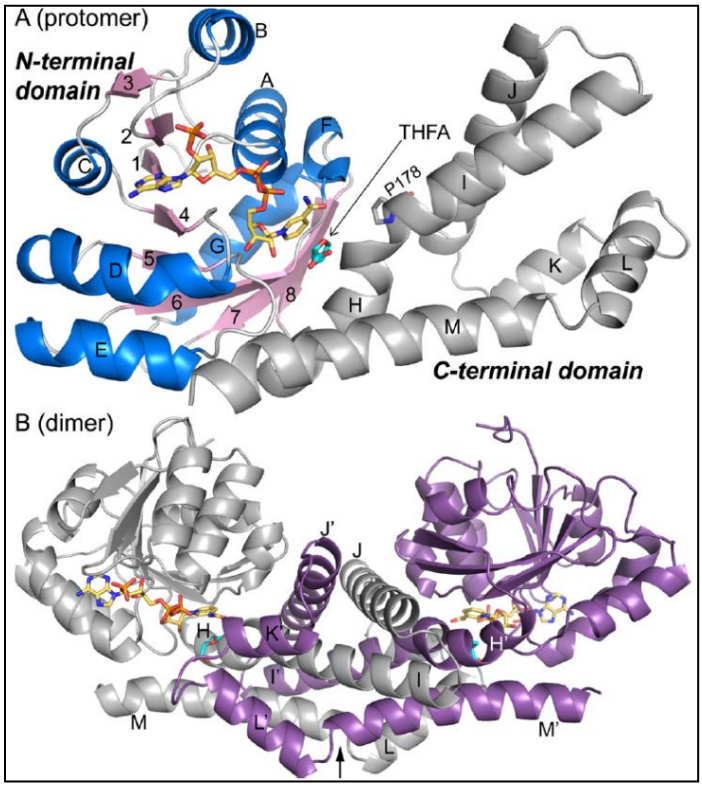

Figure 2.1. Structures of the PYCR1 protomer and dimer. A, structure of the protomer of the ternary complex with NADPH and with the L-proline/L-P5C analog of L-THFA. The N-terminal NAD(P)H-binding domain is colored according to secondary structure, with β-strands in pink and α-helices in blue. The C-terminal oligomerization domain is colored gray. NADPH appears in gold sticks. L-THFA is shown as cyan sticks. β-strands are labeled 1-8; α-helices are labeled A-M. Helix-disrupting Pro-178 is shown. B, structure of the dimer. The α-helices of the C-terminal domain are labeled H-M for the gray protomer and H'-M' for the purple protomer. NADPH and L-THFA are colored gold and cyan, respectively. The arrow represents the 2-fold axis of the dimer.

The N-terminal domain features the classic Rao-Rossmann dinucleotide-binding fold, which consists of a pair of βαβαβ motifs that interact across a pseudo-2-fold axis to form a six-stranded parallel β-sheet with strand order 321456.[30,31] An

additional βαβ substructure follows strand 6 such that the full β-sheet of the N-terminal domain has eight β-strands, with the last two β-strands antiparallel to the Rao-Rossmann β-strands. β-strand 8 of the N-terminal domain connects to the C-terminal domain, which consists of a bundle of six α-helices. The C-terminal domain plays a major role in oligomerization. For example, the C-terminal domain mediates dimerization (Fig. 2.1B). In the dimer, the C-terminal domains of two protomers form an interlocking bundle of α-helices. Overall, the domain architecture of HsPYCR1 is typical for P5CRs.[13]

The oligomeric state of HsPYCR1 in solution was determined with analytical ultracentrifugation using sedimentation-velocity. Initial studies performed at 0.8 mg/ml (24 μM) revealed a distribution of apparent sedimentation coefficient that exhibits a series of peaks in the range 1–7.5 S (Fig. 2.2A).

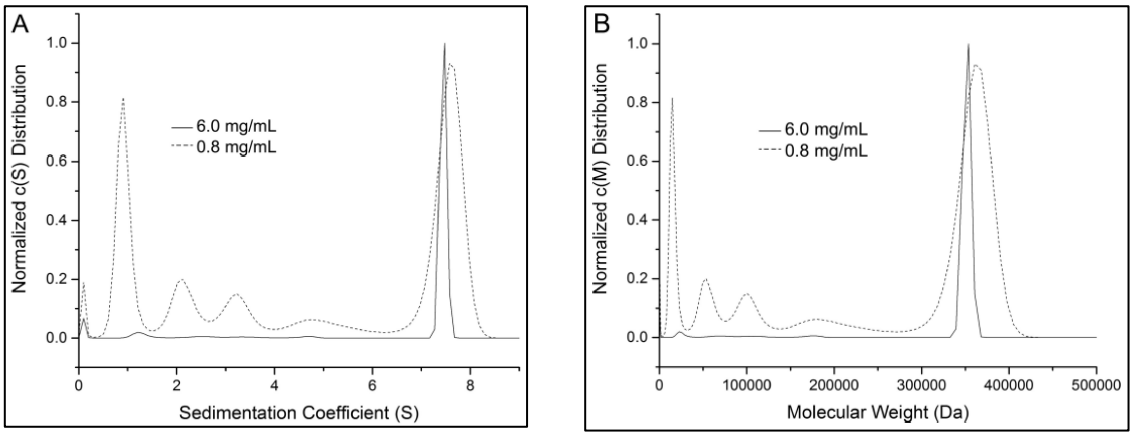

Figure 2.2. Oligomerization of PYCR1 in solution. A, apparent sedimentation coefficient distribution determined at 6.0 mg/ml (solid line) and 0.8 mg/ml (dashed line). B, molecular mass distribution determined at 6.0 mg/ml (solid line) and 0.8 mg/ml (dashed line).

The corresponding distribution of molecular masses reveals multiple species in solution spanning from ~30 to 350 kDa (Fig. 2.2B). Because the theoretical

molecular mass of a monomer is 34 kDa, the *c(M)* distribution is consistent with the presence of multiple oligomeric states ranging from monomer to decamer. To further investigate the possibility that decamer formation is concentration-dependent, sedimentation velocity was also performed at the higher concentration of 6.0 mg/ml (180 μM). This experiment yielded a sedimentation coefficient distribution with a single peak at 7.47 S (Fig. 2.2A), corresponding to a molecular mass of 350 kDa (Fig. 2.2B). Thus, at a concentration of 180 μM, HsPYCR1 is almost entirely decameric. These results are consistent with P5CR forming a self-association equilibrium in solution.

Analysis of crystal packing with PDBePISA[32] reveals a pentamer-of-dimers assembly in both crystal forms (Fig. 2.3), consistent with the decamer observed in sedimentation-velocity experiments.

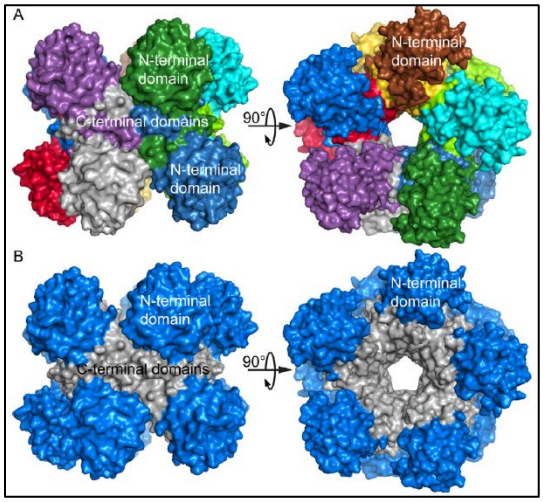

Figure 2.3. The PYCR1 pentamer-of-dimers decamer. A, two orthogonal views of the decamer, with each chain differently colored. B, two orthogonal views of the decamer, with the N-terminal domains colored blue and the C-terminal domains colored gray. Note that the C-terminal domains mediate all protein-protein interactions in the decamer.

This assembly is also present in other P5CR crystal structures from a variety of organisms.[13,14,15] The consistency of this assembly across space groups and

kingdoms suggests the decamer is a fundamental structural property of P5CRs.

The decamer is a pentamer-of-dimers assembly that resembles an "hourglass-shaped barrel"[13] when viewed perpendicular to the 5-fold axis (Fig. 2.3). The dimers are arranged such that the N-terminal domains form pentameric rings at the top and bottom of the barrel, and the C-terminal domains form a cylinder that connects the two rings. A notable feature of the decamer is that most of the interfacial surface area results from the interaction between C-terminal domains, whereas the N-terminal domains are relatively isolated from other protomers (Fig. 2.3B).

Identification of the NAD(P)H-binding site

Electron density maps revealed the location and conformation of NADPH bound to HsPYCR1 (Fig. 2.4).

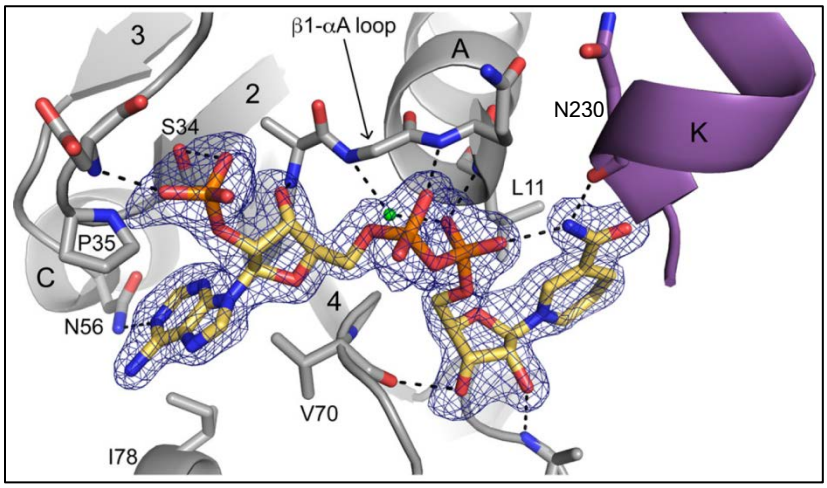

Figure 2.4. Electron density and interactions for NADPH bound to PYCR1. The cage represents a simulated annealing (F_o - F_c) map contoured at 3σ. Selected α-helices and β-strands are labeled in accordance with Fig. 2.1. α-helix K (purple) is from the opposite protomer of the dimer. The conserved water molecule of the Rao-Rossmann dinucleotide-binding fold is colored green.[33]

In the enzyme—NADPH binary complex structure, the density is very strong in two of the five chains in the asymmetric unit, allowing modeling of the complete

cofactor with occupancy of 1.0 (chains C and E). We note that high occupancy of NADPH appears to be correlated with the stabilization of residues 34–40, which form a loop that interacts with the adenosine portion of NADPH. Density for this loop is very strong in chains C and E but much weaker in chains A, B, and D. The loop was omitted in chain A.

NADPH binds at the C-termini of the strands of the Rao-Rossmann dinucleotide-binding fold (Fig. 2.4). The cofactor adopts an extended conformation with the pyrophosphate poised above the N-terminus of the first α-helix of the Rao-Rossmann fold (αA). The adenosine group interacts with the first βαβαβ motif, whereas the nicotinamide riboside contacts the second βαβαβ motif. In summary, NADPH adopts the canonical pose expected for nicotinamide adenine dinucleotides bound to Rao-Rossmann fold domains.[33]

NADPH forms several noncovalent interactions with the enzyme (Fig. 2.4). The ribose hydroxyls and pyrophosphate hydrogen bond exclusively with protein backbone atoms. Only two side chains participate in hydrogen bonding with NADPH. Asn56 hydrogen bonds with the adenine ring, whereas Ser34 interacts with the 2'-phosphoryl group. Nonpolar side chains help position the bases of NADPH, with Pro35, Val70, and Ile78 contacting the adenine and Leu11 packing against the nicotinamide.

The carboxamide of NADPH has a 2-fold rotational degeneracy at the resolution of our structures; however, hydrogen bonding can be used to deduce the correct orientation of this group. The carboxamide amino group has been modeled so it forms an intramolecular hydrogen bond with the pyrophosphate and another hydrogen bond with the backbone carbonyl of Asn230 (Fig. 2.4). In

contrast, rotation by 180° places the carboxamide carbonyl next to obligate hydrogen bond acceptors, resulting in no hydrogen bonds.

The L-proline-binding site

The structure of HsPYCR1 complexed with the product L-proline was determined at 1.90 Å resolution from a crystal that had been soaked in 1.8 M L-proline (Fig. 2.5). The electron density allowed modeling of L-proline in the active site of all five chains with occupancy of 1.0.

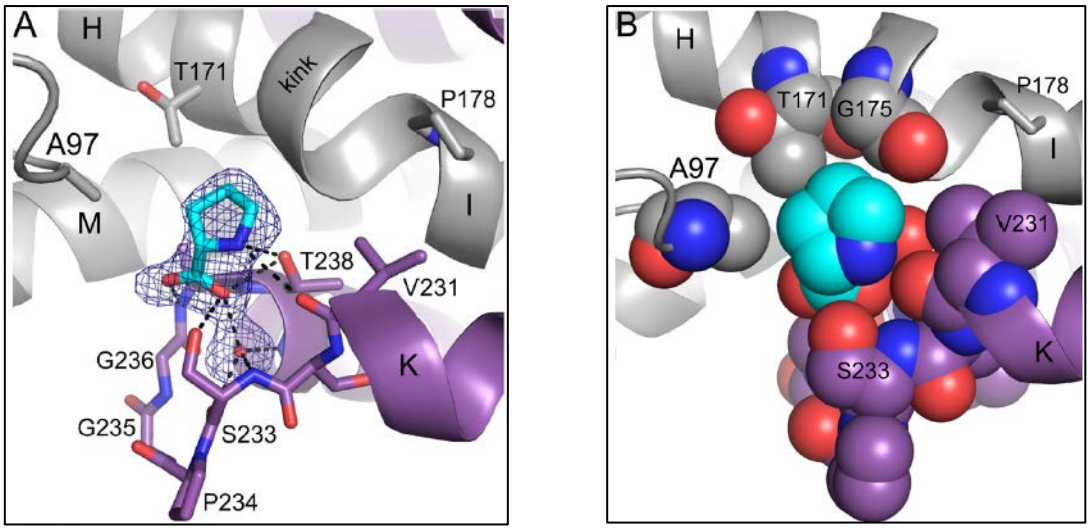

Figure 2.5. The L-proline-binding site. A, electron density and interactions for L-proline (cyan) bound to PYCR1. The cage represents a simulated annealing (F_o - F_c) map contoured at 3σ. The two protomers of the dimer are colored purple and gray. Note that L-proline binds in the dimer interface, and a hydrogen bonding water molecule in the vicinity of the carboxylate of L-proline and Ser233 is colored red. Selected α-helices are labeled in accordance with Fig. 2.1. B, space-filling representation of the L-proline-binding site highlighting nonpolar residues that contact the methylene groups of L-proline.

L-proline was also modeled into an election density feature on the surface of the protein near Thr137. The adventitious binding of L-proline to the protein surface is common when used in high concentration as a cryoprotectant, as is the case here.[34]

L-proline binds in a section of the dimer interface where the αK-αL loop of one

protomer meets α-helices H, I, and M of the other protomer (Figs. 2.1B and 2.5A). The carboxylate and imino groups of L-proline are anchored to the αK-αL loop via several hydrogen bonds, some of which are mediated by a water molecule (Fig. 2.5A). Of note is the hydrogen bond between Thr238 and the imine nitrogen of L-proline. It has been proposed that this conserved Thr residue functions in catalysis by donating a proton to the imine nitrogen atom of L-P5C.[13]

The roof of the binding site provides nonpolar contacts for the methylene groups of L-proline. These contacts include Ala97 of the Rao-Rossmann fold and the kink between α-helices H and I (Fig. 6B). The kink is caused by the presence of conserved Pro178 and appears to be a common feature of P5CRs because it is also present in structures of P5CR from microorganisms.[14] Within the kink, the carbonyls of residues 174 and 175 splay outward to avoid a steric clash with the Cδ of Pro178, and as a result, these groups do not form (*i* to *i* + 4) hydrogen bonds, and the helical structure is disrupted. Thr171 and Gly175 of the kink region provide nonpolar contacts with the methylene groups of L-proline. These interactions bury the carboxylate face of L-proline, leaving the other face solvent-exposed and available for catalysis (Fig. 2.5B).

The ternary complex with NADPH and L-THFA

The structure of HsPYCR1 complexed with NADPH and L-THFA was determined at 1.85 Å resolution (Fig. 2.6). The electron density is very strong for both ligands in all five chains, allowing the inclusion of the ligands in the model at an occupancy of 1.0. This is the first structure of any P5CR that mimics the enzyme—NADPH—L-P5C Michaelis complex.

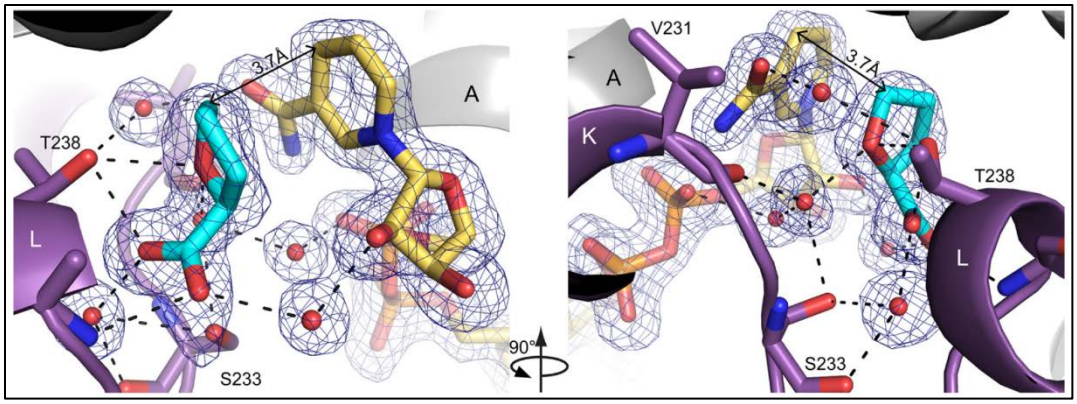

Figure 2.6. Structure of the ternary complex of PYCR1 with NADPH and L-THFA. The cage represents a simulated annealing (F_o - F_c) map contoured at 3σ. NADPH and L-THFA are colored gold and cyan, respectively. Water molecules are colored red. The two protomers of the dimer are colored purple and gray. Two orthogonal views are shown. Selected α-helices are labeled in accordance with Fig. 2.1A.

The structure shows that dimerization is essential for catalytic activity. NADPH interacts with the Rao-Rossmann fold of one protomer, and L-THFA binds in the αK-αL loop of the opposite protomer of the dimer (Fig. 2.1B). NADPH adopts the same conformation as in the binary enzyme-NADPH complex, whereas L-THFA occupies the aforementioned L-proline site. Water-mediated hydrogen bonding appears to play a role in stabilizing the ternary complex, because five water molecules with strong electron density connect L-THFA, NADPH, and the protein (Fig. 2.6). The ring of L-THFA stacks in parallel with the nicotinamide ring such that C5 of L-THFA, which represents the hydride acceptor atom of L-P5C, is 3.7 Å from C4 of the nicotinamide ring. The structure is consistent with a direct hydride-transfer mechanism.

Henri-Michaelis-Menten kinetics and product(s) inhibition Hanes-Woolf kinetics

Steady-state kinetics assays showed that HsPYCR1 utilizes both NADH and NADPH cofactors (Fig. 2.7, A-C). When keeping L-P5C fixed (3.5 mM) while

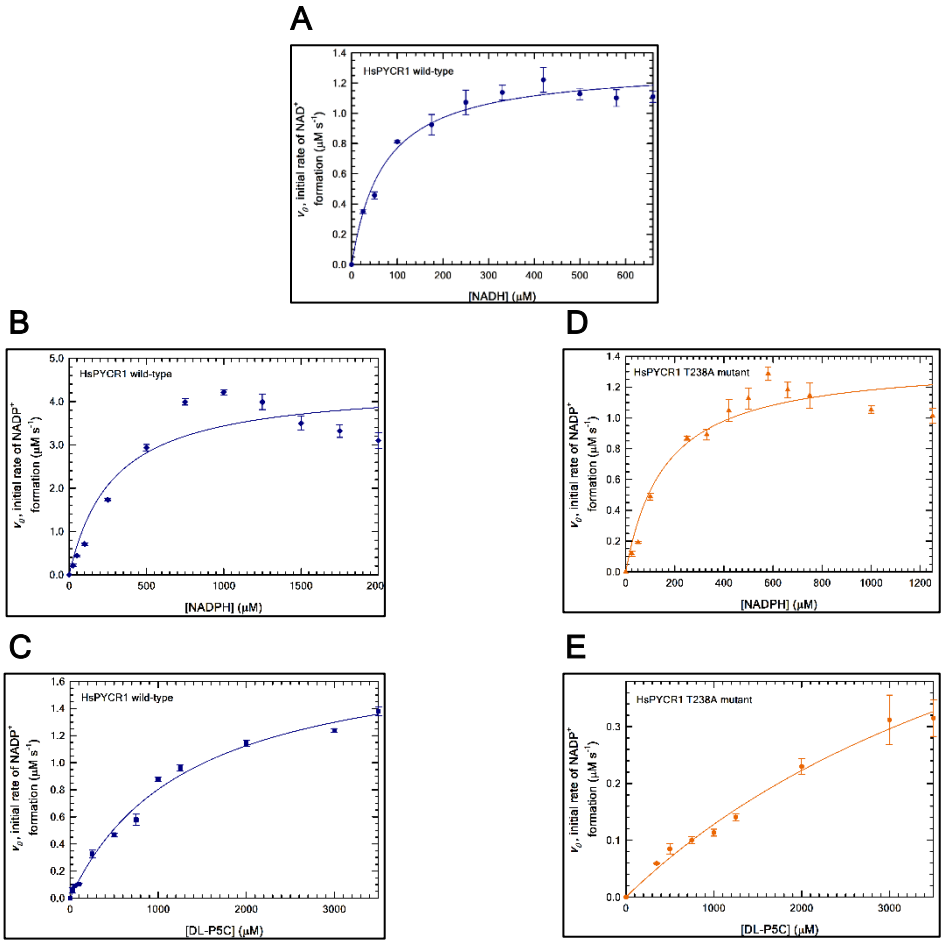

Figure 2.7. Initial velocity data for PYCR1 wild-type and T238A mutant. (A) varied NADH (0-660 μM) and fixed DL-P5C (3.5 mM) with 0.006 μM HsPYCR1. (B) varied NADPH (0-2000 μM) and fixed DL-P5C (3.5 mM) with 0.06 μM HsPYCR1. (C) varied DL-P5C (0-3.5 mM) and fixed NADPH (500 μM) with 0.06 μM HsPYCR1. (D) HsPYCR1 T238A mutant (0.06 μM) with varied NADPH (0-1200 μM) and fixed DL-P5C (3.5 mM). (E) HsPYCR1 T238A mutant (0.06 μM) with varied DL-P5C (0-3.5 mM) and fixed NADPH (500 μM). Assays were performed at 37 °C in 0.1 M Tris-HCl (pH 7.5) reaction buffer. Data (mean ± standard deviation) are plotted as variable substrate concentration (μM) versus initial reaction velocity of NAD(P)$^+$ product formation (μM s^{-1}) with non-linear least-squares fits to the Henri-Michaelis-Menten equation from which the kinetic parameters reported in Table 2.1 were derived. Apparent substrate inhibition is observed with wild-type HsPYCR1 and varied NADPH (panel B) but the data could not be fit satisfactorily to an equation for general substrate inhibition.

varying the dinucleotide concentration, K_M^{app} values of 70 and 283 μM for NADH and NADPH were obtained (Table 2.1). The k_{cat}^{app} value was nearly 3-fold higher

Table 2.1. Steady-state kinetic parameters for PYCR1[a]

Enzyme	Varied Substrate	Fixed Substrate	K_M^{app} (μM)	k_{cat}^{app} (s^{-1})	(k_{cat}^{app}/K_M^{app}) (M^{-1} s^{-1})
Wild-type[b]	NADH	DL-P5C[d]	70 ± 11	218 ± 8	(31 ± 5.) x 10^5
	NADPH	DL-P5C[d]	283 ± 119	74 ± 8	(2.6 ± 1.1) x 10^5
	DL-P5C	NADPH[e]	667 ± 88[f]	31 ± 2	(0.47 ± 0.07) x 10^5
T238A[c]	NADPH	DL-P5C[d]	159 ± 47	23 ± 2	(1.4 ± 0.4) x 10^5
	DL-P5C	NADPH[e]	2887 ± 774[f]	14 ± 3	(0.05 ± 0.02) x 10^5

[a]Value ± std error are the apparent best-fit parameters from non-linear least-squares fit of the data to the Henri-Michaelis-Menten equation using SigmaPlot 12.0 (version 12.0.0.182, Systat Software). Data plotted as the (mean ± SD) of n=3 technical replicates.
[b]Final enzyme concentration of 0.006 μM (for varied NADH with fixed DL-P5C) and 0.06 μM in remaining assays.
[c]Final enzyme concentration of 0.06 μM in the assay.
[d]DL-P5C concentration fixed at 3500 μM.
[e]NAD(P)H concentration fixed at 500 μM.
[f]Reported value is the concentration of L-P5C, which is assumed to be half the concentration of the DL-P5C racemic mixture.

higher with NADH, resulting in a 12-fold greater catalytic efficiency (k_{cat}^{app}/K_M^{app}) relative to NADPH (Table 2.1). A previous study reported a 6.5-fold higher catalytic efficiency of HsPYCR1 with NADH over NADPH.[4] Kinetic values of k_{cat}^{app} as 31 s^{-1} and K_M^{app} as 667 μM L-P5C were determined for wild-type HsPYCR1 from assays varying L-P5C while keeping NADPH fixed (Table 2.1, Fig. 2.7C).

The importance of Thr238 was tested with the site-directed mutation T238A. It has been proposed that this universally conserved residue functions in catalysis by donating a proton to the imine nitrogen of L-P5C.[13] This proposition was based on the observation of a hydrogen bond between the hydroxyl group of the conserved Thr and the imine nitrogen of the product L-proline in P5CR structures

from microorganisms[14], an interaction that is also seen in HsPYCR1 (Fig. 2.5A). The analogous hydrogen bond to L-THFA is also present in the ternary complex (Fig. 2.6).

Kinetic parameters for the T238A mutant enzyme were determined by varying NADPH and L-P5C (Fig. 2.7, D and E). Values of k_{cat}^{app} as 23 s^{-1} and 14 s^{-1} with K_M^{app} as 159 μM and 2887 μM for NADPH and L-P5C, respectively, were determined (Table 2.1). Because the K_M^{app} is near the upper concentration of L-P5C available, a k_{cat}^{app}/K_M^{app} value of 16,700 M^{-1} s^{-1} was also estimated from the slope of the linear region ([S] << K_M^{app}) of the Henri-Michaelis-Menten plot. The nearly 10-fold lower k_{cat}^{app}/K_M^{app} value of the T238A mutant relative to wild-type HsPYCR1 with L-P5C is consistent with the proposed role of Thr238 hydrogen bonding to the substrate.

The binding order of L-P5C and NADPH to HsPYCR1 was evaluated by product(s) inhibition studies.[35] The inhibition of HsPYCR1 by $NADP^+$ was first examined by varying NADPH and holding DL-P5C constant. Table 2.2 shows that increases in $NADP^+$ concentration (0-15 mM) results in a decreasing trend in k_{cat}^{app} and a slightly lower apparent K_M. With increasing $NADP^+$ concentration, trends of both increasing values of ($1/K_M^{app}$) and ($1/V_{lim}$) support the model of mixed inhibition by $NADP^+$ (Table 2.2 and Figure 2.8, A and B).[35] Global fitting of the data to a mixed inhibition model provided estimates of apparent competitive (K_{IC}) and uncompetitive (K_{IU}) inhibition constants for $NADP^+$ (Table 2.2). L-proline inhibition of HsPYCR1 was evaluated by varying DL-P5C (0-5500 μM) and holding NADPH fixed. Table 2.3 shows that with increasing L-proline concentration

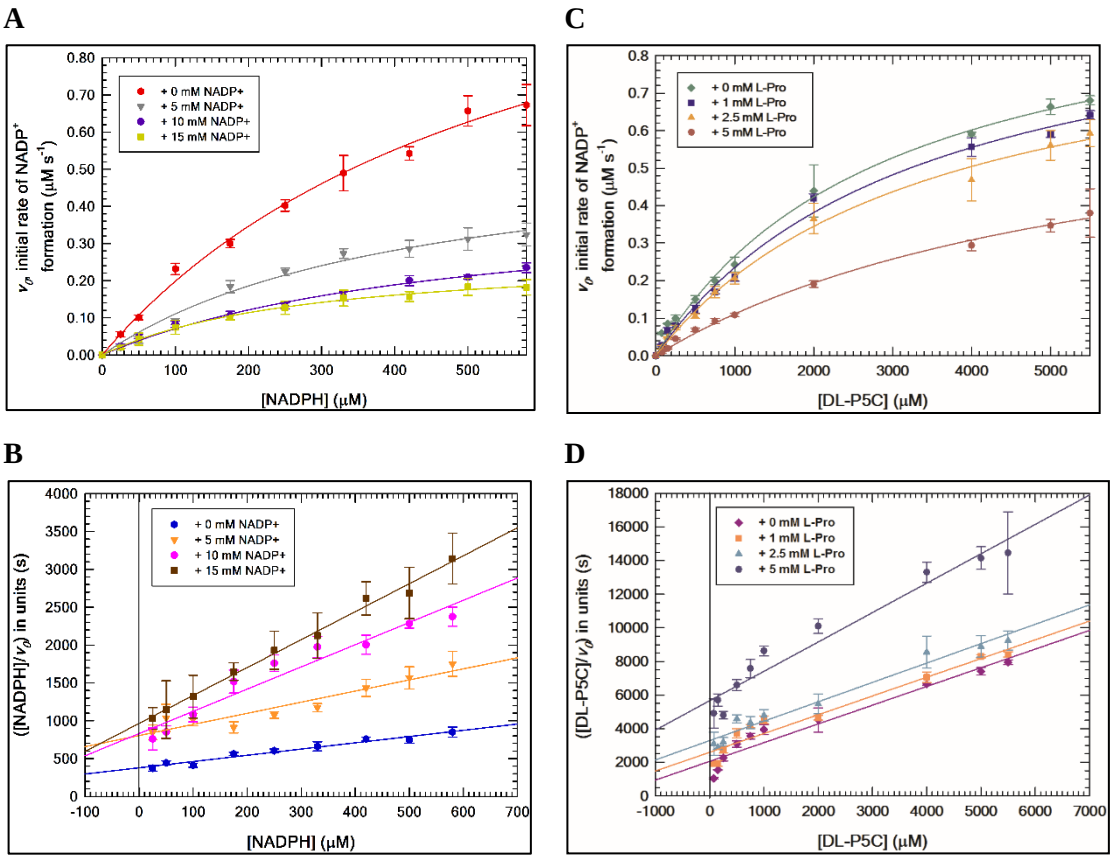

Figure 2.8. Product(s) inhibition kinetics of wild-type HsPYCR1. Henri-Michaelis-Menten plots of assays performed at (A) different $NADP^+$ concentrations (0-15 mM) while varying NADPH and holding DL-P5C constant (5000 μM) and (C) at different L-proline concentrations (0-5 mM) while varying DL-P5C and holding NADPH constant (500 μM). Hanes-Woolf plots of the data in panels B and D for inhibition of HsPYCR1 by (A) $NADP^+$ and (C) L-proline, respectively. Data plotted as (mean ± SD) of n=3 technical replicates with non-linear least-squares fits to the Henri-Michaelis-Menten equation and linear regression fits to the Hanes-Woolf equation using SigmaPlot 12.0.

Table 2.2. Steady-state kinetic parameters for $NADP^+$ product inhibition of HsPYCR1[a,b,c]

$NADP^+$ (mM)	K_M^{app} (μM)	k_{cat}^{app} (s^{-1})	(k_{cat}^{app}/K_M^{app}) (M^{-1} s^{-1})	K_{IC}^{app} (mM)	K_{IU}^{app} (mM)
0	587 ± 92	22.7 ± 0.2	(38.7 ± 6.1) x 10^3		
5	426 ± 91	9.7 ± 1.1	(22.7 ± 5.5) x 10^3	8.28 ± 1.36[d]	3.92 ± 0.64[d]
10	501 ± 98	7.1 ± 0.8	(14.1 ± 3.2) x 10^3		
15	284 ± 30	4.6 ± 0.2	(16.1 ± 1.9) x 10^3		

[a]Value ± Std error are reported for the apparent best-fit parameters of non-linear least-squares fit to the Henri-Michaelis-Menten equation using SigmaPlot 12.0 (version 12.0.0.182, Systat Software) with data plotted as (mean ± SD) of n=3 technical replicates.
[b]Final enzyme concentration of 0.06 μM was used for the assays.
[c]DL-P5C concentration was fixed at 5000 μM while NADPH concentration was varied 0-580 μM.
[d]Apparent inhibition constants, K_{IC}^{app} (competitive inhibition) and K_{IU}^{app} (=α(K_{IC}^{app})) (uncompetitive inhibition) were estimated by fitting data (25-580 μM NADPH) to the Mixed Inhibition (full) model with α=0.4728 using the Enzyme Kinetics Wizard Add-In on SigmaPlot 12.0 (version 12.0.0.182, Systat Software).

Table 2.3. Steady-state kinetic parameters for L-proline product inhibition of HsPYCR1[a,b,c]

L-proline (mM)	K_M^{app} (μM)[d]	k_{cat}^{app} (s^{-1})	(k_{cat}^{app}/K_M^{app}) (M^{-1} s^{-1})	K_{IC}^{app} (mM)
0	1463 ± 176	17.4 ± 1.0	(11.9 ± 1.6) x 10^3	2.61 ± 0.25[e]
1	1664 ± 219	17.0 ± 1.1	(10.2 ± 1.5) x 10^3	
2.5	1725 ± 210	15.7 ± 0.9	(9.1 ± 1.2) x 10^3	
5	2898 ± 396	12.6 ± 1.0	(4.3 ± 0.7) x 10^3	

[a]Value ± Std error are reported for the apparent best-fit parameters of non-linear least-squares fit to the Henri-Michaelis-Menten equation using SigmaPlot 12.0 (version 12.0.0.182, Systat Software) with data plotted as (mean ± SD) of n=3 technical replicates.
[b]Final enzyme concentration of 0.06 μM was used for the assays.
[c]NADPH concentration was fixed at 500 μM while DL-P5C concentration was varied 0-5500 μM.
[d]Reported value is the concentration of L-P5C, which is assumed to be half the concentration of the DL-P5C racemic mixture.
[e]Apparent competitive inhibition constant, K_{IC}^{app}, was estimated by fitting data (250-5500 μM DL-P5C) to a competitive inhibition (full) model using the Enzyme Kinetics Wizard Add-In on SigmaPlot 12.0 (version 12.0.0.182, Systat Software).

(0-5 mM), the value of K_M^{app} increased whereas V_{lim} remained fairly unchanged consistent with competitive inhibition by L-proline.[35] Best fits of the data to a competitive inhibition model yielded an apparent K_{IC} value of 145 μM L-proline (Table 2.3). Hanes-Woolf plots of the $NADP^+$ and L-proline inhibition data also

show linear regressions consistent with mixed and competitive inhibition, respectively (Figure 2.8, B and D). In these plots, linear trends converging at a common negative horizontal axis intercept with an increasing slope ($1/V_{lim}$) effect (Figure 2.8B) indicates $NADP^+$ is a mixed noncompetitive inhibitor[35] of HsPYCR1 with respect to NADPH. Parallel linear trends with an increasing vertical axis intercept (K_M^{app}/V_{lim}) effect (Figure 2.8D) indicate L-proline is a competitive inhibitor[35] with respect to L-P5C. Taken together, these modes of inhibition by each product ligand support a sequential-ordered binding mechanism of L-P5C binding first to the enzyme followed by NADPH.

DISCUSSION

In this work, we describe the first high-resolution structures of a human PYCR isozyme. Notably, the complex of HsPYCR1 with NADPH and the L-P5C/L-Pro analog of L-THFA is the first structure of a relevant ternary complex for any P5CR. This structure provides new information about the mechanism of the enzyme. Considering it to represent the E—NADPH—L-P5C Michaelis complex, the structure implies that L-P5C binds with its ring approximately parallel to the nicotinamide ring with C2 of L-P5C close to C4 of NADPH, as expected for a hydride-transfer mechanism. The donor-acceptor distance inferred from the structure is 3.7 Å, whereas the expected distance in the transition state for hydride-transfer reactions is ~2.7 Å.[36] It is possible that fluctuations of the enzyme are needed to achieve the transition state from the configuration represented in the crystal structure. Alternatively, our structure represents the product complex (E—$NADP^+$—L-Pro) rather than the substrate complex.

The structure also immediately suggests the stereochemistry of hydride

transfer. Because the B-side of the nicotinamide of NADPH contacts the implied substrate, HsPYCR1 is predicted to catalyze the transfer of the pro-4S hydrogen to L-P5C. This assignment agrees with a previous prediction based on superimposing separate structures of P5CR—$NADP^+$ and P5CR—L-Pro complexes.[13] To date, we are not aware of any reports of the determination of the stereochemistry of P5CR by kinetic isotope effect measurements.

It has been suggested that a conserved Thr or Ser in the active site functions as a general acid that donates a proton to the imine nitrogen of L-P5C.[13] Ser and Thr are not usually considered to be general acid/base catalysts due to their high pK_a values. It is possible for the protein micro-environment to lower the pK_a of an active site residue so it can function as a general acid, as occurs for Lys199 of the NAD-malic enzyme[37] and Arg69 of Sin resolvase.[38] However, the active site of HsPYCR1 does not have a preponderance of positively charged residues that could depress the pK_a of the proposed Thr residue. We mutated Thr238, which forms a hydrogen bond to the imine nitrogen of L-proline in our structure (Fig. 2.5A). The mutation to Ala did not substantially diminish the k_{cat}^{app}, suggesting that Thr238 is not essential for catalysis, whereas the k_{cat}^{app}/K_M^{app} of T238A mutant enzyme with varied L-P5C was 10-fold lower relative to wild type, indicating that the loss of Thr238 impacts L-P5C binding. The observed T238A mutant's k_{cat}^{app} as 14 s^{-1} may be due to a small acid or proton donor such as a water molecule that could enter and occupy the space devoid of steric bulk from the side chain of Thr at residue 238, thus allowing a proton abstraction by the imine nitrogen of L-P5C that affords some catalytic activity to occur. To rule out this possibility and to determine if the polarity present in the side chain hydroxyl

group of Thr is critical for catalytic activity, a prudent course of action would be an isosteric mutation that removes the polar side chain group as in a Thr238Val mutation. For reference, we note that mutation of Lys199 to Ala in the NAD-malic enzyme decreases V_{lim} by 10^5-fold magnitude.[37] Thus, it is concluded that Thr238 does not function as the general acid in HsPYCR1 but appears to have important interactions with the imine nitrogen of L-P5C, as corroborated by the structural and kinetic data.

Product(s) inhibition kinetics studies revealed L-Pro behaving as a competitive inhibitor and $NADP^+$ behaving as a mixed inhibitor against wild-type HsPYCR1 enzyme, which is diagnostic of a sequential binding order with L-P5C binding first to the enzyme followed by NADPH. This binding order is atypical of the general family of dehydrogenase enzymes, i.e. lactate dehydrogenase, which first binds NAD^+/NADH before the second substrate.[39] The proposed binding order is supported by the X-ray crystal structure of HsPYCR1 in complex with L-THFA and NADPH (Fig. 2.6), which shows that L-THFA, an analog of both L-proline and L-P5C, is buried within the active site. The binding site for L-THFA would be obstructed if NADPH were to bind first, thus supporting the sequential binding order of the smaller L-P5C molecule followed by binding of the larger NAD(P)H molecule. These findings are consistent with previous studies in which bacterial (*S. pyogenes*) and plant (*A. thaliana*) P5CRs were also proposed to follow a sequential-ordered binding mechanism with L-P5C binding prior to NAD(P)H.[13,40] Having the sequential-ordered binding mechanism of HsPYCR1 established will help guide development of new inhibitors and/or substrate analogs as molecular probes for modulating HsPYCR1 activity.

The noncanonical dinucleotide-binding site of HsPYCR1 proposed by Meng et al. (2006)[16] is not supported by the experimental data. The original NAD(P)H cofactor ligand density was poor, the difference density was uniformly and strongly negative, and the PDB_REDO pipeline essentially removed the contribution of the cofactor and Glu ligands by elevating their temperature factors to non-physical values. The NAD(P)H cofactor also had poor geometry and formed several bad contacts, all of which are inconsistent with a well-defined ligand-binding site.

This is in sharp contrast to the highly conserved nature of dinucleotide-binding sites in other Rao-Rossmann fold proteins. First reported in the 1970s, the Rao-Rossmann fold consists of repeated βα motifs and comprises six (typically) parallel β-strands with α-helices packed on either side of the β-sheet.[30,41,42] The dinucleotide binds with an extended conformation in the cleft found at the C-termini of the strands, with the pyrophosphate interacting with the N-terminus of αA and the Gly-rich β1-αA loop. Each base interacts with the opposing faces of the β-sheet, forming a network of polar and non-polar interactions. A previous analysis of 102 Rao-Rossmann fold protein structures representing 43 enzymes and 40 species demonstrated a remarkably high consistency of the binding site structure and cofactor conformation.[33] In fact, the binding site is so consistent that a conserved water molecule bridging the Gly-rich β1-αA loop and the pyrophosphate could effectively be considered part of the dinucleotide-binding motif.[33] Indeed, this water molecule is present in our structures (Fig. 2.4). In this context, it is surprising that a completely novel dinucleotide-binding mode for HsPYCR1 was proposed with almost no discussion of the important way in which

the site deviated from conventional wisdom.

Strong evidence from other structural studies also points to the mistaken nature of the unconventional binding site[16] of Meng et al. (2006). The core structural elements of HsPYCR1 are superimposable with those of available bacterial P5CR structures, and the dinucleotide ligands in the bacterial enzyme structures conform to the classic paradigm for Rao-Rossmann fold proteins.[13] Furthermore, the PDB contains an unpublished human PYCR1 structure (PDB code 2IZZ) that contains NAD^+ bound in the same location as our structure and bacterial P5CR structures. All of the above structural work also supports the conclusion that the binding site described by Meng et al. (2006)[16] is incorrect.

Incorrect ligand-binding site notwithstanding, there are positive aspects to the work of Meng et al. (2006). They were the first to establish that the fold of HsPYCR1 is consistent with homologous enzymes. Also, they documented the oligomeric state as a pentamer of intertwined dimers. These contributions to the literature remain valid. Nevertheless, the record must be corrected regarding the erroneous NAD(P)H-binding-site, and we recommend that correction take place. We also recommend that the recent in silico analysis of cutis laxa HsPYCR1 mutants, which is based on the incorrect active site, be reevaluated with the correct HsPYCR1 structure.[43]

Our results might explain why the canonical dinucleotide-binding site was unoccupied in the Meng et al. (2006) structures. To obtain complexes, Meng et al. (2006) soaked crystals in 0.3 mM NADH or NADPH.[16] Our measurements with HsPYCR1 indicate a $K_M{}^{app}$ of 0.07 mM for NADH and 0.3 mM for NADPH (Table 2.1). Thus, the dinucleotide concentrations used by Meng et al. (2006)[16] may not

have been high enough for saturation.

Many examples of incorrectly built structures or misplaced ligands have appeared in the crystallographic literature over the past few years.[44,45,46,47] Some have arisen from updates in genomic databases that revealed older structures solved with incorrect sequences.[44,48,49] Others are due to the very large number of new structures appearing each year coupled with the fact that many of them come from laboratories with little crystallographic experience.[50] Further, there is pressure now to produce faster, more numerous, and more novel results in science,[51] and ligand-binding density would be an important source of novelty. Finally, reviewers are often judging structures without access to coordinate files and electron density maps, making detailed verification of ligands difficult. Taken together, this leads to a risk of inappropriate ligand placement.

It has been suggested that the risk of errors in ligand placement could be mitigated by utilizing currently available structural tools.[52,53] These tools emphasize the inspection of electron density, stereochemistry, and ligand environment.[45,52] We suggest that the historical context of the ligand site also be considered. In the case of a family like Rao-Rossmann dinucleotide-binding proteins, which contain a highly conserved fold, strong proof should be required of the authors before proposing a completely new binding site.

REFERENCES

[1] Phang, J. M. (1985) The regulatory functions of proline and pyrroline-5-carboxylic acid, *Curr Top Cell Regul 25*, 91-132.

[2] Adams, E., and Frank, L. (1980) Metabolism of proline and the hydroxyprolines, *Annu Rev Biochem 49*, 1005-1061.

[3] Tanner, J. J. (2008) Structural biology of proline catabolism, *Amino Acids 35*, 719-730.

[4] De Ingeniis, J., Ratnikov, B., Richardson, A. D., Scott, D. A., Aza-Blanc, P., De, S. K., Kazanov, M., Pellecchia, M., Ronai, Z. e., Osterman, A. L., and Smith, J. W. (2012) Functional Specialization in Proline Biosynthesis of Melanoma, *PLoS ONE 7*, e45190 EP -.

[5] Reversade, B., Escande-Beillard, N., Dimopoulou, A., Fischer, B., Chng, S. C., Li, Y., Shboul, M., Tham, P. Y., Kayserili, H., Al-Gazali, L., Shahwan, M., Brancati, F., Lee, H., O'Connor, B. D., Schmidt-von Kegler, M., Merriman, B., Nelson, S. F., Masri, A., Alkazaleh, F., Guerra, D., Ferrari, P., Nanda, A., Rajab, A., Markie, D., Gray, M., Nelson, J., Grix, A., Sommer, A., Savarirayan, R., Janecke, A. R., Steichen, E., Sillence, D., Hausser, I., Budde, B., Nürnberg, G., Nürnberg, P., Seemann, P., Kunkel, D., Zambruno, G., Dallapiccola, B., Schuelke, M., Robertson, S., Hamamy, H., Wollnik, B., Van Maldergem, L., Mundlos, S., and Kornak, U. (2009) Mutations in PYCR1 cause cutis laxa with progeroid features, *Nat Genet 41*, 1016-1021.

[6] Phang, J. M., Liu, W., and Zabirnyk, O. (2010) Proline metabolism and microenvironmental stress, *Annu Rev Nutr 30*, 441-463.

[7] Nilsson, R., Jain, M., Madhusudhan, N., Sheppard, N. G., Strittmatter, L., Kampf, C., Huang, J., Asplund, A., and Mootha, V. K. (2014) Metabolic enzyme expression highlights a key role for MTHFD2 and the mitochondrial folate pathway in cancer, *Nat Commun 5*, 3128.

[8] Ou, R., Zhang, X., Cai, J., Shao, X., Lv, M., Qiu, W., Xuan, X., Liu, J., Li, Z., and Xu, Y. (2016) Downregulation of pyrroline-5-carboxylate reductase-2 induces the autophagy of melanoma cells via AMPK/mTOR pathway, *Tumour Biol 37*, 6485-6491.

[9] Loayza-Puch, F., Rooijers, K., Buil, L. C., Zijlstra, J., Oude Vrielink, J. F., Lopes, R., Ugalde, A. P., van Breugel, P., Hofland, I., Wesseling, J., van Tellingen, O., Bex, A., and Agami, R. (2016) Tumour-specific proline vulnerability uncovered by differential ribosome codon reading, *Nature 530*, 490-494.

[10] Phang, J. M., Liu, W., Hancock, C., and Christian, K. J. (2012) The proline regulatory axis and cancer, *Front Oncol 2*, 60.

[11] Zeng, T., Zhu, L., Liao, M., Zhuo, W., Yang, S., Wu, W., and Wang, D. (2017) Knockdown of PYCR1 inhibits cell proliferation and colony formation via cell cycle arrest and apoptosis in prostate cancer, *Med Oncol 34*, 27.

[12] Nakayama, T., Al-Maawali, A., El-Quessny, M., Rajab, A., Khalil, S., Stoler, Joan M., Tan, W.-H., Nasir, R., Schmitz-Abe, K., Hill, R. S., Partlow,

Jennifer N., Al-Saffar, M., Servattalab, S., LaCoursiere, Christopher M., Tambunan, Dimira E., Coulter, Michael E., Elhosary, Princess C., Gorski, G., Barkovich, A. J., Markianos, K., Poduri, A., and Mochida, Ganeshwaran H. (2015) Mutations in PYCR2, Encoding Pyrroline-5-Carboxylate Reductase 2, Cause Microcephaly and Hypomyelination, *The American Journal of Human Genetics 96*, 709-719.

[13] Nocek, B., Chang, C., Li, H., Lezondra, L., Holzle, D., Collart, F., and Joachimiak, A. (2005) Crystal structures of delta1-pyrroline-5-carboxylate reductase from human pathogens Neisseria meningitides and Streptococcus pyogenes, *J Mol Biol 354*, 91-106.

[14] Ruszkowski, M., Nocek, B., Forlani, G., and Dauter, Z. (2015) The structure of Medicago truncatula δ(1)-pyrroline-5-carboxylate reductase provides new insights into regulation of proline biosynthesis in plants, *Front Plant Sci 6*, 869.

[15] Franklin, M. C., Cheung, J., Rudolph, M. J., Burshteyn, F., Cassidy, M., Gary, E., Hillerich, B., Yao, Z. K., Carlier, P. R., Totrov, M., and Love, J. D. (2015) Structural genomics for drug design against the pathogen Coxiella burnetii, *Proteins 83*, 2124-2136.

[16] Meng, Z., Lou, Z., Liu, Z., Li, M., Zhao, X., Bartlam, M., and Rao, Z. (2006) Crystal Structure of Human Pyrroline-5-carboxylate Reductase, *Journal of Molecular Biology 359*, 1364-1377.

[17] Rao, S. T., and Rossmann, M. G. (1973) Comparison of super-secondary structures in proteins, *J Mol Biol 76*, 241-256.

[18] Kleiger, G., and Eisenberg, D. (2002) GXXXG and GXXXA motifs stabilize FAD and NAD(P)-binding Rossmann folds through C(alpha)-H... O hydrogen bonds and van der waals interactions, *J Mol Biol 323*, 69-76.

[19] Christensen, E. M., Patel, S. M., Korasick, D. A., Campbell, A. C., Krause, K. L., Becker, D. F., and Tanner, J. J. (2017) Resolving the cofactor-binding site in the proline biosynthetic enzyme human pyrroline-5-carboxylate reductase 1, *Journal of Biological Chemistry 292*, 7233-7243.

[20] McCoy, A. J., Grosse-Kunstleve, R. W., Adams, P. D., Winn, M. D., Storoni, L. C., and Read, R. J. (2007) Phaser crystallographic software, *J Appl Crystallogr 40*, 658-674.

[21] Schuck, P. (2000) Size-distribution analysis of macromolecules by sedimentation velocity ultracentrifugation and lamm equation modeling, *Biophys J 78*, 1606-1619.

[22] Merrill, M. J., Yeh, G. C., and Phang, J. M. (1989) Purified human erythrocyte pyrroline-5-carboxylate reductase. Preferential oxidation of NADPH, *Journal of Biological Chemistry 264*, 9352-9358.

[23] Szoke, A., Miao, G. H., Hong, Z., and Verma, D. P. (1992) Subcellular location of delta-pyrroline-5-carboxylate reductase in root/nodule and leaf of soybean, *Plant Physiol 99*, 1642-1649.

[24] Deutch, C. E., Klarstrom, J. L., Link, C. L., and Ricciardi, D. L. (2001) Oxidation of l-Thiazolidine-4-Carboxylate by Δ1-Pyrroline-5-Carboxylate Reductase in Escherichia coli, *Current Microbiology 42*, 442-446 LA - English.

[25] Williams, I., and Frank, L. (1975) Improved chemical synthesis and enzymatic assay of delta-1-pyrroline-5-carboxylic acid, *Anal Biochem 64*, 85-97.

[26] Moxley, M. A., Sanyal, N., Krishnan, N., Tanner, J. J., and Becker, D. F. (2014) Evidence for hysteretic substrate channeling in the proline dehydrogenase and Δ1-pyrroline-5-carboxylate dehydrogenase coupled reaction of proline utilization A (PutA), *J Biol Chem 289*, 3639-3651.

[27] Beer. (1852) Bestimmung der Absorption des rothen Lichts in farbigen Flüssigkeiten, *Annalen der Physik 162*, 78-88.

[28] Lambert, J. H., and Klett, E. (1760) *Photometria sive de mensura et gradibus luminis, colorum et umbrae*, Klett.

[29] Bouguer, P. (1729) *Essai d'optique sur la gradation de la lumière*, chez Claude Jombert, ruë S. Jacques, au coin de la ruë des Mathurins, à l ….

[30] Adams, M. J., Ford, G. C., Koekoek, R., Lentz, P. J., McPherson, A., Rossmann, M. G., Smiley, I. E., Schevitz, R. W., and Wonacott, A. J. (1970) Structure of lactate dehydrogenase at 2-8 A resolution, *Nature 227*, 1098-1103.

[31] Rossmann, M. G., Moras, D., and Olsen, K. W. (1974) Chemical and biological evolution of nucleotide-binding protein, *Nature 250*, 194-199.

[32] Krissinel, E., and Henrick, K. (2007) Inference of macromolecular assemblies from crystalline state, *J Mol Biol 372*, 774-797.

[33] Bottoms, C. A., Smith, P. E., and Tanner, J. J. (2002) A structurally conserved water molecule in Rossmann dinucleotide-binding domains, *Protein Sci 11*, 2125-2137.

[34] Pemberton, T. A., Still, B. R., Christensen, E. M., Singh, H., Srivastava, D., and Tanner, J. J. (2012) Proline: Mother Nature's cryoprotectant applied to protein crystallography, *Acta Crystallogr D Biol Crystallogr 68*, 1010-1018.

[35] Cornish-Bowden, A. (2012) *Fundamentals of enzyme kinetics*, 4th completely rev. and greatly enl. ed., Wiley-VCH, Weinheim.

[36] Hammes-Schiffer, S. (2002) Comparison of hydride, hydrogen atom, and proton-coupled electron transfer reactions, *Chemphyschem 3*, 33-42.

[37] Liu, D., Karsten, W. E., and Cook, P. F. (2000) Lysine 199 is the general acid in the NAD-malic enzyme reaction, *Biochemistry 39*, 11955-11960.

[38] Keenholtz, R. A., Mouw, K. W., Boocock, M. R., Li, N. S., Piccirilli, J. A., and Rice, P. A. (2013) Arginine as a general acid catalyst in serine recombinase-mediated DNA cleavage, *J Biol Chem 288*, 29206-29214.

[39] Shoemark, D. K., Cliff, M. J., Sessions, R. B., and Clarke, A. R. (2007) Enzymatic properties of the lactate dehydrogenase enzyme from Plasmodium falciparum, *The FEBS journal 274*, 2738-2748.

[40] Forlani, G., Giberti, S., Berlicki, L., Petrollino, D., and Kafarski, P. (2007) Plant P5C reductase as a new target for aminomethylenebisphosphonates, *J Agric Food Chem 55*, 4340-4347.

[41] Buehner, M., Ford, G. C., Olsen, K. W., Moras, D., and Rossman, M. G. (1974) Three-dimensional structure of D-glyceraldehyde-3-phosphate dehydrogenase, *J Mol Biol 90*, 25-49.

[42] Branden, C. I., and Tooze, J. (1991) *Introduction to protein structure, Chapter 10*, Garland Publishing Inc., New York.

[43] Sang, P., Hu, W., Ye, Y.-J., Li, L.-H., Zhang, C., Xie, Y.-H., and Meng, Z.-H. (2017) In silico screening, molecular docking, and molecular dynamics studies of SNP-derived human P5CR mutants, *Journal of Biomolecular Structure and Dynamics 35*, 2441-2453.

[44] Stec, B. (2013) Time passes yet errors remain: comments on the structure of N10-formyltetrahydrofolate synthetase, *Protein Sci 22*, 671-674.

[45] Weichenberger, C. X., Pozharski, E., and Rupp, B. (2013) Visualizing ligand molecules in Twilight electron density, *Acta Crystallogr Sect F Struct Biol Cryst Commun 69*, 195-200.

[46] Weiss, M. S., Diederichs, K., Read, R. J., Panjikar, S., Van Duyne, G. D., Matera, A. G., Fischer, U., and Grimm, C. (2016) A critical examination of the recently reported crystal structures of the human SMN protein, *Hum Mol Genet 25*, 4717-4725.

[47] Muller, Y. A. (2013) Unexpected features in the Protein Data Bank entries 3qd1 and 4i8e: the structural description of the binding of the serine-rich repeat adhesin GspB to host cell carbohydrate receptor is not a solved issue, *Acta Crystallogr Sect F Struct Biol Cryst Commun 69*, 1071-1076.

[48] Celeste, L., Lovelace, L., and Lebioda, L. (2013) Response to Boguslaw Stec's letter to the editor of Protein Science, *Protein Sci 22*, 675-676.

[49] Celeste, L. R., Chai, G., Bielak, M., Minor, W., Lovelace, L. L., and Lebioda, L. (2012) Mechanism of N10-formyltetrahydrofolate synthetase derived from complexes with intermediates and inhibitors, *Protein Sci 21*, 219-228.

[50] Wlodawer, A., Minor, W., Dauter, Z., and Jaskolski, M. (2013) Protein crystallography for aspiring crystallographers or how to avoid pitfalls and traps in macromolecular structure determination, *FEBS J 280*, 5705-5736.

[51] Edwards, M. A., and Roy, S. (2017) Academic Research in the 21st Century: Maintaining Scientific Integrity in a Climate of Perverse Incentives and Hypercompetition, *Environ Eng Sci 34*, 51-61.

[52] Deller, M. C., and Rupp, B. (2015) Models of protein-ligand crystal structures: trust, but verify, *J Comput Aided Mol Des 29*, 817-836.

[53] Pozharski, E., Weichenberger, C. X., and Rupp, B. (2013) Techniques, tools and best practices for ligand electron-density analysis and results from their application to deposited crystal structures, *Acta Crystallogr D Biol Crystallogr 69*, 150-167.

Chapter 3

Kinetic and Structural Characterization of the Enzyme Mechanism of wild-type HsPYCR2 and Disease Variants

ABSTRACT

Pyrroline-5-carboxylate reductase (PYCR) catalyzes the final step of L-proline biosynthesis by reducing L-P5C into L-proline using NAD(P)H as the hydride donor (Fig. 3.1). In humans, three isoforms (PYCR1, PYCR2, and PYCRL) are known. Human PYCR1 and PYCR2 are localized in the mitochondrion and share 84% amino acid sequence identity, yet interestingly different disease symptoms are found in patients that have mutations in PYCR1 or PYCR2. Recent genome-wide association and clinical studies have revealed that homozygous mutations in human PYCR2 lead to postnatal microcephaly and hypomyelination, including hypomyelinating leukodystrophy type 10. To uncover biochemical and structural insights into human PYCR2, we characterized the steady-state kinetics of wild-type enzyme along with two mutant variants, Arg119Cys and Arg251Cys, that were previously identified in patients with microcephaly and hypomyelination. Here we establish the substrate binding order for the human PYCR2 mechanism and report the biochemical penalties of the PYCR2 disease variants. Structural insights into human PYCR2 were also inferred by examining the X-ray crystal structure of human PYCR1. From this model, Arg119 and Arg251 are predicted to be important for the catalytic activity and structural stability of PYCR2, respectively, which supports our kinetic assays showing a 164-fold loss in catalytic activity for the Arg119Cys mutant relative to wild-type enzyme. The Arg251Cys mutation has a profound effect on the thermostability and secondary

structure of human PYCR2 as determined by fluorescence-based thermal shift assays and circular dichroism, respectively. The PYCR2 disease variants are concluded to impair PYCR2 function in patients by significantly lowering catalytic activity (Arg119Cys) and stability (Arg251Cys).

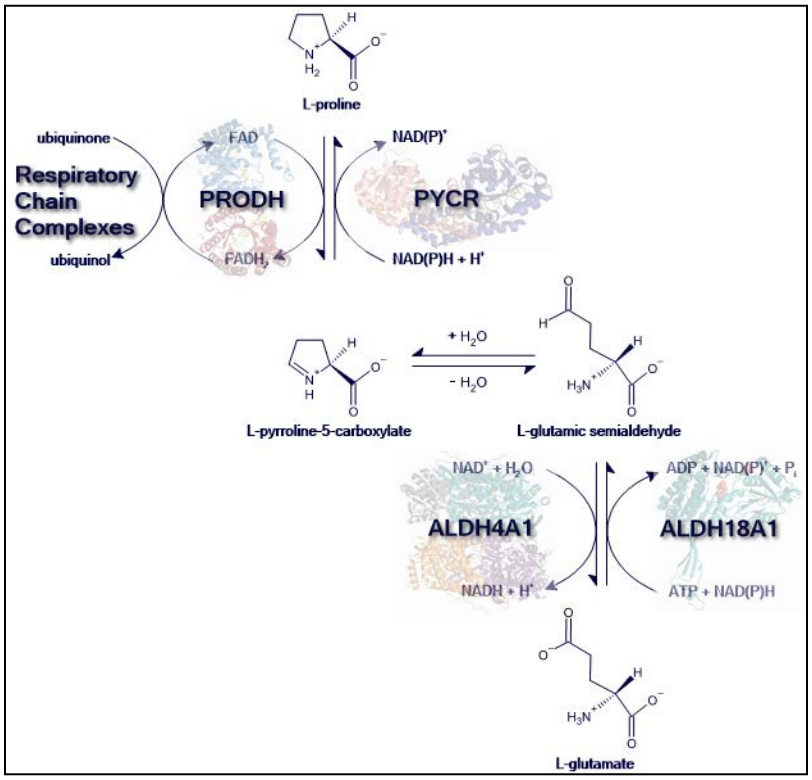

Figure 3.1. Enzymatic reactions of L-proline metabolism in the mitochondrion. Structural images are PyMol renderings of the following X-ray crystal structures: dimeric TtPRODH (PDB code 2EKG), dimeric HsPYCR1 (PDB code 5UAV), tetrameric HsALDH4A1 (PDB code 4OE5), and monomer of the L-glutamyl-γ-5-phosphate reductase domain of HsALDH18A1 (PDB code 2H5G).

INTRODUCTION

Delta-1-pyrroline-5-carboxylate reductases (PYCRs or P5CRs) have been identified as important housekeeping enzymes of L-proline (L-Pro) biosynthesis and are broadly distributed across all three domains of life (eukaryota, bacteria, and archaea).[1] L-proline is synthesized from L-glutamate by the sequential action

of L-Δ^1-pyrroline-5-carboxylate synthase (a.k.a. aldehyde dehydrogenase 18A1, ALDH18A1) and PYCR as shown in Fig. 3.1. L-proline is converted back to L-glutamate via L-proline dehydrogenase (PRODH) and L-glutamic-γ-semialdehyde dehydrogenase (GSALDH) (a.k.a. aldehyde dehydrogenase 4A1, ALDH4A1) as shown in Fig. 3.1. Both pathways share the intervening L-pyrroline-5-carboxylate (L-P5C)/L-glutamic semialdehyde (L-GSAL) equilibrium step.

In terms of the current state of knowledge for human PYCR (HsPYCR, EC 1.5.1.2), a 2012 study on L-proline biosynthesis from melanoma tissue extracts characterized three separate human genes encoding isozymes PYCR1, PYCR2, and PYCRL (a.k.a. PYCR3).[2] Subcellular localization studies identified HsPYCRL as a cytosolic enzyme whereas HsPYCR1 and HsPYCR2 were identified as mitochondrial enzymes.[2] Pairwise global sequence alignment[3] of HsPYCR1 (NCBI ref seq NP_008838.2, UniProtKB P32322) and HsPYCR2 (NCBI ref seq NP_037460.2, UniProtKB Q96C36) indicates 84.4% amino acid sequence identity between the two proteins. To date, structural knowledge of PYCR consists of 20 total X-ray crystal structures from seven organisms (*Homo sapiens*, *Bacillus cereus*, *Coxiella burnetii*, *Streptococcus pyogenes*, *Neisseria meningitides*, *Plasmodium falciparum*, and *Medicago truncatula*) deposited in the Research Collaboratory for Structural Bioinformatics-Protein Data Bank.[4] Thus far, two sets of X-ray crystal structures of human PYCR have been reported in the literature.[5, 6] The most recent is a 1.85 Å X-ray crystal structure determined by Christensen et al. (2017) of the ternary complex of HsPYCR1 + NADPH + L-proline analog, L-tetrahydro-2-furoic acid (L-THFA) (PDB code 5UAV).[6] The structure by Christensen et al. resolved the location of the enzyme active site with

NADPH binding in the canonical Rao-Rossmann motif GXGXXA/G[7] at the N-terminus, which is consistent with known X-ray crystal structures of PYCR from plants and bacteria.[8] Although progress has been made on the structural and functional characterization of HsPYCR1, considerably less is known about HsPYCR2, which is the focus of this work.

L-proline biosynthesis has been implicated in different types of cancers. Besides supporting protein synthesis, L-proline biosynthesis has been shown to promote tumorigenesis by providing $NAD(P)^+$ redox equivalents to support aerobic glycolysis and the oxidative branch of the pentose phosphate pathway.[9] Upregulation of HsPYCR2 has been found in different cancers such as melanoma, breast, prostate, esophageal tumors, lung metastasis, Kaposi's sarcoma and primary effusion lymphoma, and cervical cancer.[2,10,11,12,13] In a mass spectrometry-based screening of metabolites in tissue sections from 256 esophageal squamous cell carcinoma (ESCC) patients, Sun et al. (2019) found a significant upregulation of L-Pro metabolism in the cancer region compared to the normal epithelium and muscle regions.[11] Immunohistochemistry staining of the ESCC tissue sections identified HsPYCR2 as the most enriched metabolic enzyme in the cancer region, consistent with increased L-proline found in the same tissue region.[11] In two separate human melanoma cell lines, tumor cell death was induced by silencing HsPYCR2 expression, indicating a critical role for HsPYCR2 in cancer cells.[14]

More recently, Choi et al. (2020) verified a role for HsPYCR2 in Kaposi's sarcoma cells. With GST-tag pull down assays and mass spectrometry analysis, the authors showed that Kaposi's sarcoma-associated herpesvirus K1

oncoprotein binds endogenous human PYCR2 to commandeer L-proline biosynthesis for increased intracellular L-Pro concentration that promotes in vitro 3D spheroid culture and in vivo tumorigenesis.[12] From a kinetic standpoint, the authors also demonstrated that the presence of viral K1 protein not only activated and enhanced PYCR2 enzymatic affinity with L-P5C substrate with a 4-fold decrease in the K_M value, but also the viral K1 protein curtailed L-Pro product- or ATP-mediated competitive inhibition of PYCR2.[12] In the clinical setting of one hospital in Bangkok, Thailand, Keeratichamroen et al. (2020) recently conducted a pilot study examining changes in disease-relevant proteins in 31 patients with human papilloma virus (HPV)-associated cervical cancer compared with 16 healthy control patients using immunoaffinity-depleted serum processing of blood samples followed by liquid chromatography mass spectrometry analysis.[13] Through the use of capillary electrophoresis-based western blot analysis and receiver operating characteristic curves data analysis to quantify serum levels of the candidate protein biomarkers for the detection of HPV-associated cervical cancer, the authors identified high expression levels of PYCR2 in patients with advanced-stage III-IV cervical cancer compared to either patients with early-stage I-II cervical cancer or with HPV positive normal controls, in a statistically significant manner.[13] In lieu of the current standard of practice for cervical cancer screening tests including the Papanicolaou smear, visual inspection with acetic acid, HPV DNA testing, and liquid-based cytology, the authors conjecture that this unprecedented association between PYCR2 expression levels and cervical cancer in tandem with the quantification of five other serum protein biomarkers (A1AT, TTR, ApoA-I, VDBP, and MMRN1) can serve as a minimally invasive yet

highly sensitive and specific screen for the detection of HPV-associated cervical cancer.[13]

Autosomal recessive disorders of HsPYCR1 and HsPYCR2 have been specifically linked to hypoprolinemia, cutis laxa and progeroid syndrome, microcephaly, and neurological disorders. More specifically, mutations in HsPYCR1 generally lead to cutis laxa type IIB (OMIM # 612940)[15] whereas mutations in HsPYCR2 are uniquely linked to genetic hypomyelinating leukodystrophy type 10 with microcephaly (OMIM # 616420).[16,17,18] Thus, it has been suggested that PYCR1 mutations are most strongly associated with skin disorders while PYCR2 mutations appear more prominent in neurological disorders.[18] In a study by Zaki et al. (2016) of HsPYCR2 mutations in patients with lethal microcephaly, loss of HsPYCR2 was proposed to impair mitochondria function and disrupt oxidative balance, namely $NAD(P)^+$ levels.[18] Thus it appears HsPYCR2 not only helps drive the cellular supply of L-proline, but it also performs redox cycling of $NAD(P)H/NAD(P)^+$ to support cellular growth, which can have profound effects in different disease contexts such as in cancers with upregulated HsPYCR2 or neurological disorders associated with HsPYRC2 variants.

The need to investigate HsPYCR2 and disease variants stems in part from a study by Nakayama et al. (2015) which showed that two families of human patients were affected by the same allelic autosomal-recessive condition in the *PYCR2* gene.[17] Two HsPYCR2 variants, R119C and R251C, were each identified by a genome-wide association study to have a statistically significant linkage to the observed neurological traits of hypomyelination and microcephaly in the patients. These findings, along with the growing recognition of HsPYCR2 being

implicated in different cancers (non-small cell lung cancer, viral-related hepatocellular carcinoma, papillary renal cell carcinoma, melanoma, breast and prostate cancers, and esophageal squamous cell carcinoma, Kaposi's sarcoma, and cervical cancer)[19,20,21,14,9,11,12,13] motivated our investigation of the kinetic mechanism of wild-type HsPYCR2 and the biochemical penalties of the clinically relevant R251C and R119C mutations on HsPYCR2 function. Here we report the steady-state kinetic parameters of HsPYCR2 wild-type and mutants R251C and R119C along with thermostability and secondary structure analysis. Product(s) inhibition studies of wild-type HsPYCR2 indicate a sequential-order binding mechanism with L-P5C binding first.

MATERIALS AND METHODS.

Materials and Reagents

Milli-Q Ultrapure water was used for all experiments. The following reagents were purchased from Millipore-Sigma: DL-5-hydroxylysine hydrochloride, sodium metaperiodate, Dowex 50WX4 hydrogen form (200-400 mesh) cation exchange resin, NaH_2PO_4, ε-amino-N-caproic acid, N-tosyl-L-phenylalanine chloromethyl ketone, bovine serum albumin, nicotinamide adenine dinucleotide phosphate reduced form (NADPH), nicotinamide adenine dinucleotide reduced form (NADH), and ammonium fluoride (NH_4F). The following reagents were from Fisher Scientific: LB Agar Miller, ampicillin, yeast extract, NaOH, NaCl, 2-[4-(2-hydroxyethyl)piperazin-1-yl]ethanesulfonic acid (HEPES), and ethylenediamine tetraacetic acid (EDTA) disodium salt. Glycerol and tryptone were purchased from Research Products International. Reagents β-octyl-D-glucopyranoside (β-OG) and L-proline were from Combi-Blocks. Ethanol (190- or 200-proof) was

from Decon Labs. Tris(hydroxymethyl)aminomethane (Tris), glycine, isopropyl β-D-thiogalactopyranoside (IPTG), phenylmethylsulfonyl fluoride (PMSF), leupeptin hemisulfate, and NAD^+ were purchased from Gold Biotechnology. Imidazole and (O)2-aminobenzaldehyde (*o*-AB) were purchased from Acros Organics, and hydrochloric acid (HCl) 34-37% OmniTrace was purchased from EMD-Millipore.

DL-P5C synthesis

DL-P5C was synthesized according to the protocol by Williams and Frank,[22] which involved the metaperiodation of DL-5-hydroxylysine hydrochloride at 4 °C with the reaction product purified by Dowex 50WX4 cation exchange column chromatography using 1 M HCl to elute the fractions of DL-P5C. Synthesized DL-P5C was quantified using the *o*-AB assay in which DL-P5C and *o*-AB react to form a yellow conjugate that is measured at 443 nm (ε_{443} = 2590 M^{-1} cm^{-1}).[23] DL-P5C stock solutions were stored in 1 M HCl at 4 °C. DL-P5C as the main reaction product was confirmed by liquid chromatography-electrospray ionization-multiple reaction monitoring (LC-ESI-MRM) mass spectrometry. Additional details concerning the synthesis and mass spectrometry characterization of DL-P5C are provided in Appendix A.

Site-Directed Mutagenesis of HsPYCR2

The DNA sequence encoding human (Homo sapiens) PYCR2 transcript variant 1 (NCBI RefSeq NM_013328.3) was subcloned into the pKA8H vector at the BamHI and NdeI sites with a N-terminal 8x-Histidine tag (pKA8H/HsPYCR2). The pKA8H/HsPYCR2 construct includes an ampicillin resistance marker gene and was used as a template for generating mutants R119C and R251C. We used a modified protocol from the GeneTailor Site-Directed Mutagenesis System

(Invitrogen, Life Technologies) to introduce mutations via overlapping mutagenic and non-mutagenic sequence PCR-based reactions. Primers were generated using New England BioLabs NEBaseChanger online tool and Eurofins Genomics oligonucleotide primer synthesis services. Forward mutagenic primers consisted of an overlapping region, the mutation site, and an extended region, whereas the reverse non-mutagenic primers consisted of a complementary overlapping region and an extended region. The 21-bp forward 5'-TGGGGGCTTC**TGC**TCTCTGCT-3' and reverse 5'-CTCTCTAGAAAGTGCAGGGCG-3' primers were used for generating the R251C mutant, and the 29-bp forward 5'-CAAAGTGATT**TGC**TGCATGACCAACACAC-3' and 18-bp reverse 5'-GGGGCTGGCTGGAATGCC-3' primers were used for generating the R119C mutant. The triplet codon of the mutation site is underlined in bold for each forward primer. The wild-type and mutant constructs were confirmed by DNA sequencing of the entire *PYCR2* gene insert.

Expression and purification of HsPYCR2 wild-type and mutants

The pKA8H/HsPYCR2 constructs for wild-type and the R251C and R119C mutant proteins were transformed into *E. coli* BL21 (DE3) pLysS competent cells (Novagen-EMD Millipore Sigma) for recombinant protein expression. Cells were grown on LB Agar Miller plates containing 50 µg/ml ampicillin and 34 µg/ml chloramphenicol (Chem-Impex International). Starter cultures from the growth plates were then made in LB broth, grown overnight and used to inoculate six 1 L-cultures of Terrific Broth (TB) media (prepared from recipe in Sambrook et al. (1989) consisting of tryptone, yeast extract, glycerol, and water)[24], which also contained 50 µg/ml ampicillin and 34 µg/ml chloramphenicol. The 1-L cultures

were grown at 37 °C (180 rpm) until reaching an optical density at 600 nm (OD_{600}) ≈ 0.8-1.0. The temperature was then lowered to 18 °C and IPTG (0.4 mM final concentration) was added to the cultures to induce recombinant protein expression. After induction with IPTG for 10 h (18 °C, 180 rpm), cultures were then treated with 100 µg/ml chloramphenicol with continued shaking at 180 rpm at 18 °C for an additional 2 h. The chloramphenicol treatment was found to improve the solubility of the HsPYCR2 proteins, as chloramphenicol was previously reported to enhance chaperone-assisted folding of target proteins.[25] Cells were then harvested by centrifugation (5400 x g) (Avanti J-E High-Speed Centrifuge, Beckman Coulter) for 20 min at 4 °C. Cell pellets were stored at -80 °C. Upon thawing, the cell pellets were resuspended in NPI-5 cell lysis buffer (5 mM imidazole, 500 mM NaCl, 50 mM NaH_2PO_4, pH 7.5) containing 500 µM Tris(3-hydroxypropyl)phosphine (THPP) reducing agent (Strem Chemicals), 0.01% TritonX-100 detergent (Amresco), 0.01% Brij-35 polyoxyethylene detergent (Santa-Cruz Biotechnology), 10 mM β-OG, and five protease inhibitors (ε-amino-N-caproic acid, phenylmethylsulfonyl fluoride, leupeptin hemisulfate, N-tosyl-L-phenylalanine chloromethyl ketone and N-α-p-tosyl-L-lysine chloromethyl ketone). The cell suspension was then sonicated for 5 min with 5 sec on and 15 sec off pulse settings using a Sonic Dismembrator (Model F 550, Fisher Scientific). The resulting cell lysates were centrifuged (30960 x g) for 1.5 h at 4 °C to obtain the supernatant with the HsPYCR2 protein.

HsPYCR2 proteins were purified at 4 °C by immobilized metal affinity column chromatography using a Ni^{2+}-NTA Superflow resin (Qiagen). A stepwise gradient of 5 mM, 60 mM, and 500 mM imidazole in 50 mM NaH_2PO_4-based column

buffers was used to elute the HsPYCR2. Eluted fractions were analyzed by sodium dodecyl sulfate poly-acrylamide gel electrophoresis (SDS-PAGE) using (β)2-mercaptoethanol (Acros Organics) as a reducing agent. Fractions containing HsPYCR2 were pooled and dialyzed (10 kDa molecular weight cutoff (MWCO) Dialysis Snakeskin Tubing, ThermoFisher Scientific-Pierce Biotech) into 50 mM HEPES (pH 7.5) buffer containing 250 mM NaCl, 0.5 mM EDTA, 500 µM THPP, and 10 % (v/v) glycerol. HsPYCR2 proteins were concentrated using an ultrafiltration stirrer cell (Model 8050, Amicon, EMD Millipore-Sigma) and a 5 kDa PLCC low bind 44.5 mm diameter ultrafiltration disc (EMD Millipore-Sigma) at 4 °C until the protein solution volume was reduced to approximately 5 ml. Aliquots of 1 ml were then placed into 2 ml microtubes and flash-frozen in liquid nitrogen. The tube lids were subsequently pierced with fine needle and the frozen samples were then further concentrated by freeze-dry vacuum lyophilization (FreeZone Bulk Tray Dryer, Labconco) for 3-5 h until the volume was reduced to 250 µl. The resulting concentrated protein was next exchanged into fresh 50 mM HEPES (pH 7.5) buffer as described above by microdialysis using inverted 15kDa MWCO Tube-O-Dialyzer tubes (G Biosciences-Geno Technology). Protein concentration was quantified by the 660 nm Pierce Protein Dye Assay (ThermoFisher Scientific-Pierce Biotech) as per manufacturer's instructions. Finally, all protein samples were flash-frozen in liquid nitrogen in 500 µl aliquots and stored at -80 °C. Proteins were analyzed by SDS-PAGE under reducing conditions on a 4-20 % gradient gel and visualized using Bio-Safe Coomassie Blue G250 stain (Fig. 3.2). The N-terminal 8x-His tag was retained in all the purified HsPYCR2 proteins. A more thorough description of methods and procedures used for HsPYCR2

protein purification can be found in Appendix B.

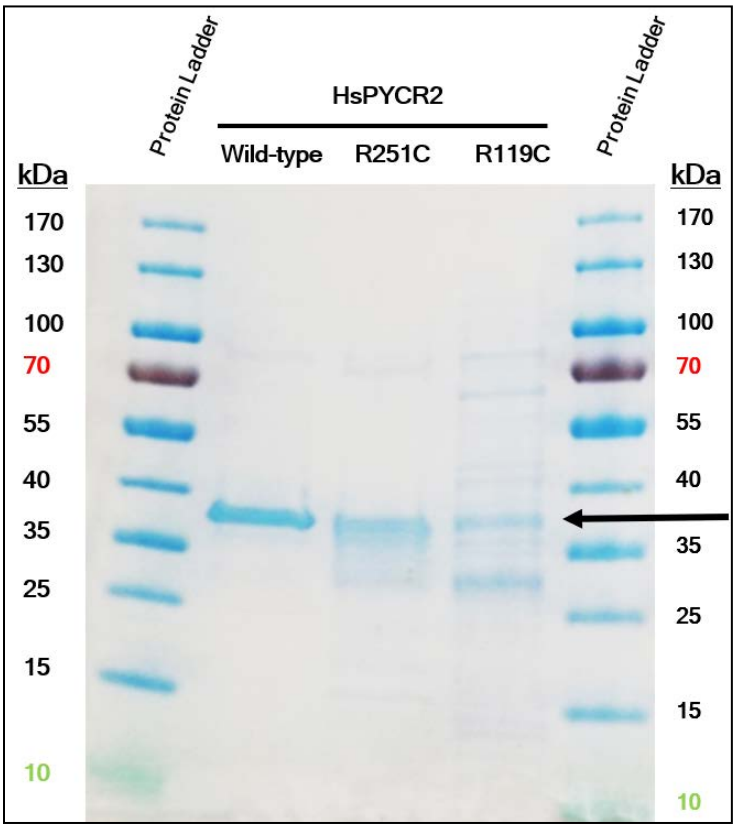

Figure 3.2. SDS-PAGE of HsPYCR2 enzymes. HsPYCR2 wild-type (2 µg), and R251C (10 µg) and R119C mutant (2 µg) enzymes (each in 50 mM HEPES (pH 7.5) buffer containing 250 mM NaCl, 0.5 mM EDTA, 10% (v/v) Glycerol, 500 µM THPP reducing agent) were mixed with denaturing loading dye buffer (50 mM Tris-HCl pH 6.8, 2% SDS, 10% Glycerol, 0.02% Bromophenol Blue, and 10% β(2)-Mercaptoethanol). Samples were thermally denatured at 100 °C and then loaded onto a 4-20% gradient precast polyacrylamide-Tris-Gly HCl, 10-well MP TGX gel (Bio-Rad). After the electrophoresis of the gel, it was stained with Bio-Safe Coomassie Blue G250 (Bio-Rad). The PageRuler Prestained Protein Ladder (ThermoFisher Scientific) was used as reference to estimate the molecular weight of the HsPYCR2 wild-type and mutant enzymes (each containing an N-terminal (8x)His-tag). The predicted molecular weight of the HsPYCR2 polypeptides is 36.1 kDa, which is consistent with the observed band (black arrow) immediately above the 35 kDa marker.

Kinetic characterization of HsPYCR2 enzymes

Kinetics assays of HsPYCR2 were performed at 37 °C in 0.1 M Tris-HCl (pH 7.5) reaction buffer containing 0.01% Brij-35 detergent and 1 mM EDTA using a

protocol modified from previous studies.[26,8,27,28] The catalytic activity of HsPYCR2 wild-type and mutants R251C and R119C were monitored by measuring the L-P5C-dependent oxidation of NAD(P)H at 340 nm and at 380 nm, using millimolar extinction coefficients 6.22 mM^{-1} cm^{-1} and 1.314 $mM^{-1}cm^{-1}$, respectively.[29,2] The concentrations of NADPH and NADH along with $NADP^+$ (VWR International) and NAD^+ in 10 mM Tris-HCl pH 8 buffer, were spectrophotometrically determined and stored at -80 °C. DL-P5C substrate solution stored at 4 °C in 1 M HCl, was neutralized to pH 7.5 just prior to enzyme assays by adding 1 M Tris-HCl (pH 9.0) buffer. NAD(P)H was varied (0-580 µM) while holding DL-P5C fixed at 5000 µM and, DL-P5C was varied (0-5500 µM) while holding NAD(P)H fixed at 500 µM. NAD^+ product inhibition assays were performed by holding DL-P5C constant (5000 µM) while varying NADH (0-580 µM) at different NAD^+ concentrations (0-500 µM). L-Pro inhibition assays were conducted by holding NADH constant (500 µM) and varying DL-P5C (0-5500 µM) at different L-Pro concentrations (0-500 µM). For assays in which DL-P5C was varied, the ionic strength was maintained at approximately 450-480 mM $Tris^+Cl^-$ at each DL-P5C concentration by adding a balance of 1 M Tris-HCl (pH 7.5). The final assay volume was 600 µl in 1.5 ml rectangular polystyrene cuvettes (1 cm pathlength) (USA Scientific). Reactions were prewarmed at 37 °C and initiated by adding the enzyme last. The absorbance decrease due to oxidation of NAD(P)H was monitored at 340 and 380 nm in a Varian Cary Bio 50 UV-Vis Spectrophotometer (Agilent Technologies) against blanks from which the varied substrate had been omitted. Final concentrations of enzyme used in the assays were 0.06 µM wild-type, 0.6 µM R251C mutant, and 3 µM R119C mutant.

Enzyme activity was calculated from the linear portion of the initial absorbance decrease using the Beer-Lambert-Bouguer law.[30,31,32] Assays were performed in triplicate and data were expressed as mean ± standard deviation. Data were fit by nonlinear regression to the Henri-Michaelis-Menten equation using SigmaPlot 12.0 (version 12.0.0.182, Systat Software) to estimate the theoretical maximal velocity limit (V_{lim}) and the apparent Michaelis-Menten constant (K_M^{app}) values (value ± standard error). The K_M^{app} for L-P5C was assumed to be half the K_M^{app} value for the racemic DL-P5C mixture. The apparent catalytic turnover rate (k_{cat}^{app}) and substrate specificity constant or catalytic efficiency values (k_{cat}^{app}/K_M^{app}) were calculated from V_{lim} and K_M^{app}. Product(s) inhibition kinetics were analyzed by global fitting of the data to different inhibition models using Enzyme Kinetics Wizard Module in SigmaPlot 12.0 and by Hanes-Woolf plot analysis. For NAD^+ product inhibition, the data fit best to a mixed inhibition (Full) model with enzyme-inhibition constants K_{IC}^{app} and $K_{IU}^{app} = \alpha(K_{IC}^{app})$ ($\alpha = 0.4112$). The mixed inhibition model had the highest squared correlation coefficient (R^2)-ranking among eight tested inhibition models. For L-Pro product inhibition, the highest R^2-ranking model was competitive inhibition (Full).

Thermal Stability Assays

Thermofluor assays were used to determine the thermal stabilities of wild-type HsPYCR2 and the mutants. Thermal stabilities of wild-type, R251C, and R119C were measured in 50 mM HEPES (pH 8.0) buffer containing 150 mM NaCl, 0.5 mM EDTA, 500 µM THPP reducing agent, and 10 % (v/v) glycerol. Assays were performed in a 50 µl reaction volume using white 8-strip 0.2 ml PCR tubes with

individual flat optically clear caps (Phenix Research Products). The reaction mixtures included 6.4 µM of HsPYCR2 wild-type and mutant enzymes, various single additions and combinations of 1 mM NADH, 1 mM DL-P5C (pH 7.5), 1 mM NAD^+, and 1 mM L-Pro (pH 8.0), and the reaction volume balanced with 100 mM potassium phosphate (pH 7.0) buffer. Sypro Orange fluorescent dye (λ_{ex} = 470 nm, λ_{em} = 570 nm, Molecular Probes) was added last at (25X) final concentration strength, and then the PCR tubes were covered with aluminum foil to protect from light during mild agitation using a rocking shaker for 4 h at 4 °C.

Next, a mini plate spinner (Model MPS C1000, LabNet) was used for 60 sec at 2500 rpm to force liquid contents towards the bottom of the tubes. Sample tubes were then loaded into an iCycler chassis (Bio-Rad) to initiate data collection using the MyiQ Single-Color Real-Time PCR Detection System with optics module (CCD camera bandpass optical Filter 2 position at (λ_{ex} = 485 ± 20 nm, λ_{em} = 530 ± 30 nm)) using iQ5 Optical System software (Bio-Rad, version 2.1). Thermal denaturation curves were recorded using a 10 min thermal equilibration period at 20 °C followed by increasing temperature increments at 0.2 °C per 15 sec from 20-90 °C. The instrument's software provided overlay plots of relative fluorescence units (RFU) vs. temperature (T) and of (-d(RFU)/dT) vs. T. From the raw numerical data, mean values of triplicate control blank curves without the enzyme were subtracted from corresponding mean values of quadruplicate curves with the enzyme for data analysis using Microsoft Excel 2017 and SigmaPlot 12.0.

The data was fit to a non-linear Boltzmann model:

$$f = \frac{y_0 + (a - y_0)}{\left(1 + e^{\left(\frac{-(x-x_0)}{b}\right)}\right)}$$

where f is the fluorescence intensity at temperature x, y_0 and a are pretransitional and posttransitional fluorescence intensities, respectively, and b is a slope factor. Analysis of the Boltzmann model fit curve facilitated determination of x_0 as the melting point temperature (T_m) that occurs at the midpoint of inflection in the unfolding transition of (RFU vs. T) plots. Statistical comparisons between paired groups of data were performed using Student's t-test calculations in Microsoft Excel 2017 with $p < 0.05$ and at 95% confidence level considered statistically and significantly different.

Circular Dichroism (CD) Spectroscopy

Wild-type HsPYCR2 and mutants R251C and R119C were microdialyzed into 10 mM NaH_2PO_4 (pH 8.0) containing 250 mM NH_4F buffer for 16 h at 4 °C. Then, 1200 µl of each protein sample (final concentration 4 µM) was loaded into an individual 0.01 cm-optical length micro-cylindrical Suprasil cell (Starna Cells) and spectra in the far UV wavelength range of 180-260 nm were collected at 22 °C using a CD spectrophotometer (Jasco, Model J-815) with Spectra Manager software (Jasco, version 2.10.01). Averaged baseline scans of buffer alone were measured before averaged sample scans of each protein sample. Instrument scanning parameters were 0.5 nm data pitch interval, standard sensitivity, 4-sec data integration averaging time, bandwidth = 1.00, continuous scan mode with scanning speed of 100 nm/min, baseline correction = baseline measured, and accumulation scans = 16. The raw data was converted into Mean Residue

Ellipticity (θ, in units deg cm^2 $dmol^{-1}$) using the following equation:

Mean Residue Ellipticity =

$$\left(\frac{\text{(CD Jasco value in units mdeg)} \times \left(\frac{1 \text{ deg}}{10^3 \text{ mdeg}} \right)}{\text{(0.01 cm pathlength)} \times \text{(4 μM)} \times \left(\frac{1 \text{ μmol}}{1 \text{ μM} \cdot 1 \text{ L}} \right) \times \left(\frac{1 \text{ mol}}{10^6 \text{ μmol}} \right) \times \left(\frac{10 \text{ dmol}}{1 \text{ mol}} \right) \times \left(\frac{1 \text{ L}}{10^{-3} \text{m}^3} \right) \times \left(\frac{1 \text{m}^3}{10^6 \text{cm}^3} \right) \times \text{(340 aa residues)}} \right)$$

Secondary structure elements (8 individual components) for each protein were determined from a mathematical fit to the experimental CD spectra (190-250nm) using the online BeStSel algorithm.[33] The CD spectra (plotted as Mean Residue Ellipticity (θ) in units deg cm^2 $dmol^{-1}$ vs. Wavelength (λ) in units nm) and corresponding high tension (HT) voltage spectra of HsPYCR2 wild-type and mutants R119C and R251C (codes CD0006228000, CD0006229000, and CD0006230000, respectively) have been deposited in the publicly accessible Protein Circular Dichroism Data Bank (http://pcddb.cryst.bbk.ac.uk).

RESULTS

Steady-state Kinetic Parameters of HsPYCR2 Wild-type and Mutants

In previous studies, the enzymatic activity of the inherited HsPYCR2 mutants leading to microcephaly and hypomyelination in human patients was not reported. Proline levels in patients were found to be normal by plasma amino acid analysis, suggesting proline depletion was not a biochemical factor in the pathophysiology.[17,18,34] However, cells harboring the HsPYCR2 mutants exhibited higher apoptosis rates under oxidative stress and were characterized by a lower mitochondrial membrane potential.[17] To provide further insight into the biochemical penalties of the R119C and R251C mutations, we determined the steady-state kinetic parameters of HsPYCR2 wild-type and mutants with respect to L-P5C and NAD(P)H substrates.

Table 3.1 provides the kinetic parameters for HsPYCR2 wild-type and mutants R251C and R119C.

Table 3.1. Steady-state kinetic parameters for HsPYCR2[a]

Enzyme	Varied Substrate	Fixed Substrate	K_M^{app} (μM)	k_{cat}^{app} (s^{-1})	(k_{cat}^{app}/K_M^{app}) (M^{-1} s^{-1})
Wild-type[b]	DL-P5C	NADH[e]	1509 ± 69[g]	61.3 ± 1.4	(41 ± 2) x 10^3
	DL-P5C	NADPH[e]	994 ± 134[g]	26.0 ± 1.5	(26 ± 4) x 10^3
R251C[c]	DL-P5C	NADH[e]	1315 ± 291[g]	3.2 ± 0.3	(2.4 ± 0.6) x 10^3
	DL-P5C	NADPH[e]	1499 ± 152[g]	3.1 ± 0.1	(2.1 ± 0.2) x 10^3
R119C[d]	DL-P5C	NADH[e]	317 ± 90[g]	0.08 ± 0.01	(0.25 ± 0.08) x 10^3
	DL-P5C	NADPH[e]	334[g,h]	0.13[h]	0.4[h] x 10^3
Wild-type[b]	NADH	DL-P5C[f]	298 ± 73	47.9 ± 5.3	(161 ± 44) x 10^3
	NADPH	DL-P5C[f]	216 ± 17	24.0 ± 0.7	(111 ± 9) x 10^3
R251C[c]	NADH	DL-P5C[f]	953 ± 321	5.9 ± 1.4	(6.2 ± 2.5) x 10^3
	NADPH	DL-P5C[f]	119 ± 10	1.8 ± 0.1	(15 ± 1) x 10^3
R119C[d]	NADH	DL-P5C[f]	34 ± 5	0.015 ± 0.001	(0.44 ± 0.07) x 10^3
	NADPH	DL-P5C[f]	537[h]	1.5[h]	2.8[h] x 10^3

[a]Value ± std error are the apparent best-fit parameters from non-linear least-squares fit of the data to the Henri-Michaelis-Menten equation using SigmaPlot 12.0 (version 12.0.0.182, Systat Software). Data plotted as the (mean ± SD) of n=3 technical replicates.
[b]Final enzyme concentration of 0.06 μM in the assay.
[c]Final enzyme concentration of 0.6 μM in the assay.
[d]Final enzyme concentration of 3 μM in the assay.
[e]NAD(P)H concentration fixed at 500 μM.
[f]DL-P5C concentration fixed at 5000 μM.
[g]Reported value is the concentration of L-P5C, which is assumed to be half the concentration of the DL-P5C racemic mixture.
[h](Values) are the apparent best-fit parameters from non-linear least-squares fit of the data (single replicate, n=1) to the Henri-Michaelis-Menten equation using SigmaPlot 12.0.

Wild-type HsPYCR2 did not show a strong preference for NADH or NADPH when keeping L-P5C fixed as indicated by similar apparent k_{cat}/K_M values of (160 ± 44) x 10^3 M^{-1} s^{-1} and (111 ± 9) x 10^3 M^{-1} s^{-1}, respectively. Accordingly, wild-type

HsPYCR2 displayed similar k_{cat}/K_M values when varying L-P5C and keeping NADH or NADPH constant. These findings contrast with a previous study by De Ingeniis et al. in which HsPYCR2 was reported to have 2.5-fold higher activity with NADH relative to NADPH.[2] Both HsPYCR2 mutants R251C and R119C exhibit substantially lower activity relative to the wild-type enzyme. Figure 3.3 shows Henri-Michaelis-Menten plots of the kinetic data in which L-P5C is varied and NADH is held constant.

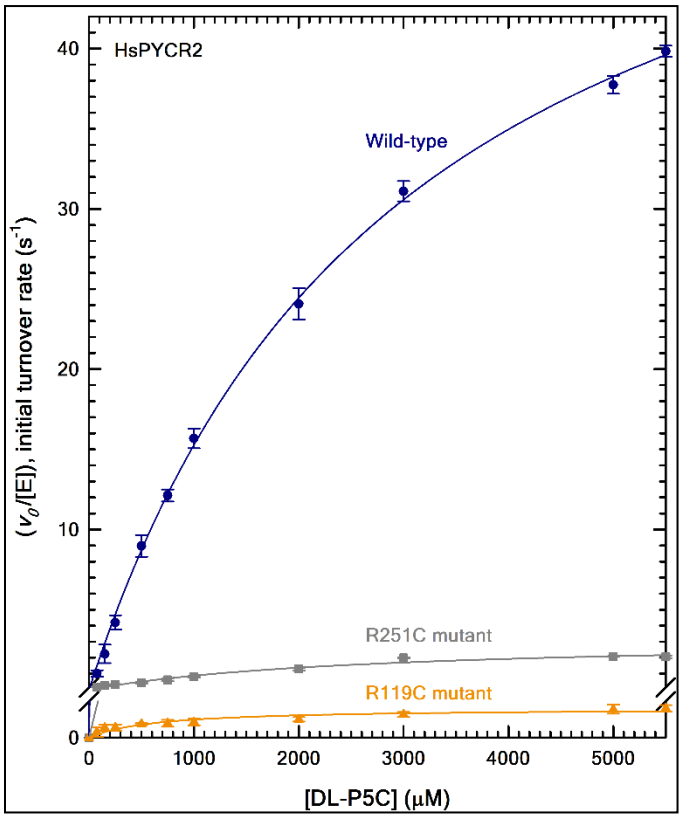

Figure 3.3. Steady-state kinetics of HsPYCR2. Overlay of Henri-Michaelis-Menten kinetics traces of 0.06 μM wild-type HsPYCR2 (dark blue), 0.6 μM R251C mutant (dark gray), and 3 μM R119C mutant (dark orange) enzymes. Assays were performed in 0.1 M Tris-HCl (pH 7.5) reaction buffer at 37 °C with varying DL-P5C (0-5500 μM) concentration and holding NADH fixed at 500 μM. Each data trace is plotted as (mean ± SD) of three technical replicates with non-linear least-squares fit to the Henri-Michaelis-Menten equation using SigmaPlot 12.0.

The $k_{cat}{}^{app}$ values with L-P5C as the varying substrate were 19-fold and 766-fold

lower for R251C and R119C mutants, respectively, than wild-type HsPYCR2. Similarly, significant lower activities were observed with the mutants when NADPH was held fixed. The resulting $k_{cat}{}^{app}/K_M{}^{app}$ values for R251C and R119C were estimated to be 12-fold and 104-fold lower, respectively, than the wild-type enzyme. The apparent k_{cat}/K_M values when varying NADH and holding L-P5C fixed were 26-fold and 366-fold lower than wild-type HsPYCR2 for R251C and R119C mutants, respectively. Thus, the R119C mutation clearly has the most significant impact on HsPYCR2 activity.

This loss of catalytic activity may be explained by inference from the homologous structure of the ternary complex HsPYCR1 + NADPH + L-THFA (PDB code 5UAV),[6] in which the Arg119 site occurs near the posterior wall of the enzyme's active site (Fig. 3.4). Mutation at sites Arg119 or Arg251 may have disrupted the conformation flexibility of the HsPYCR2 structure, perhaps in vicinity of the cofactor substrate binding site, thus leading to decreased kinetics of cofactor substrate entrance and egress.[36] When performing the R119C mutant enzyme activity assays with DL-P5C and NADPH substrates, we encountered an obstacle of limited amounts of R119C mutant enzyme to carry out more technical replicates, yet we still suspect that the drastic loss of catalytic activity is due to this mutation in proximity to the enzyme's active site.

Product(s) Inhibition and Substrate Binding Order

The binding order of L-P5C and NADH to HsPYCR2 was evaluated by product(s) inhibition studies.[37] The inhibition of HsPYCR2 by NAD^+ was first examined by varying NADH and holding DL-P5C constant. Table 3.2 shows that increases in NAD^+ concentration (0-500 μM) results in a decreasing trend in

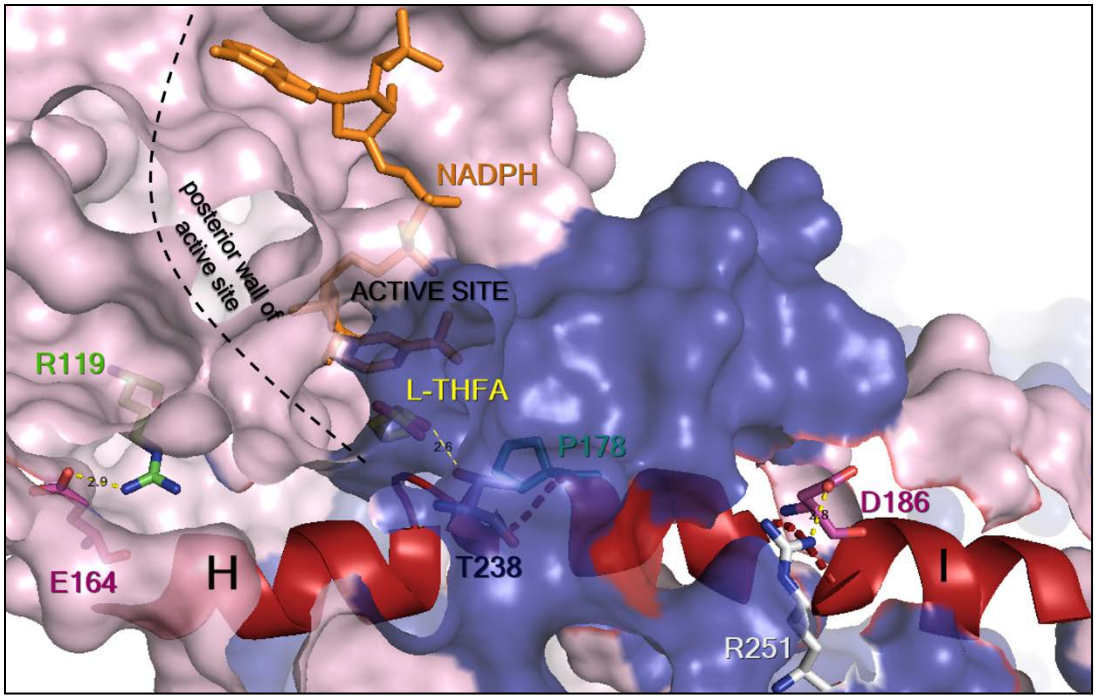

Figure 3.4. Illustration of Arg119 and Arg251 impacting α-helices H and I in PYCR. Diagram was prepared with PyMOL[35], showing a surface rendering with transparency and clipped away perspectives of the dimeric view (light pink and deep blue surfaces are partner monomers) of the experimental X-ray crystal structure of HsPYCR1 + NADPH + L-THFA (PDB code 5UAV).[6] Mutations at conserved sites R119 and R251 (shown as green and light gray stick figures, respectively) in HsPYCR2 enzyme perhaps locally destabilize α-helices H and I (residues Glu164 - Lys194). In reference to the Arg119 site on the posterior wall of the active site containing NADPH and L-THFA (shown as orange and yellow stick figures, respectively, the latter of which is in proximity (2.6 Å) to the deep blue monomer's side chain hydroxyl group of Thr238 active site residue) within the same (light pink) protein monomer, a side-chain guanidinium nitrogen of Arg119 may be hydrogen-bonded within close proximity (2.9 Å) to the side chain carboxyl oxygen of Glu164 (shown as magenta stick figure), which projects from the α-helix H backbone. In reference to the other (deep blue) protein monomer's Arg251 site, its side chain guanidinium nitrogen may be hydrogen-bonded within close proximity (2.8 Å) to the side chain carboxyl oxygen of the same (light pink) protein monomer's Asp186 (shown as magenta stick figure), which projects off of the α-helix I backbone and may be affecting the α-helical H and I kink region's Pro178 site (shown as deep teal stick figure).

$k_{cat}^{\ app}$ and a slightly lower apparent K_M. With increasing NAD^+ concentration, trends of both increasing values of ($1/K_M^{\ app}$) and ($1/V_{lim}$) support the model of mixed inhibition by NAD^+ (Table 3.2 and Figure 3.5, A).[38] Global fitting of the data

Table 3.2. Steady-state kinetic parameters for NAD+ product inhibition of HsPYCR2[a,b,c]

NAD+ (μM)	K_M^{app} (μM)	k_{cat}^{app} (s^{-1})	(k_{cat}^{app}/K_M^{app}) (M^{-1} s^{-1})	K_{IC}^{app} (μM)	K_{IU}^{app} (μM)
0	298 ± 73	47.9 ± 5.3	(161 ± 44) x 10^3	792 ± 248[d]	326 ± 102[d]
100	259 ± 53	37.3 ± 3.2	(144 ± 32) x 10^3		
250	209 ± 31	26.5 ± 1.5	(127 ± 20) x 10^3		
500	211 ± 15	19.1 ± 0.5	(90.5 ± 7.0) x 10^3		

[a]Value ± std error are reported for the apparent best-fit parameters of non-linear least-squares fit to the Henri-Michaelis-Menten equation using SigmaPlot 12.0 (version 12.0.0.182, Systat Software) with data plotted as (mean ± SD) of n=3 technical replicates.
[b]Final enzyme concentration of 0.06 μM in the assays.
[c]DL-P5C concentration was held constant at 5000 μM and NADH concentration was varied from 0-580 μM.
[d]Apparent inhibition constants, K_{IC}^{app} (competitive inhibition) and K_{IU}^{app} (= α (K_{IC}^{app})) (uncompetitive inhibition) were estimated by fitting the data to the Mixed Inhibition (full) model with α = 0.4112 using the Enzyme Kinetics Wizard Add-In on SigmaPlot 12.0 (version 12.0.0.182, Systat Software).

to a mixed inhibition model provided estimates of apparent competitive (K_{IC}) and uncompetitive (K_{IU}) inhibition constants for NAD+ (Figure 3.5, A). L-proline inhibition of HsPYCR2 wild-type was evaluated by varying DL-P5C (0-5500 μM) and holding NADH fixed. Table 3.3 shows that with increasing the L-proline (0-500 μM) the value of K_M^{app} increased whereas V_{lim} remained fairly unchanged consistent with competitive inhibition by L-proline (Table 3.3 and Figure 3.5, C).[38]

Table 3.3. Steady-state kinetic parameters for L-proline product inhibition of HsPYCR2[a,b,c]

L-proline (μM)	K_M^{app} (μM)[d]	k_{cat}^{app} (s^{-1})	(k_{cat}^{app}/K_M^{app}) (M^{-1} s^{-1})	K_{IC}^{app} (μM)
0	1509 ± 69	61.3 ± 1.4	(40.6 ± 2.1) x 10^3	145 ± 8[e]
100	2126 ± 147	52.6 ± 2.0	(24.7 ± 1.9) x 10^3	
250	1627 ± 272	34.5 ± 2.8	(21.2 ± 4.0) x 10^3	
500	3149 ± 590	42.3 ± 4.9	(13.4 ± 3.0) x 10^3	

[a]Value ± std error are reported for the apparent best-fit parameters of non-linear least-squares fit to the Henri-Michaelis-Menten equation using SigmaPlot 12.0 (version 12.0.0.182, Systat Software) with data plotted as (mean ± SD) of n=3 technical replicates.
[b]Final enzyme concentration of 0.06 µM in the assays.
[c]NADH concentration was held constant at 500 µM while DL-P5C concentration was varied 0-5500 µM.
[d]Reported value is the concentration of L-P5C, which is assumed to be half the concentration of the DL-P5C racemic mixture.
[e]Apparent competitive inhibition constant, $K_{IC}{}^{app}$, was estimated by fitting the data to the Competitive Inhibition (full) model using the Enzyme Kinetics Wizard Add-In on SigmaPlot 12.0 (version 12.0.0.182, Systat Software).

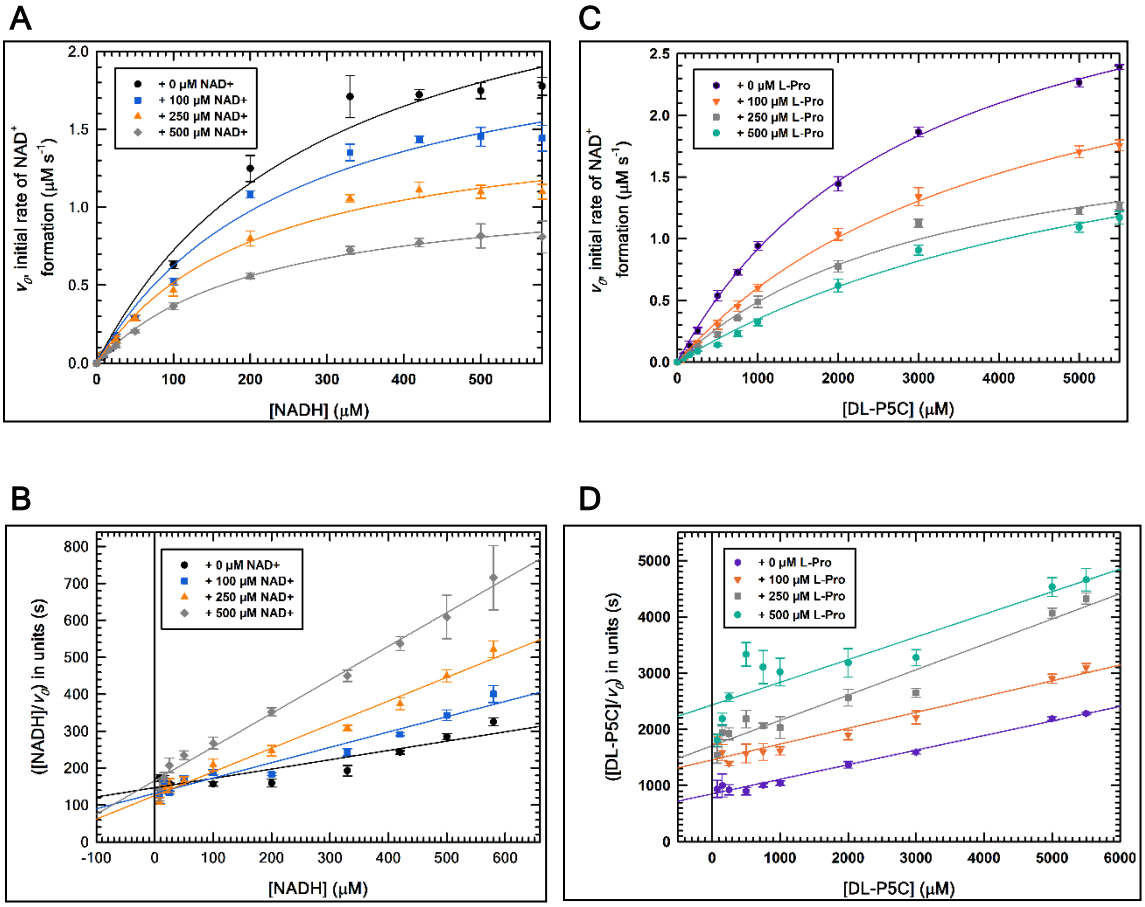

Figure 3.5. Product(s) inhibition kinetics of wild-type HsPYCR2. Henri-Michaelis-Menten plots of assays performed at (A) different NAD⁺ concentrations (0-500 µM) while varying NADH and holding DL-P5C constant (5000 µM) and (C) different L-proline concentrations (0-500 µM) while varying DL-P5C and holding NADH constant (500 µM). Hanes-Woolf plots of the data in panels A and C for inhibition of HsPYCR2 by (B) NAD⁺ and (D) L-proline. Data are plotted as (mean ± SD) of three technical replicates with non-linear least-squares fits to the Henri-Michaelis-Menten equation and linear regression fits to the Hanes-Woolf equation using SigmaPlot 12.0.

Best fits of the data to a competitive inhibition model yielded an apparent K_{IC} value of 145 µM L-proline (Figure 3.5, C). Hanes-Woolf plots of the NAD^+ and L-Pro inhibition data also show linear regressions consistent with mixed and competitive inhibition, respectively (Figure 3.5, B and D). In these plots, linear trends converging at a common negative horizontal axis intercept with an increasing slope ($1/V_{lim}$) effect (Figure 3.5, B) indicates NAD^+ is a mixed noncompetitive inhibitor[39] of HsPYCR2 with respect to NADH. Parallel linear trends with an increasing vertical axis intercept (K_M^{app}/V_{lim}) effect (Figure 3.5, D) indicate L-proline is a competitive inhibitor[39] with respect to L-P5C. Taken together, these modes of inhibition by each product ligand support the proposed sequential-ordered binding mechanism shown in Figure 3.6.[37]

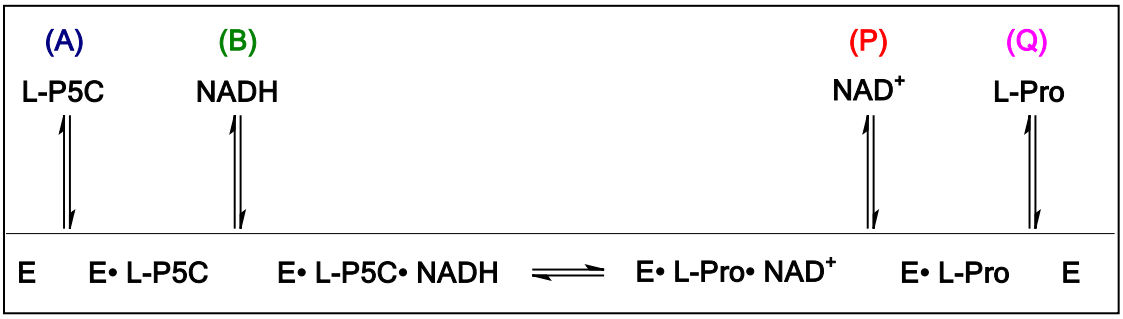

Figure 3.6. Cleland diagram of the proposed sequential-ordered binding mechanism of HsPYCR2. First (A) and second (B) substrates bind in order to HsPYCR2 and, following the chemical step, the first (P) and second (Q) products are released in sequential order.

Because PYCR has been reported to catalyze the reverse reaction with L-proline and NAD^+,[40,41] we thought it would be prudent to test whether HsPYCR2 exhibits reversible activity which would interfere with the above product inhibition assays. No formation of NAD(P)H was observed over 10 min (Fig. 3.7). Thus, HsPYCR2 activity is only detected in the forward direction toward L-proline

production.

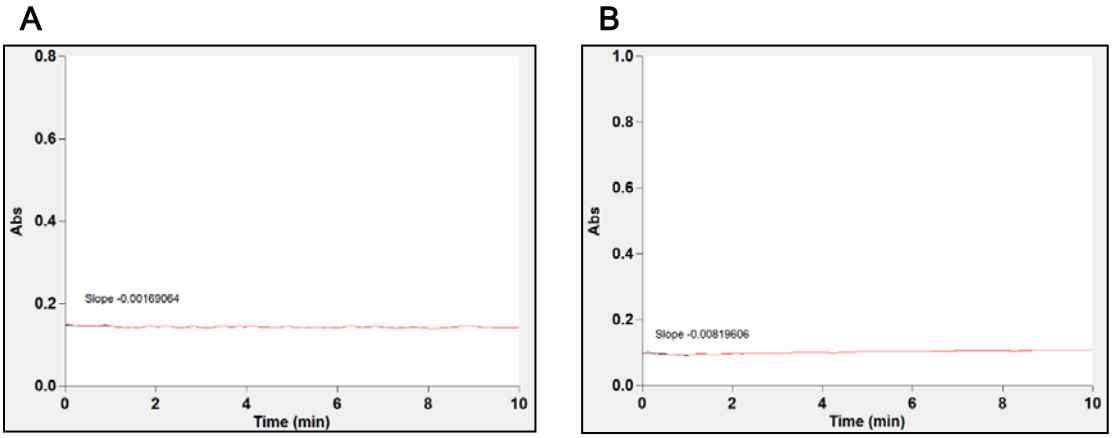

Figure 3.7. Test for HsPYCR2 reverse activity with L-proline. Absorbance traces of HsPYCR2 wild-type enzyme (0.6 µM final concentration) with L-proline (10 mM) and (A) 1 mM NAD^+ or (B) 1 mM $NAD(P)^+$. Assays (600 µL total volume) were performed in 0.1 M Tris-HCl (pH 7.5) containing 0.01% Brij-35 detergent, and 1 mM EDTA at 37 °C and absorbance at 340 nm was monitored for 10 min.

Thermal Stability of HsPYCR2 Wild-type and Mutants

The thermal unfolding of HsPYCR2 proteins was measured in the absence and presence of all combinations of substrates and products to examine HsPYCR2 stability and the functional consequences of the R119C and R251C

Table 3.4 Melting point (T_m) values of HsPYCR2 determined by Thermofluor assays

Ligand(s)[c]	T_m (°C)[a]		
	Wild-type[d]	R251C[d]	R119C[d]
None	69.2 ± 0.1[†]	54.2[b]	67.6 ± 0.1[£]
NADH	69.0 ± 0.1	54.9[b]	66.4 ± 0.1
DL-P5C	69.0 ± 0.1	53.4 ± 0.1	67.2 ± 0.1
NADH + DL-P5C	53.2 ± 0.1[†]	55.4[b]	54.9 ± 0.1[£]
NAD^+	69.6 ± 0.1	53.0 ± 0.2	67.6 ± 0.1
L-Pro	69.4 ± 0.1[§]	52.9 ± 0.1[§‡]	67.6 ± 0.1[‡]
NAD^+ + L-Pro	69.3 ± 0.1[❁]	56.6[b]	67.4 ± 0.1[❁]

[a]Melting point temperatures (T_m) are reported as value ± std error and were determined from the apparent best fit estimates of dynamic curve fits to a user-defined sigmoidal, 4 parameter equation modeled as the Boltzmann equation in SigmaPlot 12.0 (version 12.0.0.182, Systat Software) with data plotted as (mean ± SD) of n=4 technical replicates.
[b]Melting point temperatures reported as the local minimum value from the plot of (-d(RFU)/dT vs. T) using SigmaPlot 12.0 (version 12.0.0.182, Systat Software) with data plotted as (mean ± SD) of n=4 technical replicates.
[c]Each ligand concentration was 1 mM in the assays.
[d]Enzyme concentration was 6.4 µM in all the assays.
[†]According to Student's t-statistic, wild-type (none) and wild-type (NADH + DL-P5C) T_m values are statistically different at 95% confidence level (n=4).
[§]According to Student's t-statistic, wild-type (+ L-Pro) and R251C mutant (+ L-Pro) T_m values are statistically different at 95% confidence level (n=4).
[‡]According to Student's t-statistic, R251C mutant (+ L-Pro) and R119C mutant (+ L-Pro) T_m values are statistically different at 95% confidence level (n=4).
[֍]According to Student's t-statistic, wild-type (NAD^+ + L-Pro) and R119C mutant (NAD^+ + L-Pro) T_m values are statistically different at 95% confidence level (n=4).
[£]According to Student's t-statistic, apo-R119C mutant and R119C mutant (NADH + DL-P5C) T_m values are statistically different at 95% confidence level (n=4).

mutations. HsPYCR2 unfolding was monitored using the Sypro orange reporter dye which increases in fluorescence emission at 610 nm upon binding to surface-exposed hydrophobic-patches as the protein unfolds.[42] The thermal unfolding traces for HsPYCR2 wild-type and mutants are in shown in Figure 3.8 and the corresponding melting point temperatures (T_m) are summarized in Table 3.4. Wild-type HsPYCR2 and the mutant R119C exhibited similar T_m values whereas

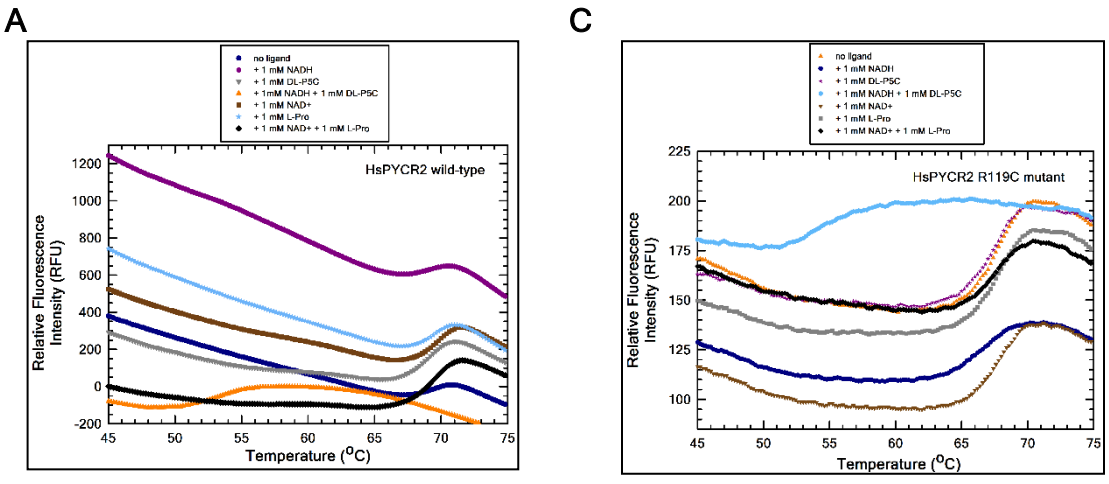

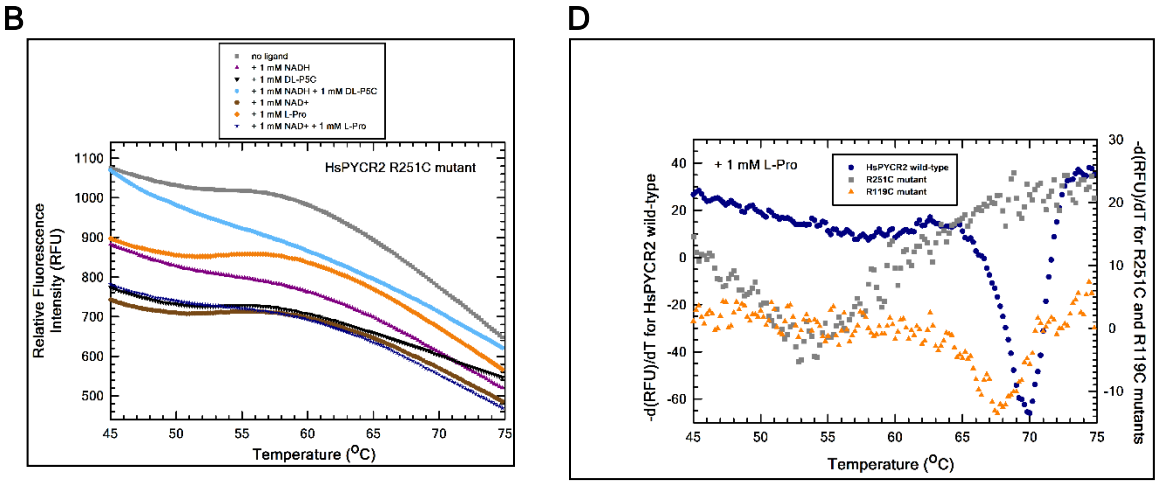

Figure 3.8. Thermal stability assays of HsPYCR2. Relative fluorescence intensity units (RFU) vs. T (°C) from Thermofluor assays are shown for (A) HsPYCR2 wild-type, and mutant enzymes (B) R251C and (C) R119C. The legend indicates the different combinations of substrate and product ligands (1 mM) each trace. (D) A derivative plot of the thermal shift data for HsPYCR2 wild-type (dark blue), R251C mutant (dark grey), and the R119C mutant (dark orange) in the presence of 1 mM L-proline. The local trough minimum indicates the melting point temperature (T_m) for each enzyme. All Thermofluor assays were performed with 6.4 µM enzyme.

the R251C mutant displayed a T_m value (54.2 °C) that was nearly 15 °C lower than the wild-type enzyme (69.2 °C). Unfortunately, some of the unfolding transitions could not be fit to the Boltzmann Equation model used for T_m determinations, particularly for several R251C mutant curves (Fig. 3.8, B).

To verify the lower melting point temperatures of R251C, the data was also visualized as -d(RFU)/dT vs. T plots (Fig. 3.9). Figure 3.8, panel D shows a plot of wild-type HsPCYR2, R251C, and R119C in the presence of L-proline which clearly shows local minimum values of the troughs confirming significantly left-shifted T_m values for the R251C mutant (ranging 53-56 °C) indicating lower thermostability relative to HsPYCR2 wild-type ($T_m \approx 69$ °C) and the R119C mutant ($T_m \approx 67$ °C).

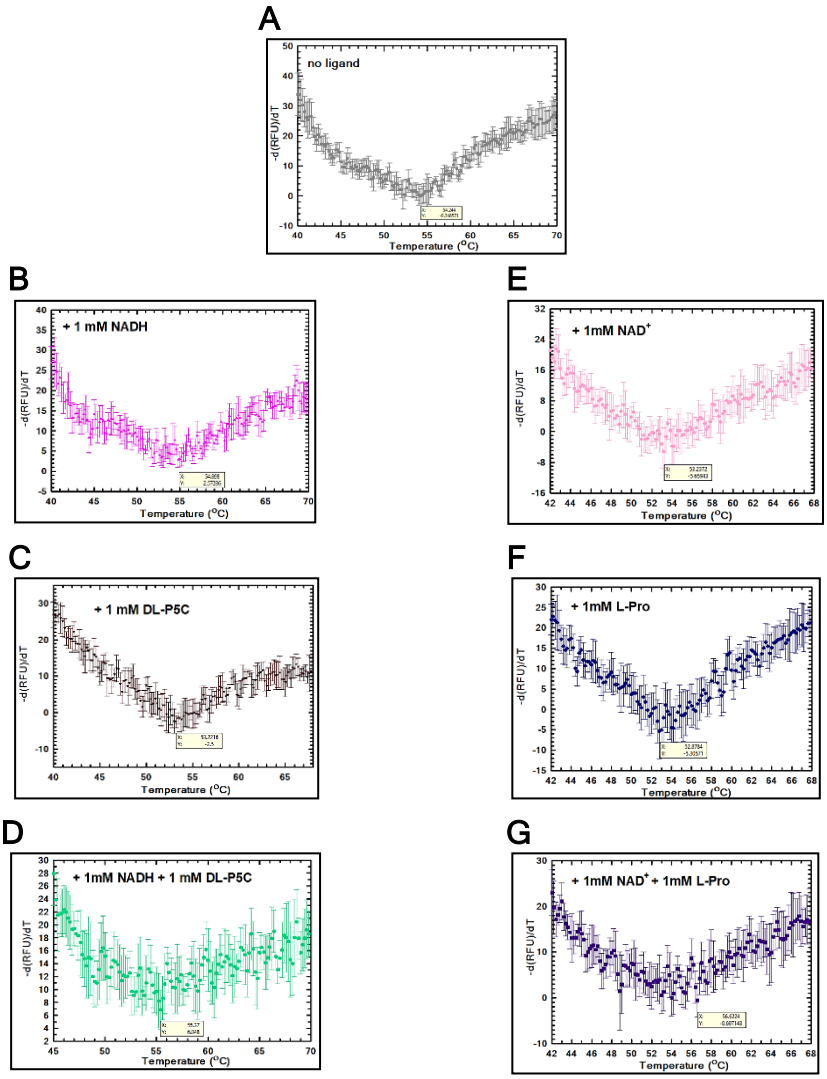

Figure 3.9. Fluorescence-based protein thermal shift profiles of R251C mutant enzyme with no ligand or combinations of substrate ligands or product ligands. Thermofluor assay traces of (-d(RFU)/dT) vs. T (°C) for 6.4 µM R251C mutant enzyme with (A) no ligand, (B) 1 mM NADH, (C) 1 mM DL-P5C, (D) 1 mM NADH + 1 mM DL-P5C, (E) 1 mM NAD^+, (F) 1 mM L-Pro, and (G) 1 mM NAD^+ + 1 mM L-Pro. Local minima of the troughs in the plots represent melting point (T_m) determinations. The trough minima of the traces are annotated.

Adding substrates individually had no effect on the thermal stability of the HsPYCR2 enzymes, however, the combination of NADH and DL-P5C induced significantly lower (95% confidence level, n=4) T_m values for the wild-type enzyme (53.2 °C) and the R119C mutant (54.9 °C). Incubation of the HsPYCR2

enzymes with products had no effect on the observed T_m values. Because the observed effect on T_m is only observed when both substrates (NADH + DL-P5C) are present, the ternary complex of HsPYCR2-P5C-NADH may induce a conformational change during catalytic turnover that is less stable than the enzyme alone.

Secondary Structure of HsPYCR2 Wild-type and Mutants

The CD spectra of HsPYCR2 wild-type and mutants are shown in Figure 3.10. The CD spectrum of the R119C mutant was typical of a protein with strong α-helical character whereas the spectrum of wild-type HsPYCR indicates less α-helical character. Most notably, the R251C mutant displays the lowest amount of α-helical character of the HsPYCR2 proteins.

To provide more insight into the observed differences in the CD spectra, secondary structure analysis was performed using the β-structure selection (BeStSel) method that takes into account the twist of β-structures.[33] BeStSel accommodates for the spectral diversity of β-structures which is sometimes a drawback of CD spectroscopy, and was recently shown to outperform 11 other secondary structure estimation algorithms.[33] Figure 3.10, panels B-D show secondary structural analysis of HsPYCR2 wild-type, and the mutants R251C

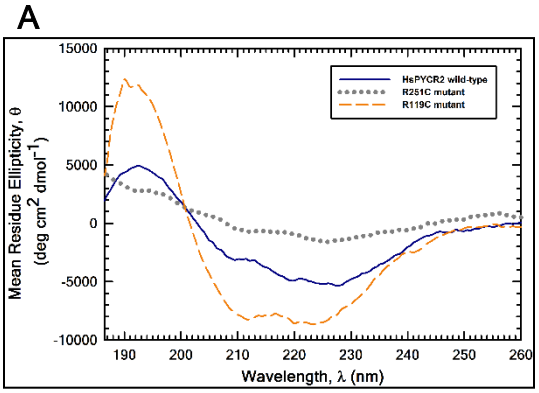

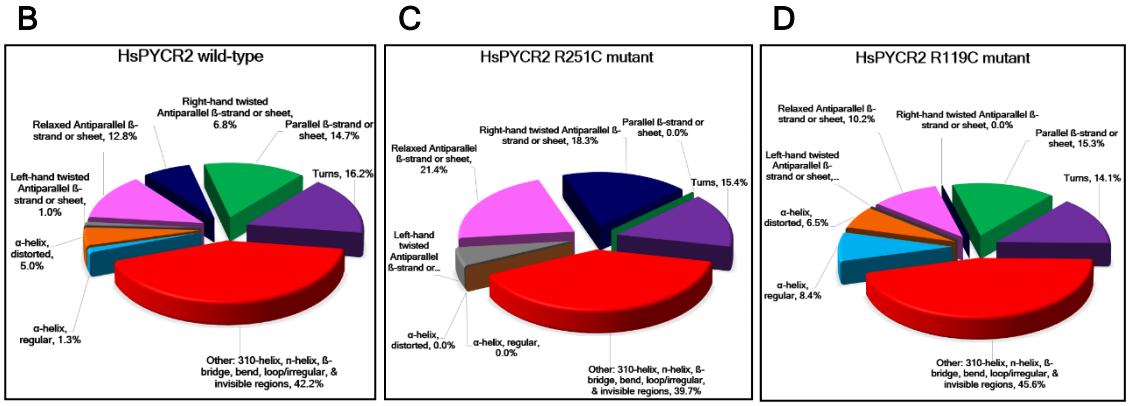

Figure 3.10. Secondary structure analysis of HsPYCR2 wild-type and mutant enzymes. (A) CD spectra of HsPYCR2 wild-type (dark blue), and the mutants R251C (dark grey) and R119C (dark orange) (4 µM each). Secondary structure analysis of (B) HsPYCR2 wild-type, and the mutants (C) R251C and (D) R119C. The experimental CD spectrum of each protein was fit with the BeStSel algorithm[33] and analyzed for eight secondary structure components: α-helix, regular; α-helix, distorted; left-hand twisted antiparallel β-strand or sheet; relaxed antiparallel β-strand or sheet; right-hand twisted antiparallel β-strand or sheet; parallel β-strand or sheet; turns; and other (3_{10}-helix, π-helix, β-bridge, bend, loop/irregular, and other invisible regions). The different secondary structure component contributions to the CD spectrum of each protein are expressed as a normalized percent.

and R119C, respectively. The overlay traces of the BeStSel algorithm fits to the experimental CD spectra (190-250 nm) of HsPYCR2 wild-type, R251C, and R119C shown in Fig. 3.11 exhibited high calculated values of Pearson correlation coefficients[43] of 0.9928, 0.9975, and 0.9790, respectively, suggesting a strong reliability of the secondary structure estimations for each protein (Table 3.5).

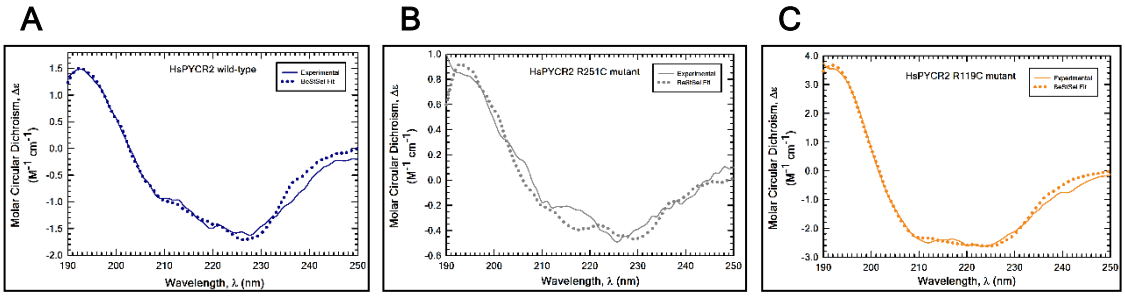

Figure 3.11. BeStSel algorithm fits to experimental CD spectra of HsPYRC2 proteins. Shown is the overlay of the experimental CD spectra (solid line) and the best-fit CD spectra (dotted line) generated by the BeStSel algorithm.[33] Data are plotted as Molar Circular Dichroism (Δε) in units M^{-1} cm^{-1} versus wavelength for (A) HsPYCR2 wild-type, (B) R251C mutant, and (C) R119C mutant enzymes.

The BeStSel structural explanations for the observed CD spectra indicate that the R119C mutant has an overall α-helical character ($f_{\alpha R}$ + $f_{\alpha D}$) that is over 2-fold (14.9 %) higher than HsPYCR2 wild-type (6.3 %) (Figure 3.10, B and D and Table 3.5). The R251C mutant is estimated to have substantially lower α-helical character than HsPYCR2 wild-type but has 2-fold (44.9%) higher antiparallel β-strand character ($f_{\beta Anti1}$ + $f_{\beta Anti2}$ + $f_{\beta Anti3}$) than the wild-type enzyme (20.6 %) (Figure 3.10, B and C and Table 3.5) .

DISCUSSION

In this work, functional and structural characterization of HsPYCR2 mutants R119C and R251C was provided to gain insight into how these mutations may contribute to hypomyelinating leukodystrophy type 10, an autosomal recessive neurological disorder. Different clinical studies have found that patients with inborn genetic errors in the *PYCR2* gene initially possess normal growth parameters and brain anatomy at birth, but then progressively develop microcephaly, hypomyelination, and failure to thrive complications that lead to cognitive and motor deficits that eventually terminate their lives in childhood.[34,44] Zaki et al.'s (2016) study of 14 affected individuals ascertained that the patients harbored either a stop codon mutation that results in depletion of PYCR2 or one of five missense mutations in the dimerization domain, such as Arg199Trp and Cys232Gly.[18] Expression levels of missense PYCR2 mutants were not found to be significantly decreased relative to wild-type PYCR2, however, based on coimmunoprecipitation experiments of PYCR2 in 293T cells, the authors reported on impaired protein multimerization of the patient protein variants,[18] indicating the mutant proteins may not form a proper oligomeric structure, which for human

Table 3.5. Secondary structure analysis[a] of HsPYCR2 proteins from Circular Dichroism Spectra

		Performance Indices			Secondary structure fractions							
Protein	N_{res}	$RMSD_{CD}$[b]	$NRMSD_{CD}$[c]	Pearson Correlation Coefficient[d], r_{CD}	α-helix, regular ($f_{\alpha R}$)	α-helix , distorted ($f_{\alpha D}$)	Left-hand twisted Antiparallel β-strand or sheet ($f_{\beta Anti1}$)	Relaxed Antiparallel β-strand or sheet ($f_{\beta Anti2}$)	Right-hand twisted Antiparallel β-strand or sheet ($f_{\beta Anti3}$)	Parallel β-strand or sheet ($f_{\beta Para}$)	Turns (f_T)	Other: 3_{10}-helix, π-helix, β-bridge, bend, loop/irregular, & other invisible regions (f_{Other})
Wild-type	340	0.1216	0.03925	0.9928	0.013	0.050	0.010	0.128	0.068	0.147	0.162	0.422
R119C Mutant	340	0.1447	0.02269	0.9975	0.084	0.065	0.000	0.102	0.000	0.153	0.141	0.456
R251C Mutant	340	0.0936	0.06282	0.9790	0.000	0.000	0.052	0.214	0.183	0.000	0.154	0.397

[a]Fractions of secondary structure elements determined from fitted circular dichroism spectra (190-250 nm) analyzed by BeStSel algorithm.[33]

[b]According to Micsonai et al.,[33] the root mean square deviation of CD spectral data was calculated as

$$RMSD_{CD} = \sqrt{\left(\frac{1}{w}\right) \times \left(\sum_{i=1}^{w}(CD_{exp,i} - CD_{fit,i})^2\right)}\ .$$

[c]Based on a modified definition reported by Micsonai et al.[33] and verified by the corresponding author (Jozsef Kardos, personal communication), normalized root mean square deviation of CD spectral data was calculated as

$$NRMSD_{CD} = \frac{[RMSD_{CD}]}{(max(CD_{exp}) - min(CD_{exp}))} = \frac{\left[\sqrt{\left(\frac{1}{w}\right) \times \left(\sum_{i=1}^{w}(CD_{exp,i} - CD_{fit,i})^2\right)}\right]}{(max(CD_{exp}) - min(CD_{exp}))}\ .$$

[d]According to Sreerama et al.,[43] Pearson correlation coefficient of CD spectral data was calculated as

$$r_{CD} = \frac{w\left(\sum_{i=1}^{w} CD_{exp,i} \times CD_{fit,i}\right) - \left(\sum_{i,j=1}^{w} CD_{exp,i} \times CD_{fit,j}\right)}{\sqrt{\left[w\left(\sum_{i=1}^{w} CD_{exp,i}\right)^2 - \left(\sum_{i=1}^{w} CD_{exp,i}\right)^2\right] \times \left[w\left(\sum_{j=1}^{w} CD_{fit,j}\right)^2 - \left(\sum_{j=1}^{w} CD_{fit,j}\right)^2\right]}}\ .$$

PYCR1 is a pentamer-of-dimers.[6]

More recently, Escande-Beillard et al. (2020) developed a Pycr2$^{-/-}$ mouse model, in which both PYCR2 and incidentally PYCR1 protein expression was limited, indicating that the loss of PYCR2 was not compensated by the engagement of PYCR1 activity to counteract the pathogenesis of recessive hypomyelinating leukodystrophy type 10.[44] Upon performing liquid chromatography-tandem mass spectrometry of Pycr2$^{-/-}$ mouse brain tissue samples, analysis of several amino acids that behave as neurotransmitters was unremarkable except for substantially and significantly high levels of glycine, an excitatory neurotransmitter, in all tested brain regions. Based on marked neuronal and oligodendroglial morphological changes indicative of axonopathy, hypomyelination, and premature apoptosis found in both brain MRI scans of HLD10 patients and immunofluorescence analysis of Pycr2$^{-/-}$ mouse brain tissues, the authors remarked that PYCR2 deficient patients and mice showed signs of cerebral hyperglycinemia with encephalopathy.[44] Using proximity-based BirA-protein label proteomics on primary human cell lines, serine hydroxymethyltransferase (SHMT2), the rate-limiting mitochondrial enzyme responsible for glycine synthesis, was not only found among the top five PYCR protein-protein interaction candidates, but endogenous protein expression (as well as mRNA levels in mice) of SHMT2 were significantly upregulated in the absence of PYCR2.[44] Further immunofluorescence staining and quantitative analyses demonstrated that knockdown of SHMT2 could rescue both axonal beading and reduced neurite length (phenotypes of axonal injury) of cultured Pycr2$^{-/-}$ mouse neurons.[44]

Here we show two missense mutations (R251C and R119C) in the *PYCR2* gene that are linked to HLD10 marked by axonal injury and microcephaly, impair HsPYCR2 catalytic activity. The observed loss in activity results from different underlying causes in the two mutants. Currently X-ray crystal structures of HsPYCR2 are not available. However, Arg119 and Arg251 are conserved in HsPYCR1, thus allowing their structural contributions to be examined. The structure of HsPYCR1 in complex with NADPH and L-THFA (PDB code 5UAV) is shown in Figure 3.4.[6] Arg119 (green sticks) and Arg251 (light gray sticks) are from different protomers but interact with Glu and Asp residues of one protomer on α-helices H and I, which are split by a kink formed by Pro178. The active site is formed at the dimer interface with Thr238 of one protomer (see chapter two, Fig. 2.6) forming a key hydrogen bonding interaction with the ring oxygen of L-THFA, which is synonymous with the imine nitrogen of L-P5C or L-Pro. Arg119 resides on a β-strand of the Rao-Rossmann fold with its side chain guanidinium group within 2.9 Å to the side chain carboxylate groups of Glu164 of α-helix H of the same protomer. Thereby, Arg119 likely helps stabilize α-helix H which has a critical role in shaping the active site.[6] The loss of enzyme activity in the R119C mutant of HsPYCR2 is likely related to disrupting the active site environment. Why the R119C would exhibit enhanced α-helical character as observed by CD spectroscopy is not clear from the structure of HsPYCR1.

As shown in Figure 3.4, the partner protomer's (deep blue) Arg251 site has its side chain guanidinium nitrogen within close proximity (2.8 Å) for a hydrogen bond with the side chain carboxyl oxygen of the other protomer's (light pink) Asp186 of α-helix I. Thus, Arg251 contributes to interactions at the dimerization

interface between the two protomers. The dramatic decrease in thermal stability and α-helical content of the R251C mutant relative to wild-type HsPYCR2 indicates that Arg251 has an important structural role. The loss of the Arg251-Asp186 interaction in the R251C mutant may destabilize α-helices L and K, thereby changing the orientation of Thr238 and negatively impacting the active site. Escande-Beillard et al. (2020) rationalized that substitution of residue Glu246 into Val with a bulkier side chain most likely results in steric hindrance with the partner monomer at the dimer interface of human PYCR2, thus disrupting catalytic function as observed with the Glu246Val mutant enzyme.[44] With respect to the T_m values determined here for HsPYCR2, the values are higher than typically observed for human proteins. In a survey of 18 human proteins within the enzyme classes of sulfotransferases, methyltransferases, and isomerases, Vedadi et al. (2006) reported melting point temperatures ranging from 34-58 °C using differential scanning fluorimetry.[45] The T_m values estimated for HsPYCR2 wild-type and R119C mutant are above that conventionally expected for human enzymes, however, the observed T_m for HsPYCR2 wild-type alone (69 °C) is consistent with a previously reported thermal inactivation of HsPYCR1 in which the enzyme activity dropped to 50% within 10 min at 68 °C.[5]

Product(s) inhibition kinetics studies revealed L-Pro behaving as a competitive inhibitor and NAD^+ behaving as a mixed inhibitor against wild-type HsPYCR2 enzyme, which is diagnostic of a sequential binding order with L-P5C binding first to the enzyme followed by NADH (Fig. 3.6). This binding order is atypical of the general family of dehydrogenase enzymes, i.e. lactate dehydrogenase, which first binds NAD^+/NADH before the second substrate.[46]

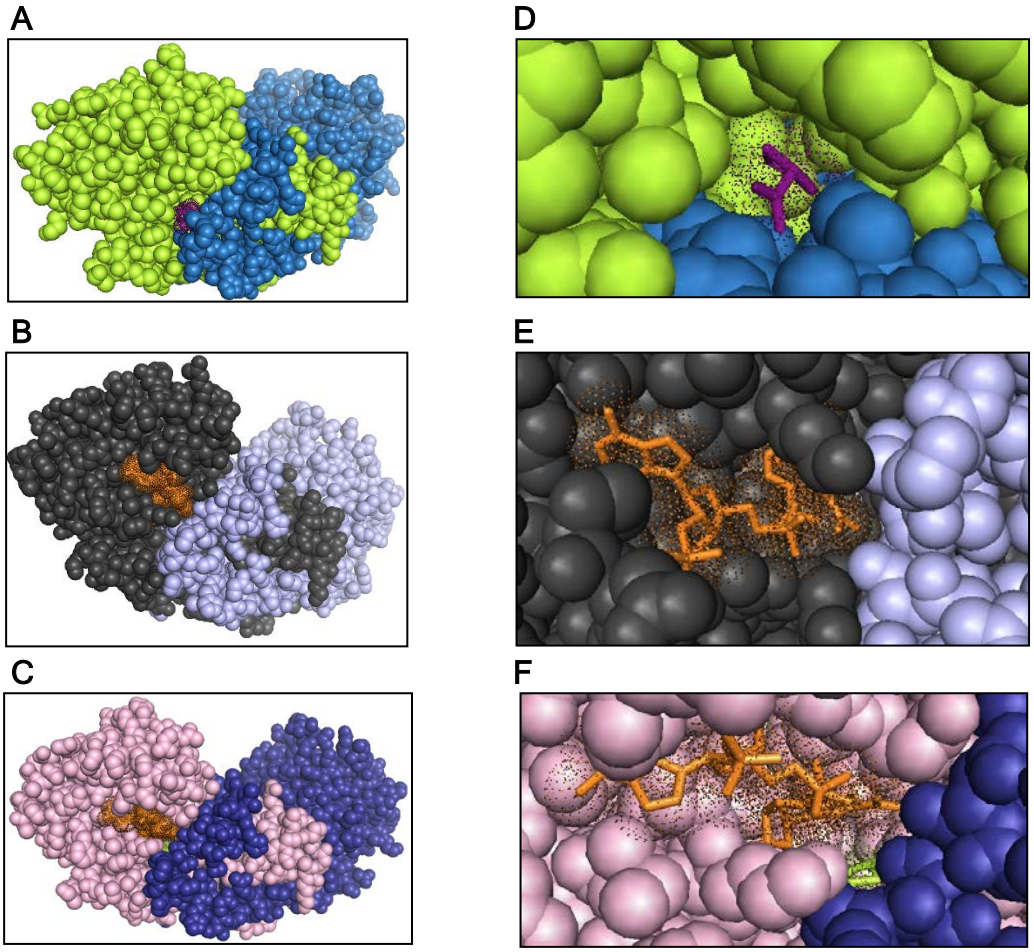

Figure 3.12. Single dimer ball-space-filling model views of enzyme-ligand(s) complexes. Illustrations were prepared with PyMOL[35] as renderings of homologous HsPYCR1 experimental X-ray crystal structure that support our proposed sequential-binding order mechanism of HsPYCR2. (A and D) 1.92 Å structure of HsPYCR1 + L-Pro (PDB code 5UAT)[6] as lime green and sea blue partner monomers shown with buried L-Pro product ligand (purple sticks and dots) in a single active site zoomed in on right panel B, (B and E) 1.90 Å structure of HsPYCR1 + NADPH (PDB code 5UAU)[6] as black and light blue partner monomers shown with bound NADPH substrate ligand (orange sticks and dots) in a single active site zoomed in on right panel D, and (C and F) 1.85 Å structure of HsPYCR1 + NADPH + L-THFA (PDF code 5UAV)[6] as salmon pink and dark blue partner monomers shown with buried L-THFA analog ligand (yellow sticks and dots) together with bound NADPH substrate ligand (orange sticks and dots) in a single active site zoomed in on right panel F.

The proposed binding order is supported by X-ray crystal structures of HsPYCR1 in complex with THFA and NADPH (Fig. 3.12), which shows that L-THFA, which is an analog of both L-proline and L-P5C, is buried within the active site. The

binding site for L-THFA would be obstructed if NADPH were to bind first, thus supporting the sequential binding order of the smaller L-P5C molecule followed by binding of the larger NAD(P)H molecule. Specifically, Figure 3.12, panels C and F show that NADPH is more solvent exposed which would facilitate the sequential release of $NADP^+$ followed by L-proline. These findings are consistent with previous studies in which bacterial (*S. pyogenes*) and plant (*A. thaliana*) P5CRs were also proposed to follow a sequential-ordered binding mechanism with L-P5C binding prior to NAD(P)H.[27,47] Having the sequential-ordered binding mechanism of HsPYCR2 established will help guide development of new inhibitors and/or substrate analogs as molecular probes for modulating HsPYCR2 activity.

Interestingly, serum levels of L-proline in healthy adult humans are reported to range from 125-633 μM with mean levels around 270 μM.[48,49] The competitive inhibition constant determined here for L-proline (K_{IC}^{app}= 145 ± 8 μM) as well as that previously reported for HsPYCR2 by De Ingeniis et al. (K_I = 96 μM)[2], is within physiological L-proline concentrations suggesting that HsPYCR2 is susceptible to product feedback inhibition by L-proline. Because concentrations of normal human fasting plasma L-P5C and of L-P5C released into extracellular medium by cultured human skin fibroblasts have been observed << 100 μM[50,51] and the apparent K_M determined here for L-P5C is (1509 ± 69 μM), HsPYCR2 is likely operating under V/K_M^{app} conditions and thereby sensitive to feedback regulation by L-proline.

On a more clinical note, previous studies which have profiled blood and plasma metabolites of HsPYCR2-deficient patients have reported no significant

decreases in L-proline .[17,18] However, it remains unknown what the concentrations of L-proline are in the relevant affected neurological tissue and cerebrospinal fluid (CSF) of these patients. In Escande-Beillard et al. (2020)'s study, the authors mentioned that no L-proline deficiency in blood or brain tissues was found in Pycr2$^{-/-}$ mice.[44] Yet, progressive neurological deterioration associated with another enzyme (P5CS) deficiency is marked by hypoprolinemia and lower urea cycle intermediates (e.g., ornithine, citrulline, arginine) that cannot be treated by fortified amino acid supplements.[52,53] Unsuccessful supplementation therapies may be due to a number of complications such as low bioavailability, high clearance rates, different intestinal absorption and plasma kinetics between amino acids derived from amino acid supplements and whole protein, as well as inadequate delivery to affected tissues.[54] Thus, L-proline serum levels in HsPYCR2 deficient patients may not be an adequate biochemical marker to determine whether HsPYCR2 deficiency causes abnormal L-proline bioavailability in patients, especially in the CSF. On a broader scope, Escande-Beillard et al. (2020) proposed loss of PYCR2 may lead to SHMT2 upregulation as the direct cause of cerebral hyperglycinemia in HLD10 patients, which triggers excitotoxicity by activation of N-methyl-D-aspartate (NMDA) receptors leading to hypomyelination and axonal damage; thus, perhaps therapeutic NMDA receptor antagonists or other treatments aimed at lowering cerebral glycine levels might be of benefit to PYCR2-deficient patients.[44]

In conclusion, we have shown that HsPYCR2 mutants R119C and R251C result in impaired enzyme function and structural stability, thus potentially leading to disrupted L-proline biosynthesis and metabolic dysfunctions that contribute to

hypomyelinating leukodystrophy type 10 with microcephaly.

REFERENCES

[1] Forlani, G., Makarova, K. S., Ruszkowski, M., Bertazzini, M., and Nocek, B. (2015) Evolution of plant δ(1)-pyrroline-5-carboxylate reductases from phylogenetic and structural perspectives, *Front Plant Sci 6*, 567.

[2] De Ingeniis, J., Ratnikov, B., Richardson, A. D., Scott, D. A., Aza-Blanc, P., De, S. K., Kazanov, M., Pellecchia, M., Ronai, Z. e., Osterman, A. L., and Smith, J. W. (2012) Functional Specialization in Proline Biosynthesis of Melanoma, *PLoS ONE 7*, e45190 EP -.

[3] Madeira, F., Park, Y. M., Lee, J., Buso, N., Gur, T., Madhusoodanan, N., Basutkar, P., Tivey, A. R. N., Potter, S. C., Finn, R. D., and Lopez, R. (2019) The EMBL-EBI search and sequence analysis tools APIs in 2019, *Nucleic Acids Res 47*, W636-W641.

[4] Berman, H. M., Westbrook, J., Feng, Z., Gilliland, G., Bhat, T. N., Weissig, H., Shindyalov, I. N., and Bourne, P. E. (2000) The Protein Data Bank, *Nucleic Acids Res 28*, 235-242.

[5] Meng, Z., Lou, Z., Liu, Z., Li, M., Zhao, X., Bartlam, M., and Rao, Z. (2006) Crystal Structure of Human Pyrroline-5-carboxylate Reductase, *Journal of Molecular Biology 359*, 1364-1377.

[6] Christensen, E. M., Patel, S. M., Korasick, D. A., Campbell, A. C., Krause, K. L., Becker, D. F., and Tanner, J. J. (2017) Resolving the cofactor-binding site in the proline biosynthetic enzyme human pyrroline-5-carboxylate reductase 1, *Journal of Biological Chemistry 292*, 7233-7243.

[7] Rao, S. T., and Rossmann, M. G. (1973) Comparison of super-secondary structures in proteins, *J Mol Biol 76*, 241-256.

[8] Ruszkowski, M., Nocek, B., Forlani, G., and Dauter, Z. (2015) The structure of Medicago truncatula δ(1)-pyrroline-5-carboxylate reductase provides new insights into regulation of proline biosynthesis in plants, *Front Plant Sci 6*, 869.

[9] Liu, W., Hancock, C. N., Fischer, J. W., Harman, M., and Phang, J. M. (2015) Proline biosynthesis augments tumor cell growth and aerobic glycolysis: involvement of pyridine nucleotides, *Sci Rep 5*, 17206.

[10] Phang, J. M. (2019) Proline Metabolism in Cell Regulation and Cancer Biology: Recent Advances and Hypotheses, *Antioxid Redox Signal 30*, 635-649.

[11] Sun, C., Li, T., Song, X., Huang, L., Zang, Q., Xu, J., Bi, N., Jiao, G., Hao, Y., Chen, Y., Zhang, R., Luo, Z., Li, X., Wang, L., Wang, Z., Song, Y., He, J., and Abliz, Z. (2019) Spatially resolved metabolomics to discover tumor-associated metabolic alterations, *Proc Natl Acad Sci U S A 116*, 52-57.

[12] Choi, U. Y., Lee, J. J., Park, A., Zhu, W., Lee, H. R., Choi, Y. J., Yoo, J. S., Yu, C., Feng, P., Gao, S. J., Chen, S., Eoh, H., and Jung, J. U. (2020) Oncogenic human herpesvirus hijacks proline metabolism for tumorigenesis, *Proc Natl Acad Sci U S A*.

[13] Keeratichamroen, S., Subhasitanont, P., Chokchaichamnankit, D., Weeraphan, C., Saharat, K., Sritana, N., Kantathavorn, N., Wiriyaukaradecha, K., Sricharunrat, T., and Paricharttanakul, N. M. Identification of potential cervical cancer serum biomarkers in Thai patients, *Oncology Letters*.

[14] Ou, R., Zhang, X., Cai, J., Shao, X., Lv, M., Qiu, W., Xuan, X., Liu, J., Li, Z., and Xu, Y. (2016) Downregulation of pyrroline-5-carboxylate reductase-2 induces the autophagy of melanoma cells via AMPK/mTOR pathway, *Tumour Biol 37*, 6485-6491.

[15] Kniffin, C. L., and O'Neill, M. J. F. Online Mendelian Inheritance in Man, OMIM. CUTIS LAXA, AUTOSOMAL RECESSIVE, TYPE IIB; ARCL2B. MIM Number: 612940: 06/15/2018., Johns Hopkins University, Baltimore, MD. Online <https://omim.org/entry/612940>.

[16] Kniffin, C. L. Online Mendelian Inheritance in Man, OMIM. LEUKODYSTROPHY, HYPOMYELINATING, 10; HLD10. MIM Number: 616420: 10 /27/2016., John Hopkins University., Baltimore, MD. Online <https://omim.org/entry/616420>.

[17] Nakayama, T., Al-Maawali, A., El-Quessny, M., Rajab, A., Khalil, S., Stoler, Joan M., Tan, W.-H., Nasir, R., Schmitz-Abe, K., Hill, R. S., Partlow, Jennifer N., Al-Saffar, M., Servattalab, S., LaCoursiere, Christopher M., Tambunan, Dimira E., Coulter, Michael E., Elhosary, Princess C., Gorski, G., Barkovich, A. J., Markianos, K., Poduri, A., and Mochida, Ganeshwaran H. (2015) Mutations in PYCR2, Encoding Pyrroline-5-Carboxylate Reductase 2, Cause Microcephaly and Hypomyelination, *The American Journal of Human Genetics 96*, 709-719.

[18] Zaki, M. S., Bhat, G., Sultan, T., Issa, M., Jung, H. J., Dikoglu, E., Selim, L., G. Mahmoud, I., Abdel-Hamid, M. S., and Abdel-Salam, G. (2016) PYCR2 mutations cause a lethal syndrome of microcephaly and failure to thrive, *Annals of neurology 80*, 59-70.

[19] Guo, L., Cui, C., Zhang, K., Wang, J., Wang, Y., Lu, Y., Chen, K., Yuan, J., Xiao, G., Tang, B., Sun, Y., and Wu, C. (2019) Kindlin-2 links mechano-environment to proline synthesis and tumor growth, *Nat Commun 10*, 845.

[20] Gao, Q., Zhu, H., Dong, L., Shi, W., Chen, R., Song, Z., Huang, C., Li, J., Dong, X., Zhou, Y., Liu, Q., Ma, L., Wang, X., Zhou, J., Liu, Y., Boja, E., Robles, A. I., Ma, W., Wang, P., Li, Y., Ding, L., Wen, B., Zhang, B., Rodriguez, H., Gao, D., Zhou, H., and Fan, J. (2019) Integrated Proteogenomic Characterization of HBV-Related Hepatocellular Carcinoma, *Cell 179*, 1240.

[21] Wang, Q. L., and Liu, L. (2019) PYCR1 is Associated with Papillary Renal Cell Carcinoma Progression, *Open Med (Wars) 14*, 586-592.

[22] Williams, I., and Frank, L. (1975) Improved chemical synthesis and enzymatic assay of delta-1-pyrroline-5-carboxylic acid, *Anal Biochem 64*, 85-97.

[23] Mezl, V. A., and Knox, W. E. (1976) Properties and analysis of a stable derivative of pyrroline-5-carboxylic acid for use in metabolic studies, *Anal Biochem 74*, 430-440.

[24] Sambrook, J., Fritsch, E. F., and Maniatis, T. (1989) *Molecular cloning: a laboratory manual*, Cold spring harbor laboratory press.

[25] de Marco, A., Deuerling, E., Mogk, A., Tomoyasu, T., and Bukau, B. (2007) Chaperone-based procedure to increase yields of soluble recombinant proteins produced in E. coli, *BMC Biotechnol 7*, 32.

[26] Merrill, M. J., Yeh, G. C., and Phang, J. M. (1989) Purified human erythrocyte pyrroline-5-carboxylate reductase. Preferential oxidation of NADPH, *Journal of Biological Chemistry 264*, 9352-9358.

[27] Nocek, B., Chang, C., Li, H., Lezondra, L., Holzle, D., Collart, F., and Joachimiak, A. (2005) Crystal structures of delta1-pyrroline-5-carboxylate reductase from human pathogens Neisseria meningitides and Streptococcus pyogenes, *J Mol Biol 354*, 91-106.

[28] Szoke, A., Miao, G. H., Hong, Z., and Verma, D. P. (1992) Subcellular location of delta-pyrroline-5-carboxylate reductase in root/nodule and leaf of soybean, *Plant Physiol 99*, 1642-1649.

[29] Deutch, C. E., Klarstrom, J. L., Link, C. L., and Ricciardi, D. L. (2001) Oxidation of l-Thiazolidine-4-Carboxylate by Δ1-Pyrroline-5-Carboxylate Reductase in Escherichia coli, *Current Microbiology 42*, 442-446 LA - English.

[30] Beer. (1852) Bestimmung der Absorption des rothen Lichts in farbigen Flüssigkeiten, *Annalen der Physik 162*, 78-88.

[31] Lambert, J. H., and Klett, E. (1760) *Photometria sive de mensura et gradibus luminis, colorum et umbrae*, Klett.

[32] Bouguer, P. (1729) *Essai d'optique sur la gradation de la lumière*, chez Claude Jombert, ruë S. Jacques, au coin de la ruë des Mathurins, à l ….

[33] Micsonai, A., Wien, F., Kernya, L., Lee, Y. H., Goto, Y., Réfrégiers, M., and Kardos, J. (2015) Accurate secondary structure prediction and fold recognition for circular dichroism spectroscopy, *Proc Natl Acad Sci U S A 112*, E3095-3103.

[34] Meng, L., Donti, T., Xia, F., Niu, Z., Al Shamsi, A., Hertecant, J., Al-Jasmi, F., Gibson, J. B., Nagakura, H., Zhang, J., He, W., Eng, C., Yang, Y., and Elsea, S. H. (2017) Homozygous variants in pyrroline-5-carboxylate reductase 2 (PYCR2) in patients with progressive microcephaly and hypomyelinating leukodystrophy, *Am J Med Genet A 173*, 460-470.

[35] DeLano, W. L. (2015) The PyMOL Molecular Graphics System, version 1.8 ed., Schrodinger, LLC, New York.

[36] Sang, P., Hu, W., Ye, Y.-J., Li, L.-H., Zhang, C., Xie, Y.-H., and Meng, Z.-H. (2017) In silico screening, molecular docking, and molecular dynamics studies of SNP-derived human P5CR mutants, *Journal of Biomolecular Structure and Dynamics 35*, 2441-2453.

[37] Cornish-Bowden, A. (2012) *Fundamentals of enzyme kinetics*, 4th completely rev. and greatly enl. ed., Wiley-VCH, Weinheim.

[38] Yang, X., Du, Z., Pu, J., Zhao, H., Chen, H., Liu, Y., Li, Z., Cheng, Z., Zhong, H., and Liao, F. (2013) Classification of difference between inhibition constants of an inhibitor to facilitate identifying the inhibition type, *J Enzyme Inhib Med Chem 28*, 205-213.

[39] Yarlett, N., Wu, G., Waters, W. R., Harp, J. A., Wannemuehler, M. J., Morada, M., Athanasopoulos, D., Martinez, M. P., Upton, S. J., and Marton, L. J. (2007) Cryptosporidium parvum spermidine/spermine N1-acetyltransferase exhibits different characteristics from the host enzyme, *Molecular and biochemical parasitology 152*, 170-180.

[40] Grünewald, S., Steckel, M., Husemann, M., Meyer, H., Han, W., and Ding, Z. (2019) Inhibitors and antagonists of human pycr1, Google Patents.

[41] Li, L., Ye, Y., Sang, P., Yin, Y., Hu, W., Wang, J., Zhang, C., Li, D., Wan, W., Li, R., Ma, L., Xie, Y., and Meng, Z. (2017) Effect of R119G Mutation on Human P5CR1 Dynamic Property and Enzymatic Activity, *Biomed Res Int 2017*, 4184106.

[42] Niesen, F. H., Berglund, H., and Vedadi, M. (2007) The use of differential scanning fluorimetry to detect ligand interactions that promote protein stability, *Nat Protoc 2*, 2212-2221.

[43] Sreerama, N., Venyaminov, S. Y., and Woody, R. W. (1999) Estimation of the number of alpha-helical and beta-strand segments in proteins using circular dichroism spectroscopy, *Protein Sci 8*, 370-380.

[44] Escande-Beillard, N., Loh, A., Saleem, S. N., Kanata, K., Hashimoto, Y., Altunoglu, U., Metoska, A., Grandjean, J., Ng, F. M., Pomp, O., Baburajendran, N., Wong, J., Hill, J., Beillard, E., Cozzone, P., Zaki, M., Kayserili, H., Hamada, H., Shiratori, H., and Reversade, B. (2020) Loss of PYCR2 Causes Neurodegeneration by Increasing Cerebral Glycine Levels via SHMT2, *Neuron 107*, 82-94.e86.

[45] Vedadi, M., Niesen, F. H., Allali-Hassani, A., Fedorov, O. Y., Finerty, P. J., Wasney, G. A., Yeung, R., Arrowsmith, C., Ball, L. J., Berglund, H., Hui, R., Marsden, B. D., Nordlund, P., Sundstrom, M., Weigelt, J., and Edwards, A. M. (2006) Chemical screening methods to identify ligands that promote protein stability, protein crystallization, and structure determination, *Proc Natl Acad Sci U S A 103*, 15835-15840.

[46] Shoemark, D. K., Cliff, M. J., Sessions, R. B., and Clarke, A. R. (2007) Enzymatic properties of the lactate dehydrogenase enzyme from Plasmodium falciparum, *The FEBS journal 274*, 2738-2748.

[47] Forlani, G., Giberti, S., Berlicki, L., Petrollino, D., and Kafarski, P. (2007) Plant P5C reductase as a new target for aminomethylenebisphosphonates, *J Agric Food Chem 55*, 4340-4347.

[48] Inoue, H., Moritani, K., Date, Y., Kohashi, K., and Tsuruta, Y. (1995) Determination of free hydroxyproline and proline in human serum by high-performance liquid chromatography using 4-(5,6-dimethoxy-2-phthalimidinyl)phenylsulfonyl chloride as a pre-column fluorescent labelling reagent, *Analyst 120*, 1141-1145.

[49] Liang, S., Sanchez-Espiridion, B., Xie, H., Ma, J., Wu, X., and Liang, D. (2015) Determination of proline in human serum by a robust LC-MS/MS method: application to identification of human metabolites as candidate biomarkers for esophageal cancer early detection and risk stratification, *Biomed Chromatogr 29*, 570-577.

[50] Fleming, G. A., Hagedorn, C. H., Granger, A. S., and Phang, J. M. (1984) Pyrroline-5-carboxylate in human plasma, *Metabolism 33*, 739-742.

[51] Semon, B. A., and Phang, J. M. (1991) Accumulation of pyrroline 5-carboxylic acid in conditioned medium of cultured fibroblast: stimulatory effects of serum, insulin, and IGF-1, *In Vitro Cell Dev Biol 27A*, 665-669.

[52] Baumgartner, M. R., Rabier, D., Nassogne, M. C., Dufier, J. L., Padovani, J. P., Kamoun, P., Valle, D., and Saudubray, J. M. (2005) Delta1-pyrroline-5-carboxylate synthase deficiency: neurodegeneration, cataracts and

connective tissue manifestations combined with hyperammonaemia and reduced ornithine, citrulline, arginine and proline, *Eur J Pediatr 164*, 31-36.

[53] Aliu, E., Kanungo, S., and Arnold, G. L. (2018) Amino acid disorders, *Ann Transl Med 6*, 471.

[54] Kölker, S., Boy, S. P., Heringer, J., Müller, E., Maier, E. M., Ensenauer, R., Mühlhausen, C., Schlune, A., Greenberg, C. R., Koeller, D. M., Hoffmann, G. F., Haege, G., and Burgard, P. (2012) Complementary dietary treatment using lysine-free, arginine-fortified amino acid supplements in glutaric aciduria type I - A decade of experience, *Mol Genet Metab 107*, 72-80.

Chapter 4

L-thioproline oxidation: Novel Enzyme Function Discovered for human PYCR1 and 2

ABSTRACT

L-thioproline (L-thiazolidine-4-carboxylate, L-T4C) is a cyclic sulfur imino acid analog of L-proline (L-Pro) found in multiple kingdoms of life. The oxidation of L-T4C leads to L-cysteine (L-Cys) formation in bacteria, plants, mammals, and protozoa. The conversion of L-T4C to L-Cys in bacterial cell lysates has been attributed to proline dehydrogenase and L-Δ^1-pyrroline-5-carboxylate (P5C) reductase (PYCR) but detailed kinetic studies have not been conducted. Here, we characterize the dehydrogenase activity of human PYCR isozymes 1 and 2 with L-T4C using $NAD(P)^+$ as the hydride acceptor. Both PYCRs exhibit significant L-T4C dehydrogenase activity, however, PYCR2 displayed nearly 10-fold higher catalytic efficiency (136 M^{-1} s^{-1} versus 13.7 M^{-1} s^{-1}) than PYCR1. Interestingly, no activity was observed with L-Pro and the analog DL-thiazolidine-2-carboxylate (DL-T2C), indicating that the sulfur at the 4-position is critical for PYCRs to utilize L-T4C as a substrate. Structural insights into L-T4C binding interactions were gained by solving a 2.30 Å X-ray crystal structure of a (PYCR1 +L-T4C) complex. L-T4C was found to occupy the same binding site as L-Pro, an observation that was corroborated by inhibition kinetics that showed L-Pro is a competitive inhibitor of PYCR1 (K_{IC}^{app} = 15.7 mM) with respect to L-T4C. Taken together, the evidence assigns a novel enzyme function to human PYCRs, thus we propose that PYCR should be classified as a bifunctional enzyme with a new name, L-thiazolidine-4-and-L-pyrroline-5-carboxylate oxidoreductase (TPCOR).

INTRODUCTION

L-thiazolidine-4-carboxylate (L-T4C) is a metabolite known to occur in various organisms throughout nature from protozoa, bacteria, plants, and mammals.[1,2,3,4,5] L-T4C is an analog of L-Pro (Figure 4.1) thought to derive from L-Cys from the mitochondrial reaction of L-Cys and formaldehyde.[2]

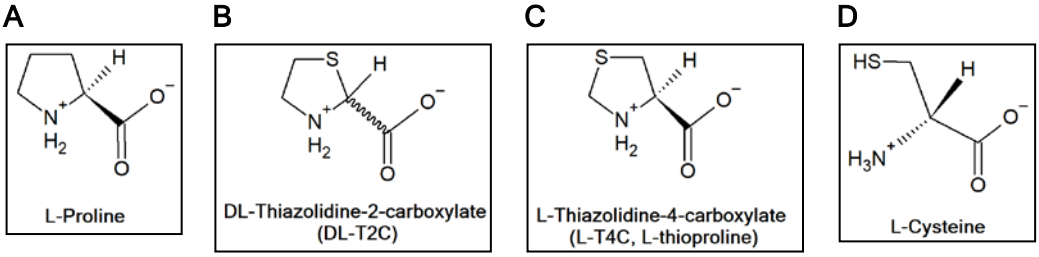

Figure 4.1. Chemical structures of L-Pro, analogs, and L-Cys. (A) L- Pro, (B) DL-T2C, (C) L-T4C, and (D) L-Cys.

L-T4C has been reported to have toxic effects in certain organisms when applied exogenously such as in bacteria and plants. For instance, the toxic effects of L-T4C in *Escherichia coli* are typically attributed to its misincorporation into proteins via the bacterial prolyl-tRNA synthetase, which does not discriminate between L-Pro and L-T4C.[6,7] Elthon et al. (1984) presented evidence that L-T4C treatment strongly influences the accumulation of L-Pro, an important cellular osmolyte and source of energy critical for plant survivability when not in excess, by specific inhibition of L-Pro oxidation in mitochondria isolated from etiolated barley (*Hordeum vulgare*) shoots.[5] The toxic effects of L-T4C have been exploited in its use as an anti-infection agent against various diseases. For instance, Magdaleno et al.'s (2009) study analyzed the effects of L-T4C on parasitic cell viability of the non-infectious epimastigote forms of *Trypanosoma cruzi* and on the infection of mammalian CHO-K1 cells by *T. cruzi*, which leads to the pathology of Chaga's

disease in host cells.[8] According to their findings, L-T4C significantly reduced parasitic cell viability and *T. cruzi* infection rates in CHO-K1 cells.[8] These results led to the suggestion that L-T4C may be a viable treatment against Chaga's disease.

A mechanism by which cells diminish L-T4C toxicity is to convert it to L-Cys, thereby not only removing the L-proline analog but also mobilizing the sulfur into a useable form. Utilizing L-T4C as a source of L-Cys has been shown to be required for the survival of the protozoan *Entamoeba histolytica*, which relies on L-Cys as the principal low-molecular-weight thiol due to the lack of glutathione.[9] Using stable isotope labeling and mass spectrometry, Jeelani et al. (2014) demonstrated that L-T4C was the major source of L-Cys formation in cells, thereby promoting trophozoite growth and protecting protozoan cells against oxidative stress.[9] Consistent with these metabolite findings, lysates of *E. histolytica* were shown to convert L-T4C into L-Cys, however, the enzymes responsible for L-T4C oxidase activity were not identified.[9]

The potential of L-T4C (L-thioproline) to serve as a source of L-Cys and to trap reactive nitrogen species (RNS) has also been explored in humans for various therapeutic applications. The first demonstration of the therapeutic potential of L-thioproline can be traced to Mackenzie et al.'s (1957) report on finding L-thioproline is about five times more potent than L-cysteine in preventing massive pleural effusions and death in thiourea-treated rats.[2] From a chemical structure standpoint, L-T4C's sulfur atom is protected in a ring moiety (Fig. 4.1, C) that only opens and liberates a sulfhydryl group upon uptake into the liver, whereas the sulfur in L-Cys is fully exposed (Fig. 4.1, D) and readily reactive as a

nucleophile prior to cellular uptake.[2] From several clinical reports in the 1960s-1980s, oral tablet or intravenous administration of L-thioproline given to patients suffering from infectious hepatitis, liver insufficiency, or chronic liver cirrhosis demonstrated limited benefits primarily to remedying cell necrosis and correcting levels of transaminase and alkaline phosphatase enzyme activities.[10] Under the moniker of generic Timonacic, L-thioproline (brand names: Hepalidine, Heparegen, etc.) has been used for the treatment of hepatic and biliary diseases, particularly in France.[10]

Despite the interest in L-T4C as a therapeutic L-Cys source in humans or an oxidative stress protectant in various organisms such as protozoa and plants, detailed kinetic studies with L-T4C have yet to be conducted. Two enzymes that have been implicated in L-T4C metabolism from numerous studies are L-proline dehydrogenase (PRODH) and L-Δ^1-pyrroline-5-carboxylate (P5C) reductase (PYCR). Genetic knockout studies in *E. coli* and activity assays with bacterial cell lysates suggests PYCR may have a significant role in converting L-T4C into L-Cys, but the individual contributions of PRODH and PYCR are unclear.[11,7]

Here, we set out to determine the ability of the human PYCR enzymes to catalyze the oxidation of L-T4C. The known function of PYCR is to catalyze the last step in L-Pro biosynthesis by NAD(P)H-dependent reduction of L-P5C into L-Pro. In this study, we characterized the ability of PYCR to catalyze the reverse reaction of reducing $NAD(P)^+$ with L-Pro and analogs, L-T4C and DL-T2C (Figure 4.1) at biologically relevant pH 7.5. We report human PYCR1 and 2 do not exhibit any enzyme activity with L-Pro or DL-T2C, however, notable activity was observed with L-T4C as a substrate. PYCR2 was found to have an apparent

catalytic efficiency with L-T4C of nearly 10-fold higher than PYCR1. A 2.30 Å experimental X-ray crystal structure of the binary complex (PYCR1+L-T4C) was solved, which implies molecular details for the hydride transfer step from L-T4C to $NAD(P)^+$. L-Pro was also shown to be a competitive inhibitor of PYCR1 with respect to L-T4C, indicating that L-T4C occupies the L-proline-binding site. In summary, the experimental evidence gathered here assigns a novel enzyme function to human PYCRs, thus expanding its physiological role.

MATERIALS AND METHODS

Materials, Reagents, and Enzymes

MilliQ-Ultra purified water was used for the preparation of all buffers and chemicals in the experiments. The same reagents mentioned in chapter three were accessed and used for these studies, including the purchases of L-thiazolidine-4-carboxylic acid and DL-thiazolidine-2-carboxylic acid from Millipore-Sigma. Human PYCR1 was graciously provided by Dr. John J. Tanner's group after following an expression and purification procedure as described previously in chapter two.[12] A detailed description of the expression and purification conditions for human PYCR2 is provided in appendix chapter B.

Kinetic characterization of PYCR reverse activity.

The majority of reaction components and reaction conditions from the methods described in chapters two and three remain consistent in these studies, yet there are some notable exceptions. For instance, stock solutions of L-T4C, DL-T2C, and L-Pro were each adjusted to pH 7.5 using 6 M NaOH prior to performing the assays. Assays were performed at 37 °C in 0.1 M Tris-HCl (pH 7.5) reaction buffer containing 0.01% Brij-35 detergent, 1 mM $NAD(P)^+$ (pH 8.0), 1

mM EDTA (pH 7.5), and different test substrate compounds of 10 mM L-proline (pH 7.5), 10 mM L-T4C (pH 7.5), and 10 mM DL-T2C (pH 7.5). The reaction components were pre-warmed for 5 min in a 1.5 mL microtube at 37 °C and then transferred to a 1 cm path length polystyrene rectangular cuvette (USA Scientific). The assay (600 µl total volume) was initiated by adding PYCR1 or 2 enzyme (0.6 µM final concentration) and reaction progress was monitored at 340 nm using a Varian Cary 50-UV/VIS spectrophotometer at room temperature for 10 min duration.

For reverse direction steady-state kinetics, the parameters k_{cat} and K_M for L-T4C were determined by holding $NADP^+$ fixed (1 mM) while varying L-T4C (0-25 mM). In assays varying L-T4C, 1 M Tris-HCl (pH 7.5) buffer was added to each assay to maintain an ionic strength of approximately 450-460 mM $Tris^+Cl^-$. L-proline inhibition studies were performed under the same conditions with 0.6 µM PYCR1 enzyme (final concentration) with $NADP^+$ fixed (1 mM) and L-T4C varied (0-25 mM) at different concentrations of L-proline (0-20 mM).

For both steady-state kinetics and ligand inhibition kinetics, the reaction components were all pre-warmed for 5 min, combined in a 1.5 ml microtube, positioned in a 37 °C water bath for 5 min, then transferred into a cuvette with the addition of enzyme to initiate the reaction. Each cuvette measurement had been zeroed against blanks omitting L-T4C, and all assays were performed in triplicate. Initial velocities were calculated from the linear increase in absorbance within a one minute window in the initial 2.5 min and quantifying NAD(P)H formation (ε_{340} = 6.22 mM^{-1} cm^{-1})[7,13] according to the Beer-Lambert-Bouguer law.[14,15,16] Data (mean ± standard deviation) are plotted as variable substrate concentration in

units mM (horizontal axis) versus initial reaction velocity of NAD(P)H product formation in units μM s^{-1} (vertical axis). The data were fit by nonlinear regression analysis to the Henri-Michaelis-Menten equation using SigmaPlot 12.0. Ligand inhibition data was analyzed by Henri-Michaelis-Menten and linear Hanes-Woolf plots. The apparent enzyme-inhibitor dissociation constant (K_{IC}) was determined by a fit of the data to a Competitive Inhibition (Full) Model, which was the highest-ranked R^2 inhibition model of the Enzyme Kinetics Wizard Add-In module in SigmaPlot 12.0.

RESULTS

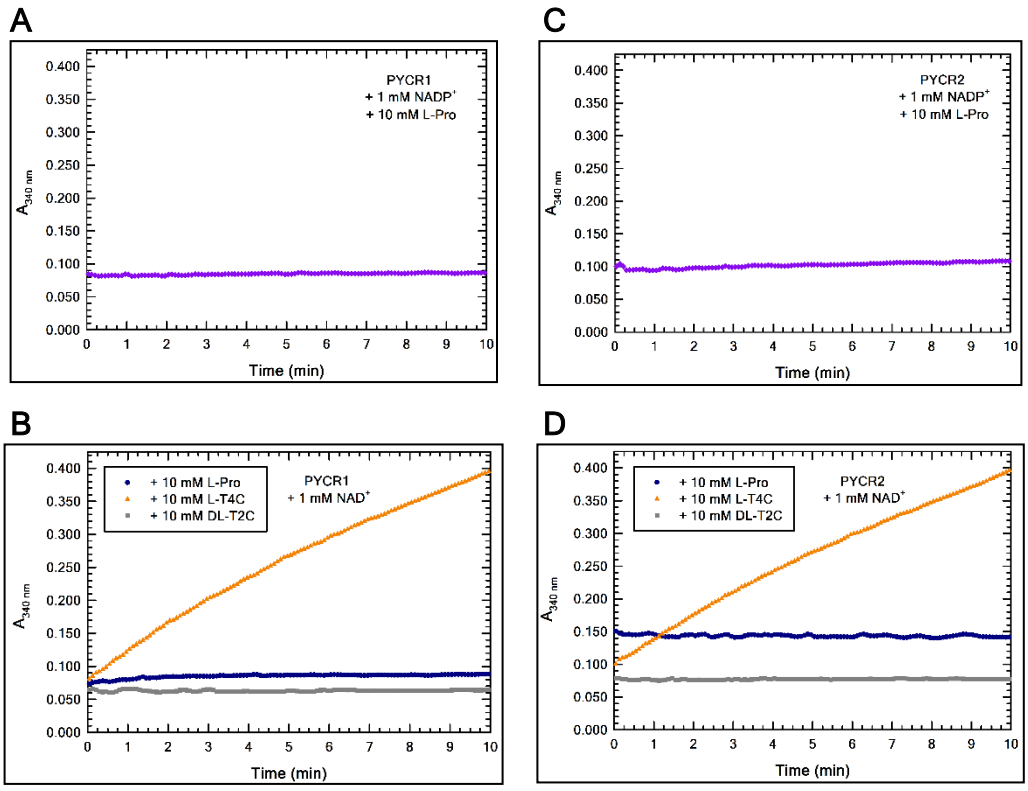

Figure 4.2. PYCR reverse activity with L-Pro and analogs. Final enzyme concentration was 0.6 μM for each assay. Progress of the reaction was monitored for 10 min by following the absorbance at 340 nm. Time-course absorbance profiles of PYCR1 reverse activity with (A) 1 mM $NADP^+$ + 10 mM L-Pro or with (B) 1 mM NAD^+ + 10 mM L-Pro or its analog L-T4C or DL-T2C. Time-course absorbance profiles of PYCR2 reverse activity with (C) 1 mM $NADP^+$ + 10 mM L-Pro or with (D) 1 mM NAD^+ + 10 mM L-Pro or its analog L-T4C or DL-T2C.

PYCR reverse activity with L-Pro, L-T4C, and DL-T2C

The ability of PYCR to catalyze the reduction of $NAD(P)^+$ with L-proline, L-T4C, and DL-T2C was examined at pH 7.5 for 10 min. The results shown in Fig. 4.2 and Table 4.1 demonstrate that NADPH formation is only observed in PYCR reverse activity assays using L-T4C as the substrate. Thus, neither PYCR1 nor PYCR2 can catalyze the reverse reaction of L-proline oxidation and $NAD(P)^+$ reduction, consistent with the forward reaction toward L-proline biosynthesis being strongly favored by PYCRs.

Table 4.1. Human PYCR reverse activity with L-Pro and its analogs[a]

Enzyme[b]	Substrate[c]	Cofactor[d]	$A_{340\ nm}$/min	NAD(P)H formation ($\mu M\ s^{-1}$)[e]
PYCR1	L-Pro	$NADP^+$	-0.0006	0
	L-Pro	NAD^+	0.0059	~ 0
	L-T4C	NAD^+	0.0438	0.1175
	DL-T2C	NAD^+	0.0004	~ 0
PYCR2	L-Pro	$NADP^+$	-0.0082	0
	L-Pro	NAD^+	-0.0017	0
	L-T4C	NAD^+	0.0374	0.1003
	DL-T2C	NAD^+	-0.0015	0

[a]Enzyme activity assay involved measurement for the change in absorbance at 340 nm over 10 min time duration.
[b]Final enzyme concentration of 0.6 μM in assay.
[c]Final concentration of 10 mM for L-Pro, L-T4C, and DL-T2C.
[d]Final NAD(P)H concentration of 1 mM.
[e]Initial reaction velocity of NAD(P)H formation calculated with $\varepsilon_{NAD(P)H\ at\ 340\ nm}$ = 6.22 $mM^{-1}\ cm^{-1}$.

In terms of quantitative comparisons of reverse activity, PYCR1 shows nearly 3.5-fold higher reaction velocity with 10 mM L-T4C in the presence of 1 mM NAD^+ compared to the corresponding value in the presence of 1 mM $NADP^+$.

Conversely, PYCR2 shows nearly 2.5-fold higher reaction velocity with 10 mM L-T4C in the presence of 1 mM $NADP^+$ compared to the corresponding value in the presence of 1 mM NAD^+.

Steady-state kinetics analysis of PYCR reverse activity with L-T4C

The apparent steady-state kinetic parameters k_{cat} and K_M were then determined for L-T4C by keeping $NADP^+$ fixed while varying the L-T4C substrate. Henri-Michaelis-Menten plots of the data are shown in Fig. 4.2 for PYCR1 and PYCR2.

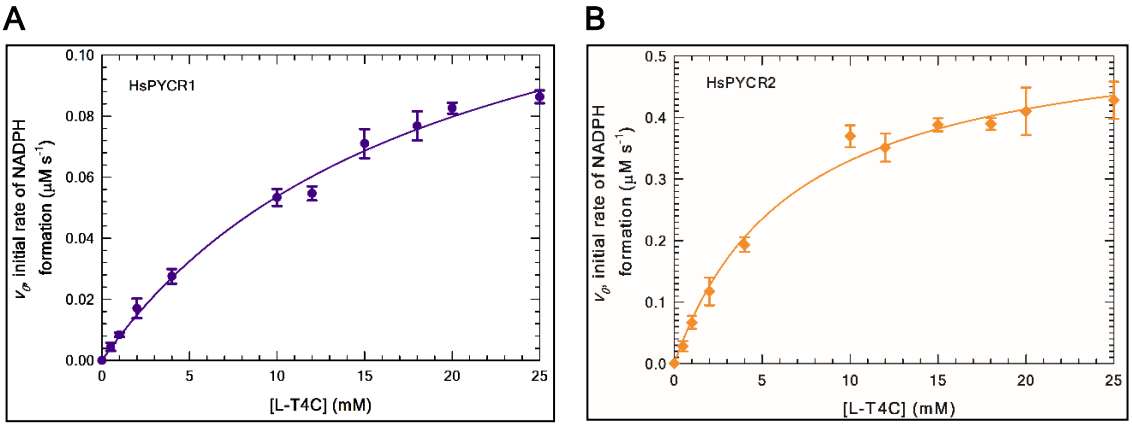

Figure 4.3. Steady-state kinetics analysis of PYCR reverse activity with L-T4C. Final enzyme concentration of 0.6 μM (A) PYCR1 and (B) PYCR2 were used. Data are plotted as (mean ± SD) of three technical replicates and fit to the Henri-Michaelis-Menten equation by non-linear least-squares regression in SigmaPlot 12.0.

Table 4.2. Steady-state kinetics analysis of PYCR reverse activity[a] with L-T4C

Enzyme[b]	Varied Substrate	Fixed Substrate[c]	$K_M{}^{app}$ (mM)	$k_{cat}{}^{app}$ (s^{-1})	($k_{cat}{}^{app}/K_M{}^{app}$) ($M^{-1}$ s^{-1})
PYCR1	L-T4C	$NADP^+$	18.9 ± 2.9	0.26 ± 0.02	13.7 ± 2.3
PYCR2	L-T4C	$NADP^+$	6.8 ± 0.9	0.92 ± 0.04	136 ± 19

[a](Value ± Std error) are the apparent best-fit parameters from non-linear least-squares fit of the data to the Henri-Michaelis-Menten equation using SigmaPlot 12.0 (version 12.0.0.182, Systat Software). Data plotted as the (mean ± SD) of n=3 technical replicates.
[b]Final enzyme concentration is 0.6 μM.
[c]Final $NADP^+$ concentration fixed at 1 mM.

Both PYCR1 and PYCR2 achieved saturation kinetics with L-T4C substrate for nonzero maximal limiting reaction velocities (V_{lim}) of 0.16 μM s^{-1} and 0.55 μM s^{-1}, respectively. PYCR2 exhibited higher catalytic activity than PYCR1 with k_{cat}^{app} approaching 1 s^{-1} (Table 4.2). The nearly 4-fold higher k_{cat}^{app} and 3-fold lower K_m^{app} values for PYCR2 result in a 10-fold higher catalytic efficiency with L-T4C relative to PYCR1 (Table 4.2).

Structural and ligand inhibition kinetics analysis of L-T4C binding in PYCR1

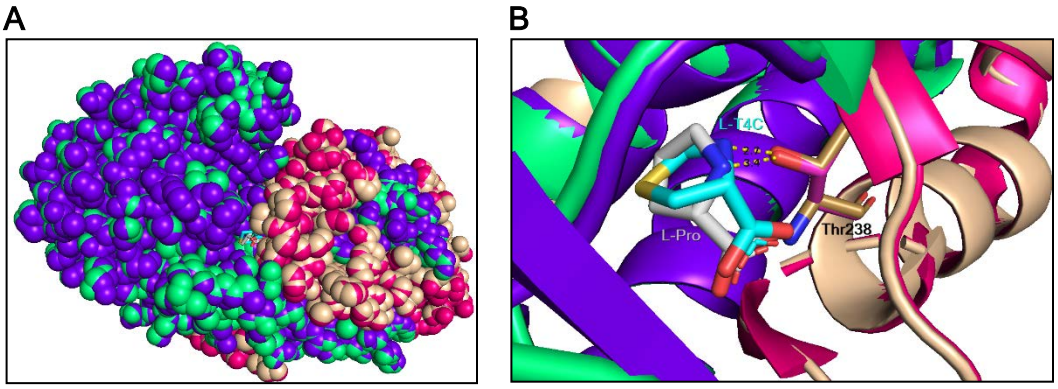

Figure 4.4. Superimposed X-ray crystal structures of PYCR1—L-T4C and PYCR1—L-Pro binary complexes. (A) Ball-space-filling model of dimeric superimposed structures of PYCR1—L-T4C (purple blue and wheat partner protomers) and PYCR1—L-Pro (lime green and hot pink partner protomers) binary complexes. The active site is formed at interface of partner protomers with L-T4C (cyan sticks) and L-Pro (gray sticks) present deep in active site. (B) Ribbon cartoon model of superimposed structures with zoomed-in view of active site showing hydrogen bond interaction (2.7 Å) between side chain hydroxyl group of Thr238 and imine nitrogen (blue colored atom) of L-T4C, analogous to hydrogen bond interaction (3.4 Å) between side chain hydroxyl group of Thr238 and imine nitrogen (blue colored atom) of L-Pro. Illustrations of the 2.30 Å X-ray crystal structure of the PYCR1—L-T4C complex and of the 1.90 Å X-ray crystal structure of PYCR1—L-Pro complex (PDB code 5UAU)[12] were made with PyMol.[17] The X-ray crystal structures of human PYCR1 soaked with 50 mM L-T4C in the former case and soaked with 1.8 M L-Pro in the latter case, were both graciously provided by Dr. John J. Tanner and Dr. Emily Christensen.

To further characterize L-T4C as a substrate of PYCR, structural and kinetic evidence was generated to support that L-T4C binds in the same active site region of PYCR1 as L-proline and consequently as the L-P5C substrate. In

previous studies (see chapter three) with PYCR1, a 1.90 Å X-ray crystal structure of the binary complex of PYCR1+L-Pro was solved (PDB code 5UAU).[12] The structure, along with evidence from product inhibition kinetics, showed that L-Pro and L-P5C occupy the same binding site near NADPH in PYCR1. As shown in Fig. 4.4, our collaborators (Dr. Emily Christensen and Dr. John J. Tanner) solved a 2.30 Å X-ray crystal structure of L-T4C complexed with PYCR1. The electron density of L-T4C is observed in the same active site binding pocket as previously shown for L-Pro. Additionally, the highly conserved active site residue Thr238's side chain hydroxyl group forms a 2.7 Å hydrogen bond interaction with the imine nitrogen of L-T4C, which is analogous to hydrogen bond interaction (3.4 Å) between side chain hydroxyl group of Thr238 and imine nitrogen of L-Pro in the superimposed structure of the PYCR1—L-Pro binary complex. Thus, L-T4C appears to bind to the PYCR1 active site in a manner similar to L-proline.

In tow with this structural interpretation, we performed ligand inhibition kinetics with L-proline to test whether L-T4C binds to the same site as L-proline in PYCR1. Upon holding $NADP^+$ concentration constant at 1 mM and varying L-T4C substrate (0-25 mM) at different L-proline concentrations (0-20 mM), the apparent K_M (K_M^{app}) for L-T4C was observed to trend upward while the apparent k_{cat} (k_{cat}^{app}) stayed relatively constant (Table 4.3 and Fig.4.5). With increasing L-Pro concentration, trends of an overwhelming increasing value of the K_M^{app} with a fairly unchanging value of the V_{max} agree well with the model of competitive inhibition with an apparent competitive inhibition constant (K_{IC}^{app}) of 15.7 mM L-Pro (Fig.4.5, A and Table 4.3).[18] Hanes-Woolf plot analysis of the L-proline inhibition data shows a parallel linear pattern that is consistent with competitive

inhibition (Figure 4.5, B). In particular, the increasing vertical axis intercept (K_M^{app}/V_{max}) effect shown in Figure 4.5, panel B indicates L-Pro is a competitive inhibitor[19] with respect to the L-T4C substrate.

Table 4.3. Steady-state kinetic parameters for L-proline ligand inhibition of PYCR1 with varied L-T4C[a,b,c]

L-proline (mM)	K_M^{app} (mM)	k_{cat}^{app} (s^{-1})	(k_{cat}^{app}/K_M^{app}) (M^{-1} s^{-1})	K_{IC}^{app} (mM)
0	18.9 ± 2.9	0.26 ± 0.02	13.7 ± 2.3	
5	32.0 ± 6.3	0.27 ± 0.35	8.4 ± 11.1	15.7 ± 1.1[d]
10	35.1 ± 6.9	0.26 ± 0.35	7.5 ± 10.1	
20	36.8 ± 7.6	0.23 ± 0.03	6.3 ± 1.6	

[a](Value ± Std error) are reported for the apparent best-fit parameters of non-linear least-squares fit to the Henri-Michaelis-Menten equation using SigmaPlot 12.0 (version 12.0.0.182, Systat Software) with data plotted as (mean ± SD) of n=3 technical replicates.
[b]Final enzyme concentration is 0.6 µM.
[c]$NADP^+$ concentration was fixed at 1 mM while L-T4C concentration was varied 0-25 mM.
[d]Apparent competitive inhibition constant, K_{IC}^{app}, was estimated by globally fitting the data (0.5-25 mM) to a competitive inhibition (full) model using the Enzyme Kinetics Wizard Add-In on SigmaPlot 12.0 (version 12.0.0.182, Systat Software).

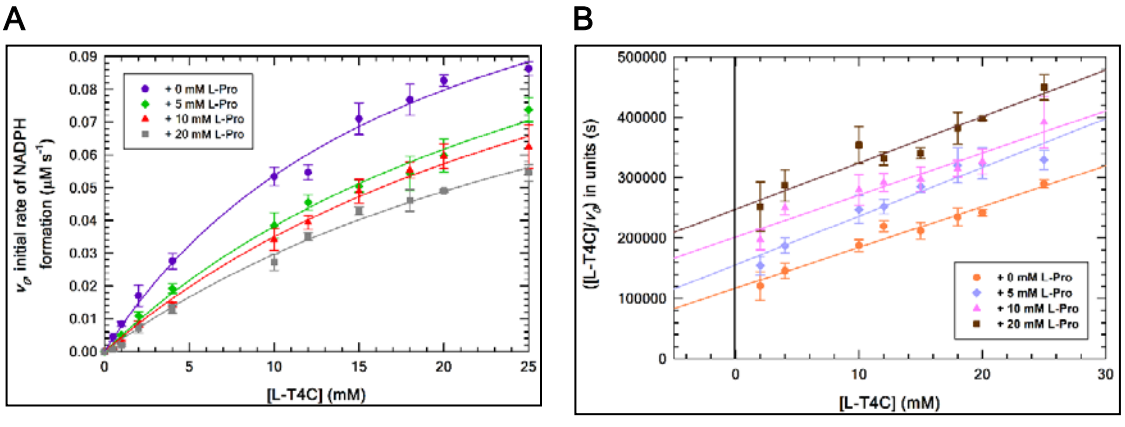

Figure 4.5. L-Pro ligand inhibition kinetics of PYCR1 with varied L-T4C substrate. (A) Henri-Michaelis-Menten plots of assays performed at different L-proline concentrations (0-20 mM) while varying L-T4C (0-25 mM) and holding $NADP^+$ concentration constant (1 mM). (B) Hanes-Woolf plot of the (2-25 mM) data in

panel A. Final enzyme concentration of 0.6 µM PYCR1 was used. Data are plotted as (mean ± SD) of n=3 technical replicates with non-linear least-squares fits to the Henri-Michaelis-Menten equation and linear regression fits to the Hanes-Woolf equation using SigmaPlot 12.0.

DISCUSSION

The kinetic data shown here directs attention to the chemical importance of

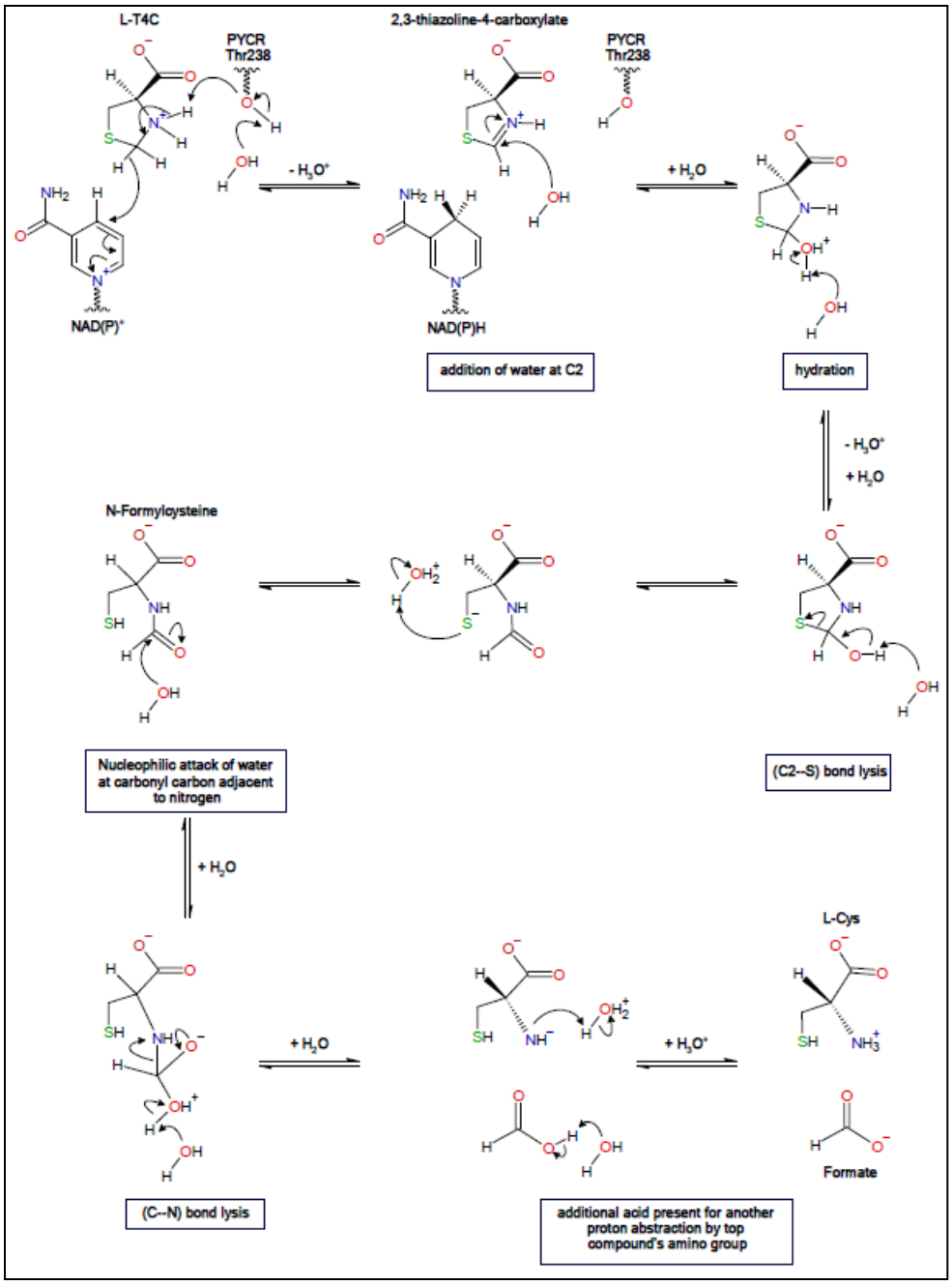

Figure 4.6. Proposed catalytic mechanism of L-T4C initial oxidation by PYCR.

sulfur in the structure of L-proline analogs. As depicted in Fig. 4.1, the insertion of the sulfur atom at the C4 position of the pyrrolidine ring of L-Pro enables oxidation of L-T4C whereas sulfur at the C3 position of the pyrrolidine ring of L-Pro, as in DL-T2C, does not enable oxidation of the L-proline analog. A reaction mechanism for the oxidation of L-T4C by PYCR is proposed in Fig. 4.6. The mechanism involves a hydride transfer from the C2 position in L-T4C to $NADP^+$ followed by nonenzymatic hydrolysis to form products L-cysteine and formate (which later becomes formaldehyde). The sulfur being adjacent to the C2 position likely lowers the pK_a of the hydrogen atoms at C2 and promotes electron delocalization between the N1 and C2 atoms. These electronic factors must be sufficient enough to enable PYCR to catalyze hydride transfer from the C2 of L-T4C to $NADP^+$. In DL-T2C, the sulfur is too far removed from the site of hydride transfer to have an impact, thus no activity is observed with this L-proline analog.

Both PYCR1 and PYCR2 catalyze the oxidation of L-T4C at a significant rate, however, PYCR2 exhibits a 10-fold higher catalytic efficiency than PYCR1. When comparing the L-T4C oxidative and L-P5C reductive enzyme activities, PYCR1 and PYCR2 both exhibit $>10^3$-fold higher catalytic efficiency in the forward direction reaction with L-P5C (as shown in data from chapter three) consistent with the main function of PYCRs in L-proline biosynthesis.

L-T4C has long been studied as an anti-aging therapeutic. For example, dietary supplementation with L-T4C (2.0 g/kg) in mice was shown to increase median and maximal life span by approximately 10–29% in both genders and improve neuromuscular coordination and exploratory function.[20] The mechanisms by which L-T4C enhances lifespan in mice appear to be multifaceted and likely

involve the protection of mitochondrial function. Navarro et al. (2007) found that L-T4C-supplemented diets given to mice ad libitum resulted in approximately 51-74% curtailment of aging-related reductions of brain mitochondrial enzyme activities of NADH-dehydrogenase, cytochrome c oxidase, and mitochondrial nitric oxide synthase in old and senescent mice.[20]

Other anti-aging effects of T4C include its ability to act as an in vivo protector against protein aggregation and as a scavenger of reactive nitrogen and oxygen species, and N-nitroso compounds. In a recent mouse study by Lyu et al. (2020), L-T4C significantly diminished aggregation of oxidized bovine serum albumin (BSA), possibly by directly interacting with BSA via hydrogen bonds and van der Waals interactions.[21] In the same study, the ability of L-T4C to prevent oxidative damage in brain tissue was tested against five other antioxidants. L-T4C showed the highest antioxidant effects in oxidized isolates of mouse brain tissue with a nearly 1.4-fold drop in malondialdehyde content (readout for membrane lipid peroxidative damage) and nearly 1.3-fold increase in superoxide dismutase enzyme activity (readout for cellular antioxidant activity).[21]

Over the years, L-T4C's high capacity for trapping reactive nitrogen species and N-nitroso compounds has been exploited on the drug market for protection against liver diseases and gastrointestinal disorders. In mammals, many carcinogenic N-nitrosamines (e.g., N-nitrosomorpholine) are endogenously formed inside the acidic stomach by the reaction between amines and nitrite, which originates from nitrate produced by two primary sources: bacterial flora in the oral cavity and activated macrophages.[22] It has also been established that endogenously produced N-nitrosothioproline and N-nitrosoproline comprise the

majority of excreted N-nitroso compounds found in urine.[22] However, in vitro reaction kinetics show that N-nitrosation of L-T4C into N-nitrosothioproline occurs 10^3 times faster than that of L-proline into N-nitrosoproline.[23] Miwa et al.'s (1989) in vitro study reported that the incubation of 5 mM morpholine with activated murine macrophages resulted in the formation of 1.06 pM N-nitrosomorpholine, which could be strongly curtailed by treatment with 5 mM L-T4C.[22] These results led Miwa et al. (1989) to propose that L-T4C can trap nitrosating-compounds produced by activated macrophages in non-human and human animals.[22] In a more recent study of pathology with Barrett's esophagus and development of esophageal cancer, Kumagai et al. (2004) evaluated the nitroxide scavenging efficacy of L-T4C using a surgically made duodenal reflux model in rats. Experimental treatment of 0.5% L-T4C was used to examine whether L-T4C could lower reactive nitrogen species (e.g., nitric oxide and peroxynitrite, and N-nitroso compounds) present in the contents of the gastroduodenal reflux and thereby minimize pathology.[24] Upon histological examination, the L-T4C treated rats had milder forms of mucosal changes with lesser degrees of inflammation and zero presence of esophageal adenocarcinoma compared to the control group. These exciting results suggest L-T4C inhibits the production of N-nitroso compounds in the gastroduodenal reflux contents, a property of potential therapeutic benefit in esophageal cancer.[24]

Another important aspect of L-T4C is its impact on biogenic aldehydes. L-T4C has been suggested to be a source of formaldehyde, presumably through its metabolism by L-proline dehydrogenase and PYCR. Garnier et al. (1980) assessed the clinical toxicity of L-T4C in patients and concluded that overdosage

of L-T4C overwhelms the metabolic capacity of the liver, thereby leading to L-T4C distribution throughout the body including the cerebrospinal fluid (CSF). It was proposed that metabolic degradation of L-T4C in the intrameningeal tissue results in the release of toxic formaldehyde, which causes the acute central nervous system (CNS) symptoms of epileptic seizures and convulsions.[25] In a separate study investigating the therapeutic potential of L-T4C in cancer, Newman et al. (1980) showed that the toxicity of L-T4C administered at 400 mg/kg to mice and rats could be counteracted by barbiturate anesthesia with no acute CNS symptoms of epileptic seizures and convulsions.[26] Thus, it was proposed that the acute toxic effects of L-T4C in animals may not be a direct consequence of formaldehyde released from L-T4C, but rather the inactivation of important biogenic aldehydes by L-T4C, particularly in the brain.[10] From high performance liquid chromatography (HPLC) and mass spectrometry experiments, Susillo et al. (1989) reported on the involvement of L-cysteine in the brain metabolism of biogenic aldehydes, i.e. 5-hydroxyindole-3-acetic acid (5'-HIAAL), by forming L-thiazolidine-4-carboxylic acid derivatives, perhaps as a control measure to limit labile biogenic aldehydes by the rapid intracellular inactivation of the compounds.[27] Essentially, the metabolic transformation of indoleamines into biologically inactive L-T4C derivatives is catalyzed by two enzymes located in separate subcellular compartments of neuronal cells.[27] Monoamine oxidase located in the outer mitochondrial membrane converts 5-hydroxytryptamine (5-HT) into biogenic aldehyde (5'-HIAAL) and then carbon-sulfur lyase in the cytosol cleaves off the cysteinyl moiety from the spontaneously formed condensation product of (L-cysteine + 5'-HIALL), namely (4R)-2-[3'-(5'-hydroxyindoly1)-

methyl]-1,3-thiazolidine-4-carboxylic acid (5'-HITCA), to liberate a reactive free aldehyde 5'-HIAA product.[27]

In summary, we show here that PYCR1 and PYCR2 exhibit activity with L-T4C that is likely to be biologically significant and contribute to the physiological effects reported thus far with L-T4C. The 2.30 Å X-ray crystal structure of the PYCR1+L-T4C complex shows that L-T4C binds in the active site of PYCR1 which is consistent with the mechanism shown in Fig. 4.6 with hydride transfer from L-T4C to $NADP^+$. L-proline ligand inhibition kinetic studies corroborate the interpretation of the structural data and indicate that L-T4C and L-proline occupy the same binding pocket in PYCR1. Whether L-cysteine and formaldehyde also bind to PYCR1 is not known, but would be an important question to pursue in future research. A key underlying point of our findings is that human PYCRs function as a metabolic lynchpin that links L-Pro biosynthesis with L-Cys formation. In conclusion, a new enzyme activity is assigned to human PYCRs. We thus propose that PYCR be renamed for its bifunctional activities as L-thiazolidine-4-and-L-pyrroline-5-carboxylate oxidoreductase (TPCOR).

REFERENCES

[1] CAVALLINI, D., DE MARCO, C., MONDOVI, B., and TRASARTI, F. (1956) Studies of the metabolism of thiazolidine carboxylic acid by rat liver homogenate, *Biochim Biophys Acta 22*, 558-564.

[2] MACKENZIE, C. G., and HARRIS, J. (1957) N-formylcysteine synthesis in mitochondria from formaldehyde and L-cysteine via thiazolidinecarboxylic acid, *J Biol Chem 227*, 393-406.

[3] JOHNSON, A. B., and STRECKER, H. J. (1962) The interconversion of glutamic acid and proline. IV. The oxidation of proline by rat liver mitochondria, *J Biol Chem 237*, 1876-1882.

[4] Unger, L., and DeMoss, R. (1966) Metabolism of a proline analogue, l-thiazolidine-4-carboxylic acid, by Escherichia coli, *Journal of bacteriology 91*, 1564-1569.

[5] Elthon, T. E., and Stewart, C. R. (1984) Effects of the proline analog l-thiazolidine-4-carboxylic acid on proline metabolism, *Plant physiology 74*, 213-218.

[6] Papas, T. S., and Mehler, A. H. (1970) Analysis of the amino acid binding to the proline transfer ribonucleic acid synthetase of Escherichia coli, *J Biol Chem 245*, 1588-1595.

[7] Deutch, C. E., Klarstrom, J. L., Link, C. L., and Ricciardi, D. L. (2001) Oxidation of l-Thiazolidine-4-Carboxylate by Δ1-Pyrroline-5-Carboxylate Reductase in Escherichia coli, *Current Microbiology 42*, 442-446 LA - English.

[8] Magdaleno, A., Ahn, I. Y., Paes, L. S., and Silber, A. M. (2009) Actions of a proline analogue, L-thiazolidine-4-carboxylic acid (T4C), on Trypanosoma cruzi, *PLoS One 4*, e4534.

[9] Jeelani, G., Sato, D., Soga, T., Watanabe, H., and Nozaki, T. (2014) Mass spectrometric analysis of L-cysteine metabolism: physiological role and fate of L-cysteine in the enteric protozoan parasite Entamoeba histolytica, *mBio 5*, e01995.

[10] Weber, H. U., Fleming, J. F., and Miquel, J. (1982) Thiazolidine-4-carboxylic acid, a physiologic sulfhydryl antioxidant with potential value in geriatric medicine, *Arch Gerontol Geriatr 1*, 299-310.

[11] Deutch, C. E. (1992) Oxidation of L-thiazolidine-4-carboxylate by L-proline dehydrogenase in Escherichia coli, *J Gen Microbiol 138 Pt 8*, 1593-1598.

[12] Christensen, E. M., Patel, S. M., Korasick, D. A., Campbell, A. C., Krause, K. L., Becker, D. F., and Tanner, J. J. (2017) Resolving the cofactor-binding site in the proline biosynthetic enzyme human pyrroline-5-carboxylate reductase 1, *Journal of Biological Chemistry 292*, 7233-7243.

[13] De Ingeniis, J., Ratnikov, B., Richardson, A. D., Scott, D. A., Aza-Blanc, P., De, S. K., Kazanov, M., Pellecchia, M., Ronai, Z. e., Osterman, A. L., and Smith, J. W. (2012) Functional Specialization in Proline Biosynthesis of Melanoma, *PLoS ONE 7*, e45190 EP -.

[14] Beer. (1852) Bestimmung der Absorption des rothen Lichts in farbigen Flüssigkeiten, *Annalen der Physik 162*, 78-88.

[15] Lambert, J. H., and Klett, E. (1760) *Photometria sive de mensura et gradibus luminis, colorum et umbrae*, Klett.

[16] Bouguer, P. (1729) *Essai d'optique sur la gradation de la lumière*, chez Claude Jombert, ruë S. Jacques, au coin de la ruë des Mathurins, à l ….

[17] DeLano, W. L. (2015) The PyMOL Molecular Graphics System, version 1.8 ed., Schrodinger, LLC, New York.

[18] Yang, X., Du, Z., Pu, J., Zhao, H., Chen, H., Liu, Y., Li, Z., Cheng, Z., Zhong, H., and Liao, F. (2013) Classification of difference between inhibition constants of an inhibitor to facilitate identifying the inhibition type, *J Enzyme Inhib Med Chem 28*, 205-213.

[19] Yarlett, N., Wu, G., Waters, W. R., Harp, J. A., Wannemuehler, M. J., Morada, M., Athanasopoulos, D., Martinez, M. P., Upton, S. J., and Marton, L. J. (2007) Cryptosporidium parvum spermidine/spermine N1-acetyltransferase exhibits different characteristics from the host enzyme, *Molecular and biochemical parasitology 152*, 170-180.

[20] Navarro, A., Sánchez-Pino, M. J., Gómez, C., Bández, M. J., Cadenas, E., and Boveris, A. (2007) Dietary thioproline decreases spontaneous food intake and increases survival and neurological function in mice, *Antioxid Redox Signal 9*, 131-141.

[21] Lyu, M., Liu, H., Ye, Y., and Yin, Z. (2020) Inhibition effect of thiol-type antioxidants on protein oxidative aggregation caused by free radicals, *Biophys Chem 260*, 106367.

[22] Miwa, M., Tsuda, M., Kurashima, Y., Hara, H., Tanaka, Y., and Shinohara, K. (1989) Macrophage-mediated N-nitrosation of thioproline and proline, *Biochem Biophys Res Commun 159*, 373-378.

[23] Tahira, T., Tsuda, M., Wakabayashi, K., Nagao, M., and Sugimura, T. (1984) Kinetics of nitrosation of thioproline, the precursor of a major nitroso compound in human urine, and its role as a nitrite scavenger, *Gan 75*, 889-894.

[24] Kumagai, H., Mukaisho, K., Sugihara, H., Miwa, K., Yamamoto, G., and Hattori, T. (2004) Thioproline inhibits development of esophageal adenocarcinoma induced by gastroduodenal reflux in rats, *Carcinogenesis 25*, 723-727.

[25] Garnier, R., Conso, F., Efthymiou, M. L., and Fournier, E. (1980) Thioproline, *Lancet 1*, 365.

[26] Newman, R. A., Hacker, M. P., McCormack, J. J., and Krakoff, I. H. (1980) Pharmacologic and toxicologic evaluation of thioproline: a proposed nontoxic inducer of reverse transformation, *Cancer Treat Rep 64*, 837-844.

[27] Susilo, R., Rommelspacher, H., and Höfle, G. (1989) Formation of thiazolidine-4-carboxylic acid represents a main metabolic pathway of 5-hydroxytryptamine in rat brain, *J Neurochem 52*, 1793-1800.

Chapter 5

Cautionary tale of using tris(alkyl)phosphine reducing agents with NAD^+-dependent enzymes

ABSTRACT

Protein purification protocols typically include disulfide bond reducing agents to thwart unwanted thiol oxidation and protein aggregation. Various disulfide bond reducing agents include dithiothreitol, β-mercaptoethanol, glutathione, and phosphine compounds such as tris(2-carboxyethyl)phosphine (TCEP) and tris(3-hydroxypropyl)phosphine (THPP). Δ^1-pyrroline-5-carboxylate (P5C) reductase (PYCR) catalyzes the final step of L-proline (L-Pro) biosynthesis by reducing L-P5C into L-Pro using NAD(P)H as a hydride donor. When probing the ability of PYCR to operate in the reverse direction of L-Pro oxidation using NAD^+, we observed a rapid non-enzymatic reaction between NAD^+ and reducing agents TCEP and THPP. The product of the reaction with TCEP exhibits a maximum absorbance peak at 334 nm and forms with an apparent forward association rate constant of 490.5 $M^{-1}s^{-1}$. The reaction with TCEP is reversible with an apparent equilibrium association constant of 20.1 M^{-1}. NMR characterization (^{1}H-, ^{13}C-, and ^{31}P-NMR) of the reaction product revealed that a covalent adduct is formed with the phosphorus of the phosphine compound and the C4 atom of the dihydronicotinamide ring of NAD^+. The findings here serve to caution researchers when using TCEP or THPP in experimental protocols that include $NAD(P)^+$-dependent enzymes.

INTRODUCTION

In all domains of life, L-proline is biosynthesized from L-glutamate via three enzymatic steps with the last step catalyzed by L-Δ^1-pyrroline-5-carboxylate

(L-P5C) reductase (PYCRs or P5CRs). PYCR reduces L-P5C into L-Pro using NAD(P)H as the hydride donor. Besides providing L-proline for protein biosynthesis, another function of PYCR is to provide $NAD(P)^+$ redox equivalents for other pathways such as the oxidative branch of the pentose phosphate pathway in plants and animals. [1] PYCR has been found to have important roles in plant stress response, bacterial pathogenesis, and in humans, is upregulated in different types of cancer.[2,3]

Studies of PYCR or P5CR from various organisms have assayed the reverse reduction reaction of $NAD(P)^+$ with L-Pro to characterize the kinetic activity of PYCR. In some cases, L-proline analogs such as L-thiazolidine-4-carboxylate (L-T4C) and 3,4-dehydro-L-proline were used as the substrate.[4] Because the L-P5C substrate is not commercially available and L-P5C is not amenable for long-term storage, PYCR assays in the reverse direction are more easily deployed. In particular, PYCR assays in the reverse direction are more readily applied in high-throughput screening of compound libraries seeking to identify small molecule inhibitors of PYCR. We, therefore, sought to test the reverse activity of human PYCR, namely of human isoforms 1 (HsPYCR1) and (HsPYCR2). Under our assay conditions, however, we did not detect any reverse activity of PYCR with $NAD(P)^+$ and L-Pro, a finding which contrasts with previous reports on PYCRs.[5,6]

Amid these experiments, we unexpectedly discovered a chemical reaction between NAD^+ and reducing agents tris(3-hydroxypropyl)phosphine (THPP) and tris(2-carboxyethyl)phosphine (TCEP). THPP and TCEP are tris(alkyl)phosphine compounds commonly used as disulfide reducing agents during protein purification and are thought to be more effective than dithiothreitol (DTT) and β-

mercaptoethanol. In a direct side-by-side comparison of disulfide reducing agents at biologically relevant pH 8.0 conditions, THPP demonstrated higher water-solubility, lower susceptibility to oxidation, and a higher ability to reduce a wide range of disulfide substrates into their corresponding thiols than TCEP and DTT.[7] THPP has also found uses in industrial wood pulp applications as an agent for bleaching and brightness stabilization in spruce wood pulps.[8]

THPP and TCEP concentrations are commonly maintained at ≤ 1.0 mM during protein purification and long-term storage of proteins. In a given enzyme assay, the final THPP and TCEP concentrations are typically much lower due to dilution effects upon adding the enzyme to the assay. However, THPP and TCEP are sometimes added to the assay solution for various reasons resulting in millimolar concentrations of the phosphine compound. Examples would include enzyme activity assays, biological binding experiments, and protein crystallization.

Here, we report evidence of a rapid chemical reaction between NAD^+ and tris(alkyl)phosphine compounds THPP and TCEP under conditions commonly used for kinetic and structural studies of enzymes. Stopped-flow kinetics show the reaction product with the main UV absorbance peak at 334 nm that is rapidly formed upon mixing NAD^+ and TCEP. One-dimensional and two-dimensional NMR demonstrate that the reaction product is a covalent adduct formed between the phosphorus of the phosphine compound and the C4 atom of the dihydronicotinamide ring of NAD^+. Altogether, our findings here serve as a cautionary note when using TCEP and THPP in biological assays and structural studies of $NAD(P)^+$-dependent oxidoreductases.

MATERIALS AND METHODS.

Materials and Reagents.

MilliQ-Ultra purified water was used for the preparation of all buffers and chemicals in the experiments. The following reagents were purchased from Millipore-Sigma: NaH_2PO_4, ε-amino-N-caproic acid, N-tosyl-L-phenylalanine chloromethyl ketone, bovine serum albumin, pyruvate, L-lactate dehydrogenase, NADPH, NADH, and NH_4F. The following reagents were commercially available from Fisher Scientific: NaOH, NaCl, 2-[4(2-hydroxyethyl)piperazin-1-yl]ethanesulfonic acid (HEPES), Na_2CO_3, $NaHCO_3$, and ethylenediamine tetraacetic acid (EDTA) disodium salt. Reagents β-octyl-D-glucopyranoside (β-OG) and L-proline (L-Pro) were commercially available from Combi-Blocks. Ethanol (190- or 200-proof) was purchased from Decon Labs. Tris(hydroxymethyl)aminomethane (Tris), glycine, isopropyl β-D-thiogalactopyranoside (IPTG), phenylmethylsulfonyl fluoride (PMSF), leupeptin hemisulfate, and NAD^+ were purchased from Gold Biotechnology. Imidazole and *o*-aminobenzaldehyde (*o*-AB) were purchased from Acros Organics. In terms of tris(alkyl)phosphine reducing agents used in this study, tris(3-hydroxypropyl)phosphine (THPP) was purchased from Strem Chemicals, and the hydrochloride salt of tris(2-carboxyethyl)phosphine (TCEP-HCl) was purchased from ThermoFisher Scientific-Pierce Biotech.

Stock solutions of NADH and NAD^+ were prepared in 10 mM Tris-HCl (pH 8) and stored at -80 °C. NADH and NAD^+ concentrations were determined spectrophotometrically at wavelengths 340 nm (ε_{340} = 6.22 x 10^3 $M^{-1}cm^{-1}$)[9] and 260 nm (ε_{260} = 17.37 x 10^3 $M^{-1}cm^{-1}$),[10] respectively. Each tris(alkyl)phosphine

reducing agent, THPP and TCEP, was prepared in 100 mM Tris-HCl (pH 7.5) buffer and stored at -80 °C.

Enzyme expression and PYCR reverse activity assays

HsPYCR1 protein was graciously provided by Dr. John J. Tanner's group after following an expression and purification procedure as described previously.[11] Similarly, HsPYCR2 protein was expressed from a pKA8H-PYCR2 construct in *E. coli* BL21 (DE3) pLysS competent cells (Novagen-EMD Millipore Sigma), cultured in TB liquid media and induced with 0.4 mM IPTG, followed by centrifugation for the harvesting of cell pellets. Next, the cell pellets were resuspended in NPI-5 cell lysis buffer (5 mM imidazole, 500 mM NaCl, 50 mM NaH_2PO_4, pH 7.5) also containing 500 µM THPP, 0.01% TritonX-100 detergent (Amresco), 0.01% Brij-35 polyoxyethylene detergent (Santa-Cruz Biotechnology), 10 mM βOG, and a mixture of five protease inhibitors. The cell suspension was then subjected to sonication and 4 °C centrifugation, to obtain supernatants of target protein solution for further purification by Ni-NTA Superflow (Qiagen) affinity column chromatography.

Time-course profiles of enzymatic reactions in the direction of NADH formation were performed at room temperature with NAD^+ substrate to monitor gain of absorbance at 340 nm over time under dark lab conditions with overhead lights off the entire time, using a modified protocol based on previous studies.[12,9,4,13] The ability of HsPYCR1 or 2 enzyme to catalyze the reverse reaction (L-Pro + NAD^+ → L-P5C + NADH) was tested in 0.1 M Tris-HCl (pH 7.5) buffer containing 0.01% (v/v) Brij-35 detergent, 30 mM $MgCl_2$, 5 mM L-proline (pH 7.5), and 0.5 mM NAD^+ (pH 8), and with or without tris(alkyl)phosphine

compound (1 mM TCEP (pH 7.5) or 1 mM THPP (pH 7.5)). The reaction components added into a 1 cm path length rectangular semi-micro, self-masking quartz spectrophotometer cuvette (Starna Cells) were cover wrapped in aluminum foil to protect from ambient light, placed atop a rocking platform for mild agitation at room temperature for 15 min, and then, the reaction was initiated by adding PYCR enzyme (0.06 µM final concentration) to achieve final assay volume of 600 µl. Followed by immediate parafilm covering the cuvette top, we shook it with inversion agitation to mix contents before placing the quartz cuvette into the spectrophotometer. Reactions were monitored at 340 nm for 30 min using a Varian Cary 50-UV/Vis spectrophotometer (Agilent Technologies) and Cary WinUV Kinetics Application software (version 5.0.0.999, Agilent Technologies).

NAD^+ reactions with tris(alkyl)phosphine reagents

Reactions of NAD^+ with THPP and TECP were initially performed at room temperature and dark conditions similar to the PYCR enzyme assays above, except no enzyme was added. Reaction components (0.5 mM NAD^+ and 5 mM L-proline) were combined with 0.1 M Tris-HCl buffer (pH 7.5, 0.01% (v/v) Brij-35 detergent, 30 mM $MgCl_2$) in the quartz cuvette for 15 min initial absorbance monitoring followed by the addition of THPP and TCEP (1 mM final concentration) and immediate parafilm covering the cuvette top for inversion agitation to mix contents before placing the quartz cuvette back into the spectrophotometer. The absorbance at 340 nm was monitored for 30 min total using a Varian Cary 50-UV/Vis spectrophotometer.

Stopped-flow absorbance spectrophotometry of the reactions between NAD^+

and THPP or TCEP were performed in the dark with different 100 mM (pH 7.5) reaction buffer compositions: HEPES, Tris-HCl, Na-Phosphate, and PBS. All stopped-flow experiments were conducted on a Hi-Tech KinetAsyst Scientific SF-61DX2 stopped-flow instrument equipped with a photodiode array detector and attached to nitrogen gas pressure, where all instrument settings and data collection was controlled and managed by Kinetic Studio software. The temperature of the mixing chamber for all experiments was maintained at room temperature (23 °C). NAD^+ (0.5 mM after mixing) was rapidly mixed with THPP or TCEP (25 mM after mixing) and the reaction was monitored in the stopped-flow by multiwavelength absorption in the range of 310-702 nm, Run Time = 1 s, Number of Scans = 100. In another set of experiments, NAD^+ was held fixed at 0.5 mM (after mixing) while increasing the concentrations of THPP and TCEP (5-150 mM, after mixing) in 100 mM HEPES (pH 7.5) buffer and monitoring the reaction by single-wavelength data collection at 334 nm. The average of three collected traces (n=3 technical replicates) was fit by non-linear least-squares regression to a single 3 parameter exponential rise equation using SigmaPlot 12.0 (version 12.0.0.182, Systat Software). The observed rate constant (k_{obs}) from the single 3 parameter exponential fitting was then plotted versus THPP and TCEP concentrations from which the apparent second-order forward association rate constant of the reaction (k_+^{app}) was determined as the slope of linear least-squares fit analysis. The apparent first-order reverse dissociation rate constant of the reaction (k_-^{app}) was determined by the intercept at the vertical axis. Under the pseudo-first-order conditions of the stopped-flow experiments ([THPP or TCEP] >> $[NAD^+]$), the following linear relationship holds $k_{obs} = (k_+^{app})$ [THPP or TCEP] +

(k_{-}^{app}) and the apparent association equilibrium constant is defined as K_a^{app} = (k_{+}^{app}/k_{-}^{app}).[14]

Nuclear Magnetic Resonance (NMR) characterization of the reaction product

For NMR measurements, the reaction of NAD^+ with THPP and TCEP was performed in 100 mM $NaHCO_3$-Na_2CO_3 (pH 7.5) buffer. Reaction component tubes were wrapped in aluminum foil to protect from ambient light. Samples were made by reacting NAD^+ (30.6 mM) or NADH (25.3 mM) with 400 mM of THPP or TCEP and kept on ice before NMR measurements. To assign the chemical structure to samples, we examined H_2O-D_2O (9:1 in volume) deuterated solvent-based preparations of each reaction component individually as well as in approximate (1:1) volume combinations of NAD^+ to THPP or TCEP in separate NMR glass capillary tubes to gather ^1H-, ^{13}C-, and ^{31}P-NMR data, as well as for the combination samples ^1H-^{31}P-HSQC-TOCSY, ^1H-^{31}P-HSQC, ^1H-^{13}C HMBC, and ^1H-^{13}C HSQC data. The NMR spectra were acquired on a Bruker Advance 600 MHz NMR spectrometer with a 5 mm TXI or 5 mm BBO probe. All spectra were acquired under dark lab conditions with overhead lights off the entire time and with the samples at 4 °C.

RESULTS

Evidence of (NAD^+—tris(alkyl)phosphine) association reaction

Evidence for a nonenzymatic reaction between NAD^+ and a tris(alkyl)phosphine reducing reagent was adduced by several observations. Initial assays of HsPYCR1 and 2 with L-Pro and NAD^+ generated no increase in absorbance at 340 nm over 30 min (Figure 5.1). We then included THPP and TCEP in the reaction buffer as was done in the U.S. Patented PYCR1 inhibition

assay protocol.[15] A rapid initial increase was observed with either TCEP or

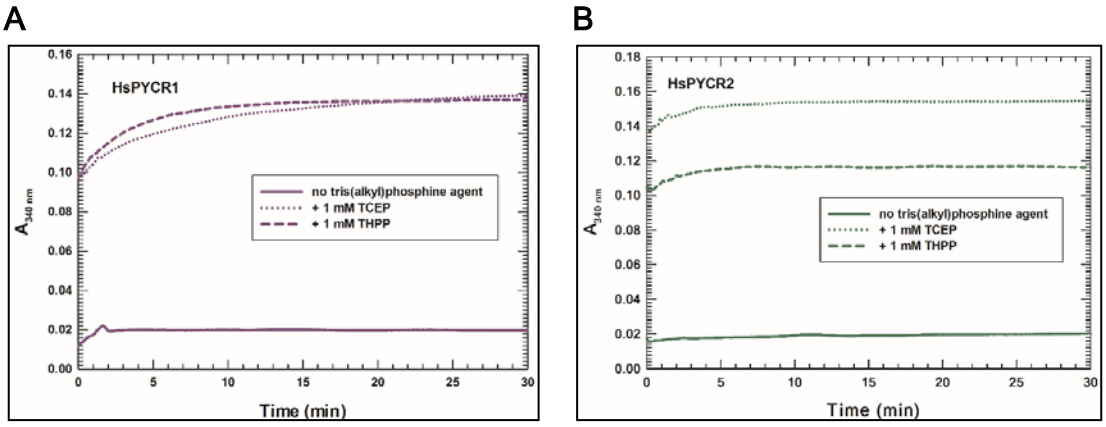

Figure 5.1. Test for PYCR activity in the reverse direction. PYCR activity in the reverse direction (L-Pro + NAD^+ → L-P5C + NADH) was assayed using 0.1 M Tris-HCl (pH 7.5) buffer with 0.01% (v/v) Brij-35 detergent, 30 mM $MgCl_2$, 5 mM L-proline, 0.5 mM NAD^+, with or without 1 mM TCEP or 1 mM THPP, and final enzyme concentration 0.6 µM (A) HsPYCR1 and (B) HsPYCR2. Progress of the reaction was monitored for 30 min by following the absorbance at 340 nm.

THPP, which then leveled off between 10-15 min and sustained absorbance intensity up to 30 min (Figure 5.1). Suspecting that we were observing a nonenzymatic reaction, we repeated the assay without PYCR and observed a sharp increase in absorbance at 340 nm upon adding THPP or TCEP after 15 min with again a sustained absorbance intensity up to 30 min (Figure 5.2).

Because the observed increase in absorbance occurred rapidly upon adding TCEP and THPP, we examined the reaction by stopped-flow absorbance spectrophotometry. Upon rapidly mixing both TCEP with NAD^+ in 100 mM HEPES (pH 7.5) reaction buffer, a peak with a maximum absorbance at 334 nm appeared within 200 ms (k_{obs} of 35.4 ± 0.4 s^{-1}) (Figure 5.3, A). The reaction was repeated using different reaction buffers with each exhibiting a similar k_{obs} value (30-35 s^{-1}) for the increase in absorbance, indicating the product formation is independent of the buffer composition.

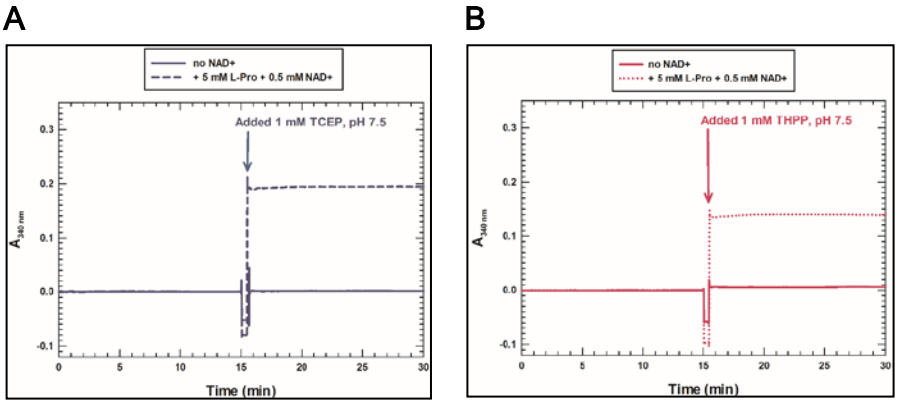

Figure 5.2. Absorbance changes upon mixing NAD⁺ with tris(alkyl)phosphine compounds. Nonenzymatic reactions with or without NAD⁺ (0.5 mM) were incubated in 0.1 M Tris-HCl (pH 7.5) buffer with 0.01% (v/v) Brij-35 detergent, 30 mM $MgCl_2$, and 5 mM L-proline. After 15 min, TCEP (A) and THPP (B) were added (1 mM final concentration) and the absorbance at 340 nm was recorded for an additional 15 min. All data points were normalized to a zero-absorbance baseline.

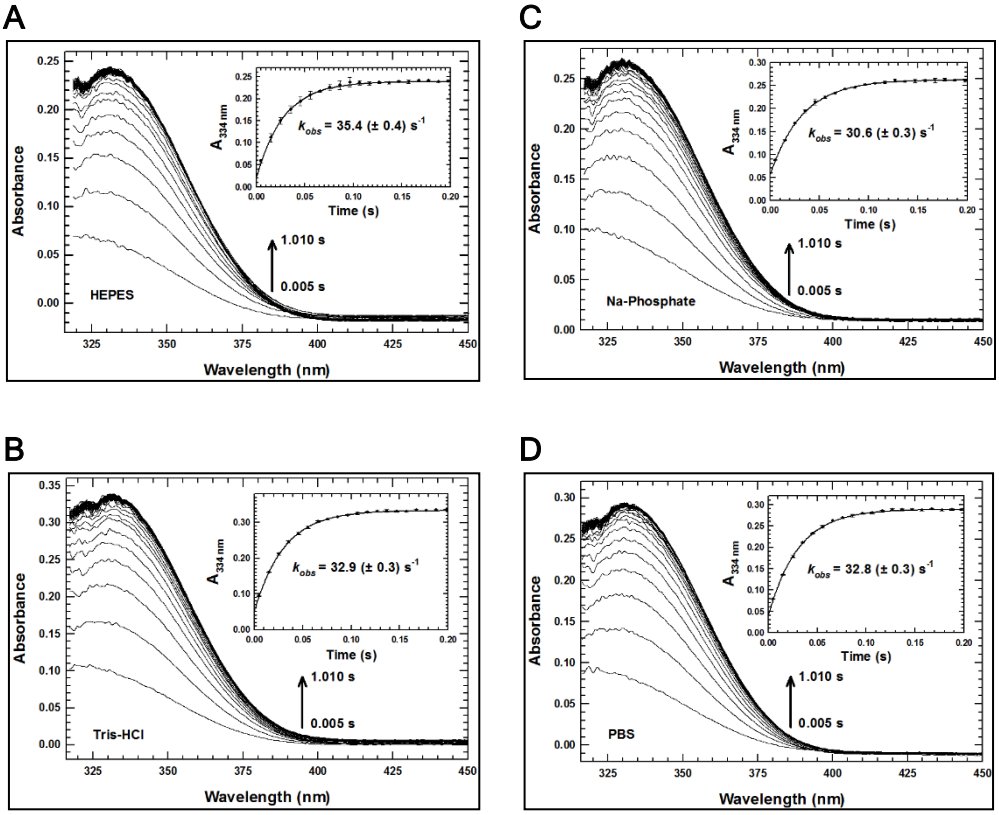

Figure 5.3. Stopped-flow absorbance spectrophotometry of mixing NAD⁺ and TCEP. NAD⁺ (0.5 mM after mixing) and TCEP (25 mM after mixing) were rapidly mixed and multiwavelength absorbance traces were recorded. Reactions were performed in 100 mM (pH 7.5) (A) HEPES, (B) Tris-HCl, (C) Na-Phosphate, and

(D) PBS reaction buffer. Plots of the absorbance increase at 334 nm over 0.20 s of time were fit to a single 3 parameter exponential equation as shown in the inset along with the observed rate constant (k_{obs}).

Rate constants for the observed increase in absorbance at 334 nm were then determined for TCEP and THPP using 100 mM HEPES (pH 7.5) reaction buffer.

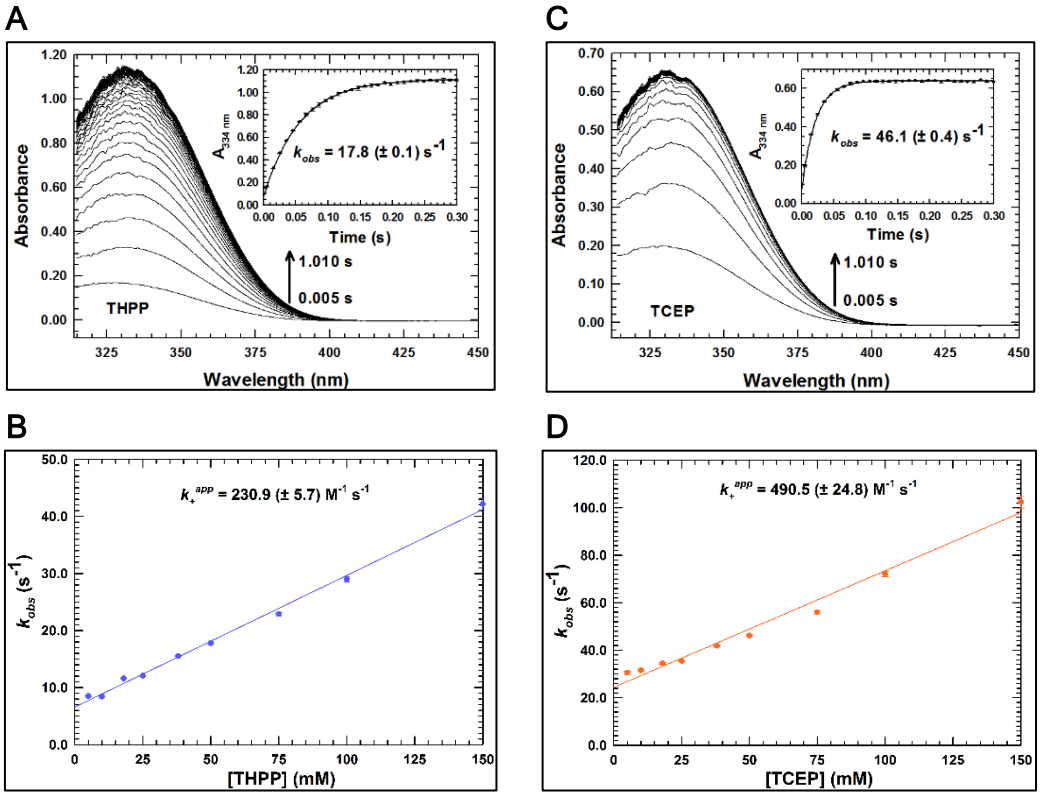

Figure 5.4. Stopped-flow kinetics of the (NAD$^+$—tris(alkyl)phosphine) association reaction. NAD$^+$ (0.5 mM) was rapidly mixed with 50 mM (A) THPP and (C) TCEP in 100 mM HEPES (pH 7.5) reaction buffer. Plots of the absorbance increase at 334 nm over 0.30 s of time were fit to a single 3 parameter exponential equation are shown in the inset along with the observed rate constant (k_{obs}). The dependence of the observed rate constant (k_{obs}) on THPP and TCEP concentration was then determined by holding NAD$^+$ concentration fixed (0.5 mM) and varying THPP and TCEP concentration (5-150 mM). Single wavelength data were collected at 334 nm and the corresponding k_{obs} values were determined from single 3 parameter exponential fits of the data. The apparent forward association (k_{+}^{app}) and reverse dissociation (k_{-}^{app}) rate constants were determined from the plot of k_{obs} versus (B) THPP and (D) TCEP. Data are plotted as (mean ± SD) of n=3 technical replicates and fit to a linear equation using SigmaPlot 12.0. All concentrations are specified after mixing.

Figure 5.4 shows the absorbance changes upon rapidly mixing 50 mM THPP (panel A) or 50 mM TCEP (panel B) with NAD^+. In another set of experiments, NAD^+ was then rapidly mixed with increasing concentrations of THPP or TCEP (5-150 mM). The observed rate constants (k_{obs}) versus THPP (panel C) and TCEP (panel D) concentration were then plotted to determine the apparent forward association (k_+^{app}) and reverse dissociation (k_-^{app}) rate constants. Table 5.1 summarizes the rate constants and shows that both the apparent forward (490.5 M^{-1} s^{-1}) and reverse (24.4 s^{-1}) rate constants with TCEP are faster than with THPP. The apparent equilibrium association constant (K_a^{app}), however, is slightly higher with THPP (35.1 M^{-1}).

Table 5.1. Pre-steady-state kinetic parameters for the reaction of NAD^+ and tris(alkyl)phosphine compounds

Kinetic parameter	THPP	TCEP
k_+^{app} (M^{-1} s^{-1})[a]	230.9 ± 5.7	490.5 ± 24.8
k_-^{app} (s^{-1})[b]	6.6 ± 0.4	24.4 ± 1.7
K_a^{app} (M^{-1})[c]	35.1 ± 2.3	20.1 ± 1.7

[a](Value ± Std error) is reported for the apparent forward rate constant determined as the slope of the plotted data fit to a linear least-squares equation using SigmaPlot 12.0 (version 12.0.0.182, Systat Software) with data plotted as (mean ± SD) of n=3 technical replicates.
[b](Value ± Std error) is reported for the apparent reverse rate constant determined as the vertical axis intercept of the plotted data.
[c]Apparent equilibrium association constant determined from the calculation of $K_a^{app} = (k_+^{app}/k_-^{app})$.

Characterization of the reaction product

L-lactate dehydrogenase and pyruvate were initially added to the reaction product to test whether NADH was formed. However, no decrease in absorbance (330-340 nm) was observed indicating that the product was not usable by L-

lactate dehydrogenase. We also did not find evidence for NADH by mass spectrometry analysis of the reaction product.

NMR was then used to characterize and identify the product. Initial NMR experiments included one-dimensional (^{1}H and ^{31}P) and two-dimensional (^{1}H-^{31}P HSQC, ^{1}H-^{31}P HSQC-TOCSY) analyses. The chemical shift data from these experiments indicated the tris(alkyl)phosphine compound's phosphorus atom was interacting with the C4 position of the dihydronicotinamide ring of NAD^{+}. Additionally, two-dimensional NMR data as shown in Fig. 5.5 with corresponding spectral data provided in Table 5.2, indicated the reaction was reversible as the ^{1}H-^{31}P HSQC-TOCSY showed ^{31}P correlations to reaction product protons and ^{31}P correlations to NAD^{+} protons. With the ^{1}H-^{31}P HSQC-TOCSY, NAD^{+} proton correlations could only be observed if the phosphine compound was associating and dissociating with the dihydronicotinamide ring during the TOCSY spinlock, indicating reaction reversibility. Lastly, these initial experiments indicated the reaction yielded two products with different stereochemistry, likely with the phosphorus above or below the dihydronicotinamide ring, in a roughly 1 to 0.6 ratio.

As evident from both one-dimensional (^{31}P) and two-dimensional (^{1}H-^{31}P HSQC, ^{1}H-^{31}P HSQC-TOCSY) analyses, the latter of which is shown in Fig. 5.5 and Table 5.2, there were two sets of phosphorus species observed in the NAD^{+} and THPP reaction mixture. The phosphorus species circa 34.4 ppm were interacting with the dihydronicotinamide ring. The phosphorus species circa -13.2 ppm were interacting with one of the ribose rings. Additionally, two-dimensional (^{1}H-^{13}C HMBC) analysis of NAD^{+} alone and NADH alone with their spectral data

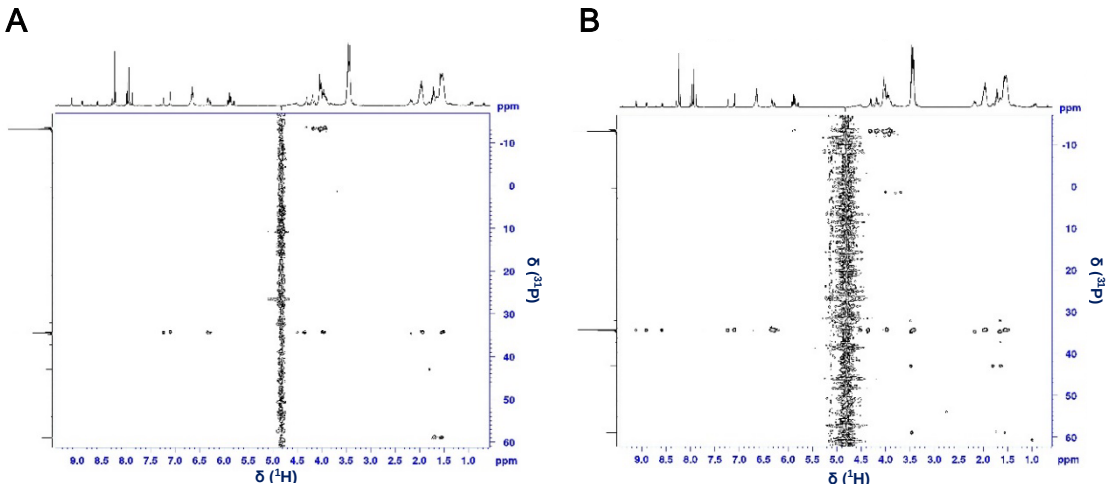

Figure 5.5. Two-dimensional ^{1}H-^{31}P NMR spectra of the NAD^{+} and THPP reaction mixture. Shown here is the (A) ^{1}H-^{31}P HSQC spectrum and (B) ^{1}H-^{31}P HSQC-TOCSY spectrum. Both spectra were acquired with a J-coupling constant of 11 Hz, and the latter spectrum with a TOCSY mixing time of 80 ms. The assignments are summarized in Table 2 to support the chemical structures of the reaction product and NAD^{+} alone as shown in Fig. 5.6, D.

summarized in Tables 5.3 and 5.4, respectively, support structural assignments of these reference compound structures shown in Fig. 5.6, A and B.

Table 5.2. Chemical shifts from ^{1}H-^{31}P NMR correlation experiment† of NAD^{+} and THPP reaction mixture

Label	δ (^{1}H, ppm)‡	δ (^{1}H-^{31}P HSQC, ppm)	δ (^{1}H-^{31}P HSQC-TOCSY, ppm)
1	3.96 (^{1}H), minor 4.35	34.3, minor 34.4	34.3, minor 34.4
2	1.96 (m), minor 1.98	34.3	34.3
3	1.54 (m)	34.3	34.3
4	3.44 (m)		34.3
5			
6			
7	7.10 (d, ^{1}H, J = 1.8 Hz), minor 7.23 (d, ^{1}H, J = 1.8 Hz)	34.3, minor 34.4	34.3, minor 34.4
8	6.33 (at, ^{1}H, J = 6.3 Hz), minor 6.28 (at, ^{1}H J = 6.3)	34.3, minor 34.4	34.3, minor 34.4
9	4.51		
10	4.67 (broad s), minor 4.69		
b	8.91 (d, J = 6.3 Hz)		34.3
d	8.59 (d, J = 8.4 Hz)		34.3
g	9.11 (s)		34.3

†Chemical shifts were determined from the HSQC and HSQC-TOCSY experiments shown in Fig. 5.5 and correspond to site labels shown in Fig. 5.6, D.
‡Listed next to each ^{1}H-NMR chemical shift value is (multiplicity designation [s, singlet; d, doublet; m, multiplet; etc.], J-coupling constant).

Table 5.3. Chemical shifts from ^{1}H-^{13}C NMR correlation experiment† of NAD$^+$

Label	δ (^{1}H, ppm)‡	δ (^{13}C, ppm)	HMBC
a	5.85 (d, ^{1}H, J = 5.6 Hz)	98	b, g
b	8.9 (d, ^{1}H, J = 6.6 Hz)	140.3	a, c, d, g
c	7.93 (at, ^{1}H, J = 6.6 Hz)	126.6	b, e
d	8.57 (d, ^{1}H, J = 8.5 Hz)	143.6	b, f, g
e		131.6	
f		163.2	
g	9.1 (s, ^{1}H)	138.0	a, b, d, e, f

†Chemical shifts were determined from the HMBC experiment and correspond to site labels shown in Fig. 5.6, A.
‡Listed next to each ^{1}H-NMR chemical shift value is (multiplicity designation [s, singlet; d, doublet; etc.], J-coupling constant).

Table 5.4. Chemical shifts from ^{1}H-^{13}C NMR correlation experiment† of NADH

Label	δ (^{1}H, ppm)‡	δ (^{13}C, ppm)	HMBC
A	4.55 (d, ^{1}H, J = 7.1 Hz)	93.1	B, G
B	5.73 (d, ^{1}H, J = 8.4 Hz)	121.4	A, C, D, G
C	4.51 (^{1}H)	103.4	B, E
D	2.35 (dd, ^{1}H, J = 3.4, 18.8 Hz), 2.49 (d, ^{1}H, J = 18.4 Hz)	19.9	B, C, E, G
E		97.5	
F		170.7	
G	6.68 (s, ^{1}H)	136.7	A, B, D, E, F

†Chemical shifts were determined from the HMBC experiment and correspond to site labels shown in Fig. 5.6, B.
‡Listed next to each ^{1}H-NMR chemical shift value is (multiplicity designation [s, singlet; d, doublet; dd, doublet of doublets], J-coupling constant).

A

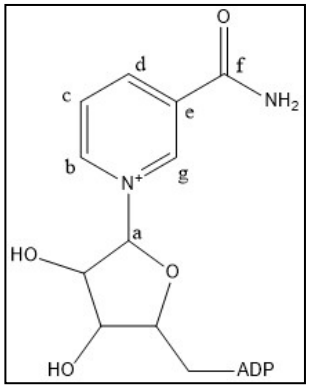

C

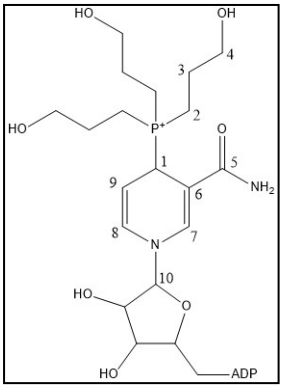

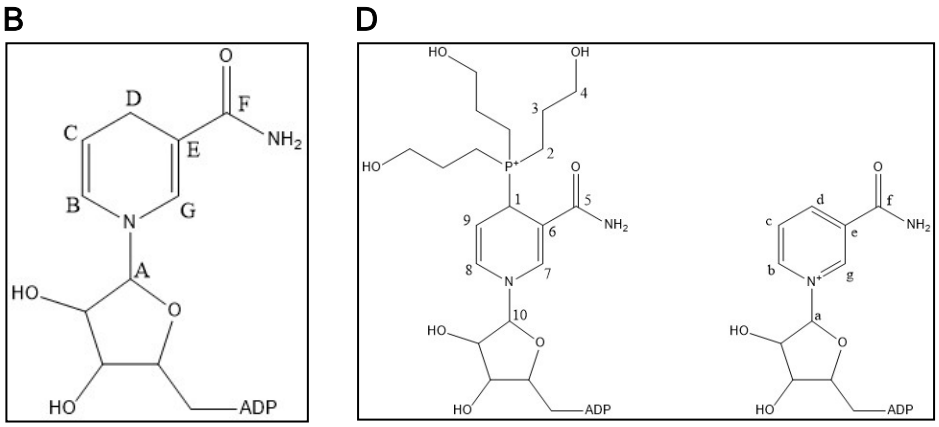

Figure 5.6. Chemical structures of compounds based on the assignment of NMR spectral data. Assignments of (A) NAD^+ structure, (B) NADH structure, (C) NAD^+ and THPP reaction mixture structure, and (D) structures of NAD^+ and THPP reaction mixture (left) and NAD^+ alone (right) have alphanumeric site labels corresponding to chemical shift data presented in Tables 5.2-5.5.

Further experiments were conducted, on an aged sample of NAD^+ and THPP, to complete the structural assignment. These experiments included one dimensional (^{13}C) and two dimensional (^1H-^1H COSY, ^1H-^1H TOCSY, ^1H-^{13}C HSQC, ^1H-^{13}C HMBC) analyses as shown in Fig. 5.7, the last of which has its spectral data summarized in Table 5.5. Also, the reaction product of NAD^+ and

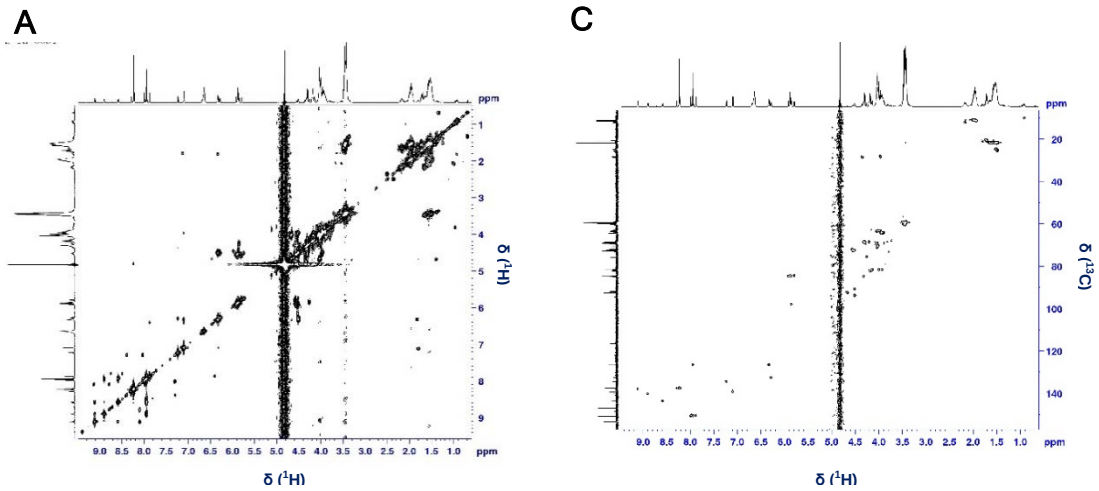

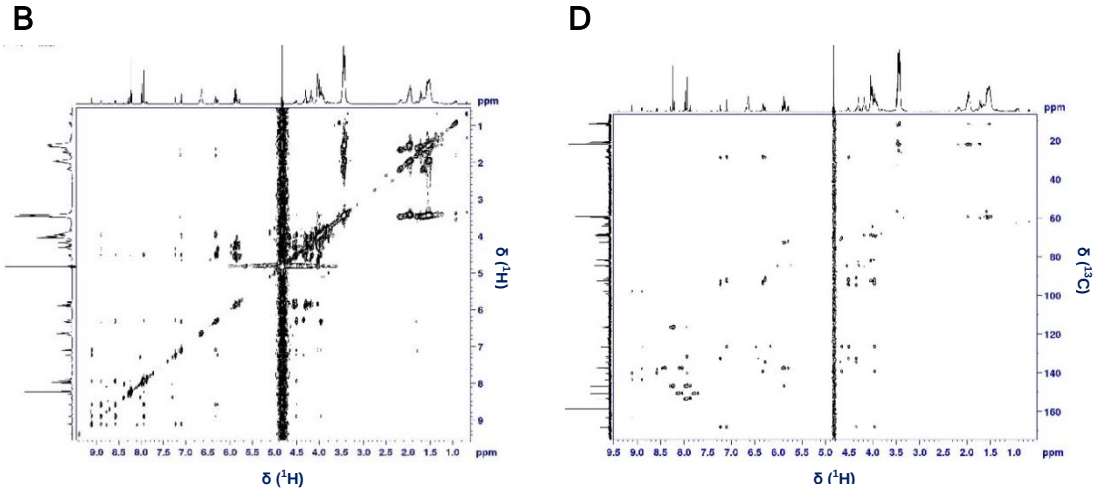

Figure 5.7. Two-dimensional NMR spectra of NAD⁺ and THPP reaction mixture. Shown here is the (A) ^{1}H-^{1}H COSY spectrum, (B) ^{1}H-^{1}H TOCSY spectrum, (C) ^{1}H-^{13}C HSQC spectrum, and (D) ^{1}H-^{13}C HMBC spectrum. The assignments of panel D are summarized in Table 5.5 to support the chemical structure of the reaction product as shown in Fig. 5.6, C.

Table 5.5. Chemical shifts from ^{1}H-^{13}C NMR correlation experiment† of NAD⁺ and THPP reaction mixture

Label	δ (^{1}H, ppm)‡	δ (^{13}C, ppm)	HMBC
1	3.96 (^{1}H), minor 4.35	28.4 (J-CP = 47 Hz), minor 28.6 (J-CP = 48 Hz)	5, 6, 7, 8, 9
2	1.96 (m), minor 1.98	11.3 (J-CP = 44 Hz), minor 11.1 (J-CP = 45 Hz)	3, 4
3	1.54 (m)	21.6 (J-CP = 4 Hz), minor 21.8 (J-CP = 4 Hz)	2, 4
4	3.44 (m)	59.3	2, 3
5		168.2	
6		94.6	
7	7.10 (d, ^{1}H, J = 1.8 Hz), minor 7.23 (d, ^{1}H, J = 1.8 Hz)	139.3, minor 134.5	1, 5, 6, 8, 10
8	6.33 (at, ^{1}H, J = 6.3 Hz), minor 6.28 (at, ^{1}H J = 6.3)	126.6, minor 132.6	1, 7, 9, 10
9	4.51	93.9	1, 8
10	4.67 (broad s), minor 4.69	92.6, minor 92.3	7, 8

†Chemical shifts were determined from the HMBC experiment shown in Fig. 5.7, D and correspond to site labels shown in Fig. 5.6, C.
‡Listed next to each ^{1}H-NMR chemical shift value is (multiplicity designation [s, singlet; d, doublet; m, multiplet; etc.], J-coupling constant).

THPP was very similar to that of NAD⁺ and TCEP as determined by overlaying or stacking the one-dimensional proton spectra as shown in Fig. 5.8.

DISCUSSION

To our knowledge, this is the first NMR characterization of a covalent adduct between NAD^+ and TCEP or THPP. The reaction occurs at biologically relevant concentrations of NAD^+ (0.5 mM) with TCEP and THPP concentrations (1 mM) typically used in experimental conditions. Stopped-flow kinetics indicate the reaction is reversible and occurs on a timescale comparable to that of TCEP reduction of disulfide bonds in DTT (43 $M^{-1}s^{-1}$), peptide substrates containing a CXXC motif (650 $M^{-1}s^{-1}$), and oxidized cysteines in proteins (1.5 - 813 $M^{-1}s^{-1}$).[16,17] We did not detect NADH formation, instead, NMR showed conclusive evidence for a covalent adduct of the phosphorus at the C4 position of the dihydronicotinamide ring. The reaction likely proceeds through a nucleophilic attack of the phosphine's phosphorus atom at the C4 position of the dihydronicotinamide group of NAD^+ similar to that of a tertiary phosphine attacking an alkyl halide to form a phosphonium ion.

The dihydronicotinamide ring of NAD^+ has electrophilic character and thereby

A

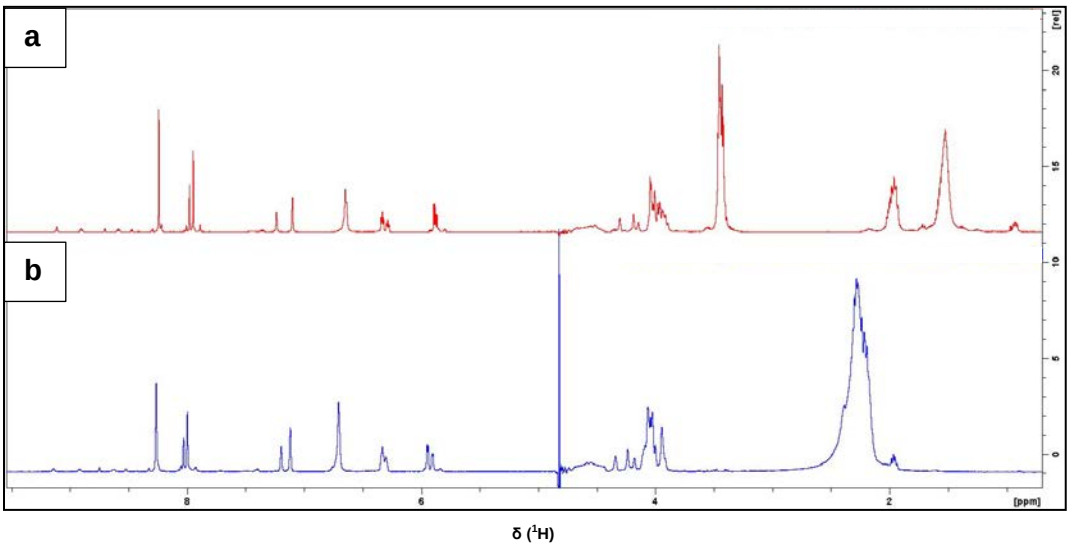

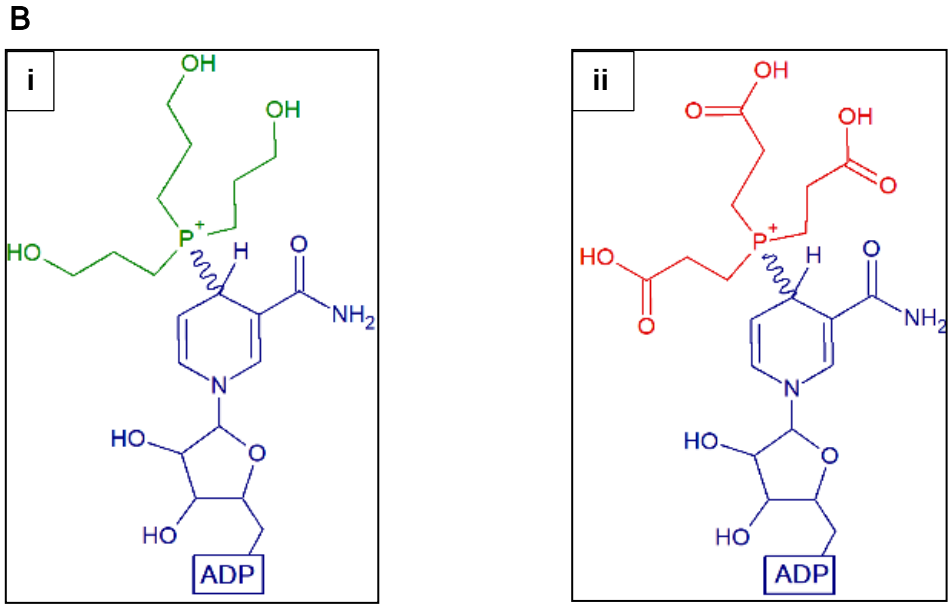

Figure 5.8. Covalent Adduct Reaction Product NMR spectra and resolved chemical structures. (A) ^{1}H-NMR spectra stacked as (a) NAD^{+} with THPP and (b) NAD^{+} with TCEP. (B) Chemical structures of resolved covalent adduct product from the reaction of (i) NAD^{+} with THPP and (ii) NAD^{+} with TCEP.

is susceptible to modifications by nucleophilic species. More fundamentally, NAD(P)$^{+}$ and NAD(P)H differ from other coenzymes such as thiamine pyrophosphate, biotin, and pyridoxal phosphate, which return to their original forms upon completion of their catalytic cycles, whereas the pyridine dinucleotides appear modified with stereospecific hydrogen exchange at the C4 position of the dihydronicotinamide ring, thus earning NAD(P)$^{+}$ and NAD(P)H the title of cosubstrate.[18] Of biological relevance is that various sulfhydryl compounds can form adducts at the C4 position of the dihydronicotinamide ring.[19] Besides consistent UV absorption spectra, the infrared absorption spectra of covalent adduct compounds formed from the reaction of thiols (including benzyl mercaptan, 2-mercaptothiazole, β-phenylethyl mercaptan, ethyl mercaptan, thiocyanate ion, and thiophenol) with 1-substituted NAD^{+} demonstrate

characteristic peak absorption at ~1560 cm^{-1}, particularly due to a vinylogous amide group that often occurs in 1,4-dihydronicotinamide molecules.[19] Sulfhydryl compounds such as cysteine and glutathione can add to the dihydronicotinamide ring of NAD^+ to form NAD^+-mercaptan addition complexes with UV absorbance maxima at 350 nm.[20] It is of interest to note that the apparent association equilibrium constants for cysteine (2.4×10^{-9} M^{-1}) and glutathione (1.6×10^{-9} M^{-1})[20] with NAD^+ are dramatically 10^9- to 10^{10}-fold smaller in magnitude than the K_a^{app} values for tris(alkyl)phosphine compounds with NAD^+ observed here. Another example of observed NAD^+ addition reaction with a nucleophilic species involves the bacterial NAD^+-dependent enzyme urocanase, which forms a chromophore between competitive inhibitor imidazole-propionate and NAD^+ with an observed UV absorbance peak at 335 nm.[21] In this case, NMR evidence showed that the chromophore generated from this urocanase reaction was not NADH, but rather was a reversible complex of the inhibitor's imidazole nitrogen forming a covalent adduct with the C4 position of the dihydronicotinamide ring of NAD^+.[21] Thus, the UV absorbance peak of 334 nm observed here for the covalent NAD^+—tris(alkyl)phosphine adducts, is similar to that previously reported for various covalent NAD^+ adduct species.

We could not find any previous reports of chemical reactivity between NAD^+ and phosphine compounds. In 2017, however, Mayclin et al. from the Seattle Structural Genomics Center for Infectious Disease resolved a 1.45 Å X-ray crystal structure of the $NADP^+$ cofactor-bound complex of bacterial short-chain dehydrogenase/reductase (SDR) from *Burkholderia ambifaria* (Figure 5.9).[22] This structure was determined from a crystal grown in the presence of 5 mM $NADP^+$

and 1 mM TCEP (PDB Code: 5VPS). Whereas $NADP^+$ was explicitly added to the crystallization experiment to obtain a structure of the functional enzyme, TCEP was included as an innocuous component of the enzyme stock solution buffer. The electron density maps clearly showed $NADP^+$ bound to the Rao-Rossmann fold in the expected conformation (Figure 5.9, a). Unexpectedly, strong electron density indicated that the C4 atom of the dihydronicotinamide ring of NADPH had been covalently linked to the phosphorus atom of (Figure 5.9, b). The electron

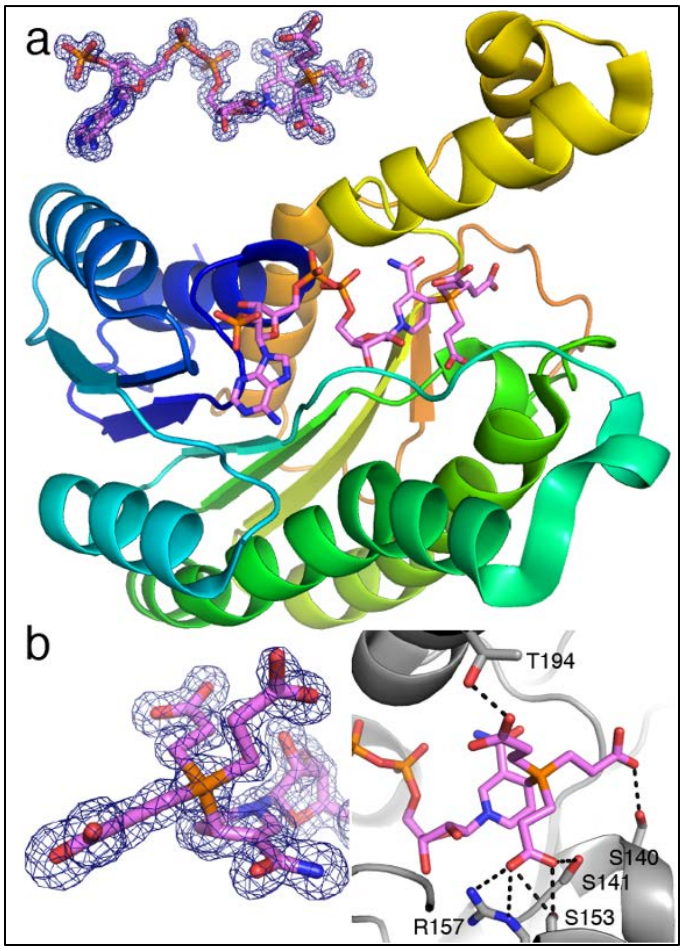

Figure 5.9. Structure of *Burkholderia ambifaria* SDR with a $NADP^+$–TCEP adduct in the active site. (a) Ribbon cartoon model of the SDR protein with the adduct in pink sticks. The inset shows electron density for the adduct (polder omit, 3.0σ). (b) Closeup views of the adduct showing electron density for the P-C4 bond (left) and interactions with the carboxyethyl groups of TCEP (right). The X-ray crystal structure of SDR soaked with 5 mM $NADP^+$ and 1 mM TCEP was graciously provided by Dr. Stephen J. Mayclin and Dr. Thomas E. Edwards.

density is consistent with the structure of the adduct determined from solution NMR. Thus, TCEP and $NADP^+$ are also capable of forming a covalent adduct in an oxidoreductase active site. Whether the kinetics of the reaction is similar to that in solution remains unknown. Because TCEP and $NAD(P)^+$ can form a complex in solution or in an enzyme active site, it raises the question as to how many structures of $NAD(P)^+$-dependent oxidoreductases have been impacted by including TCEP or THPP in the crystallization milieu. Although the $NADP^+$-TCEP adduct was captured in SDR, the same adduct could potentially cause disorder of the $NAD(P)^+$ cofactor in other enzymes making it difficult to identify $NAD(P)^+$-binding interactions.

In addition to unintentional interference with crystallization and structural studies, TCEP and THPP are also likely to cause problems with enzyme assays and binding studies. As we observed, adding TCEP and THPP to $NAD(P)^+$-dependent assays would generate a rapid absorbance increase around 340 nm that, without proper controls, could be misinterpreted as enzyme activity. This would particularly be a problem with high-throughput assays that use only endpoint measurements. With respect to binding studies, the addition of tris(alkyl)phosphine compounds would potentially lead to lower concentrations of free $NAD(P)^+$, resulting in anomalous errors in the determined binding constant. Also, the data could be convoluted by unknowingly having two species present, $NAD(P)^+$ and the $NAD(P)^+$—tris(alkyl)phosphine covalent adduct. Methods that measure changes in heat to quantify bimolecular binding events, such as isothermal titration calorimetry, would have additional complications due to heat contributions by $NAD(P)^+$ reacting with TCEP or THPP during the titration.[23]

We characterized the chemical reaction kinetics of (NAD^+—tris(alkyl)phosphine) association reactions and identified the chemical structure of the reaction product molecule through NMR assignments. Evidence from stopped-flow spectrophotometry and multidimensional NMR indicate that the species formed with a UV absorbance maximum at 334 nm is a reversible covalent adduct between the tris(alkyl)phosphine compound's phosphorus atom and the C4 position of the dihydronicotinamide group of NAD^+. Side-by-side comparison of TCEP and THPP shows the reaction kinetics with NAD^+ are faster with TCEP whereas THPP exhibits a 1.7-fold higher apparent equilibrium association constant for the NAD^+—tris(alkyl)phosphine covalent adduct. In conclusion, the implications of our data concerning the (NAD^+—tris(alkyl)phosphine) association reaction warrant caution be taken when using TCEP or THPP with $NAD(P)^+$-dependent enzymes.

REFERENCES

[1] Liu, W., Hancock, C. N., Fischer, J. W., Harman, M., and Phang, J. M. (2015) Proline biosynthesis augments tumor cell growth and aerobic glycolysis: involvement of pyridine nucleotides, *Sci Rep 5*, 17206.

[2] De Ingeniis, J., Ratnikov, B., Richardson, A. D., Scott, D. A., Aza-Blanc, P., De, S. K., Kazanov, M., Pellecchia, M., Ronai, Z. e., Osterman, A. L., and Smith, J. W. (2012) Functional Specialization in Proline Biosynthesis of Melanoma, *PLoS ONE 7*, e45190 EP -.

[3] Phang, J. M. (2019) Proline Metabolism in Cell Regulation and Cancer Biology: Recent Advances and Hypotheses, *Antioxid Redox Signal 30*, 635-649.

[4] Nocek, B., Chang, C., Li, H., Lezondra, L., Holzle, D., Collart, F., and Joachimiak, A. (2005) Crystal structures of delta1-pyrroline-5-carboxylate reductase from human pathogens Neisseria meningitides and Streptococcus pyogenes, *J Mol Biol 354*, 91-106.

[5] Meng, Z., Lou, Z., Liu, Z., Li, M., Zhao, X., Bartlam, M., and Rao, Z. (2006) Crystal Structure of Human Pyrroline-5-carboxylate Reductase, *Journal of Molecular Biology 359*, 1364-1377.

[6] Laliberté, G., and Hellebust, J. A. (1989) Pyrroline-5-Carboxylate Reductase in Chlorella autotrophica and Chlorella saccharophila in Relation to Osmoregulation, *Plant Physiol 91*, 917-923.

[7] McNulty, J., Krishnamoorthy, V., Amoroso, D., and Moser, M. (2015) Tris(3-hydroxypropyl)phosphine (THPP): A mild, air-stable reagent for the rapid, reductive cleavage of small-molecule disulfides, *Bioorg Med Chem Lett 25*, 4114-4117.

[8] Moiseev, D. V., James, B. R., and Hu, T. Q. (2012) Characterization of secondary and primary (hydroxymethyl) phosphines and their oxidation products: Synergism in pulp-bleaching, *Phosphorus, Sulfur, and Silicon and the Related Elements 187*, 433-447.

[9] Ruszkowski, M., Nocek, B., Forlani, G., and Dauter, Z. (2015) The structure of Medicago truncatula δ(1)-pyrroline-5-carboxylate reductase provides new insights into regulation of proline biosynthesis in plants, *Front Plant Sci 6*, 869.

[10] Haid, E., Lehmann, P., and Ziegenhorn, J. (1975) Molar absorptivities of beta-NADH and beta-NAD at 260 nm, *Clin Chem 21*, 884-887.

[11] Christensen, E. M., Patel, S. M., Korasick, D. A., Campbell, A. C., Krause, K. L., Becker, D. F., and Tanner, J. J. (2017) Resolving the cofactor-binding site in the proline biosynthetic enzyme human pyrroline-5-carboxylate reductase 1, *Journal of Biological Chemistry 292*, 7233-7243.

[12] Merrill, M. J., Yeh, G. C., and Phang, J. M. (1989) Purified human erythrocyte pyrroline-5-carboxylate reductase. Preferential oxidation of NADPH, *Journal of Biological Chemistry 264*, 9352-9358.

[13] Szoke, A., Miao, G. H., Hong, Z., and Verma, D. P. (1992) Subcellular location of delta-pyrroline-5-carboxylate reductase in root/nodule and leaf of soybean, *Plant Physiol 99*, 1642-1649.

[14] Pollard, T. D., and De La Cruz, E. M. (2013) Take advantage of time in your experiments: a guide to simple, informative kinetics assays, *Mol Biol Cell 24*, 1103-1110.

[15] Grünewald, S., Steckel, M., Husemann, M., Meyer, H., Han, W., and Ding, Z. (2019) Inhibitors and antagonists of human pycr1, Google Patents.

[16] Cline, D. J., Redding, S. E., Brohawn, S. G., Psathas, J. N., Schneider, J. P., and Thorpe, C. (2004) New water-soluble phosphines as reductants of

peptide and protein disulfide bonds: reactivity and membrane permeability, *Biochemistry 43*, 15195-15203.

[17] Parsons, Z. D., and Gates, K. S. (2013) Thiol-dependent recovery of catalytic activity from oxidized protein tyrosine phosphatases, *Biochemistry 52*, 6412-6423.

[18] You, K. S. (1985) Stereospecificity for nicotinamide nucleotides in enzymatic and chemical hydride transfer reactions, *CRC Crit Rev Biochem 17*, 313-451.

[19] Dittmer, D., and Kolyer, J. (1963) Addition Compounds of Thiols and 1-Substituted Nicotinamides1, 2, *The Journal of Organic Chemistry 28*, 1720-1722.

[20] VAN EYS, J., and KAPLAN, N. O. (1957) The addition of sulfhydryl compounds to diphosphopyridine nucleotide and its analogues, *J Biol Chem 228*, 305-314.

[21] Matherly, L. H., DeBrosse, C. W., and Phillips, A. T. (1982) A covalent nicotinamide adenine dinucleotide intermediate in the urocanase reaction, *Biochemistry 21*, 2789-2794.

[22] Mayclin, S. J., Dranow, D. M., Lorimer, D., Edwards, T. E., and Disease, S. S. G. C. f. I. (2017, doi: 10.2210/pdb5VPS/pdb.) PDB ID: 5VPS. Crystal structure of an SDR from Burkholderia ambifaria in complex with NADPH with a TCEP adduct.

[23] Di Trani, J. M., Moitessier, N., and Mittermaier, A. K. (2018) Complete Kinetic Characterization of Enzyme Inhibition in a Single Isothermal Titration Calorimetric Experiment, *Anal Chem 90*, 8430-8435.

Chapter 6

Major Conclusions and Future Directions

MAJOR CONCLUSIONS

Pyrroline-5-carboxylate reductases have been identified as important housekeeping enzymes of L-proline biosynthesis, which generate the unique imino acid L-proline that serves as an instrumental structural component of proteins and participates in stress protection and redox homeostasis of cells across all three domains of life (eukaryota, bacteria, and archaea).[1,2,3,4] In chapter two, we describe the circa 1.9 Å high resolution X-ray crystal structures of the binary complexes of HsPYCR1 with NADPH or L-Pro bound ligands that were obtained by our collaborators. These structures unequivocally identify the NADPH-binding site being located in the N-terminal Rao-Rossmann fold domain of HsPYCR1. A high-resolution X-ray crystal structure of a ternary complex of HsPYCR1 containing NADPH and an L-P5C/L-Pro analog, L-THFA, provides a mechanistic model of the Michaelis complex formed during hydride transfer. Functional analysis of a highly conserved active site Thr238 by site-directed mutagenesis reveals substitution with Ala (T238A) results in a 10-fold diminution in catalytic efficiency with varied concentrations of L-P5C relative to the wild-type enzyme. These data suggest that the loss of Thr238 as a potential proton donor in the enzyme active site strongly hinders catalytic activity, perhaps by loss of a hydrogen bonding interaction with the imine nitrogen of the L-P5C substrate.

Based upon structural homology with human PYCR1, chapter three focuses on the functional and structural consequences in wild-type HsPYCR2 enzyme of two mutant variants, Arg119Cys and Arg251Cys, that were previously identified

in patients with microcephaly and hypomyelination.[5] Arg119 and Arg251 are predicted to be important for the catalytic activity and structural stability of HsPYCR2. Henri-Michaelis-Menten kinetic analysis shows a 164-fold loss in catalytic efficiency for the Arg119Cys mutant, with varied concentrations of L-P5C substrate and fixed concentration of NADH cofactor, relative to the wild-type enzyme. The dramatic loss in activity could be due to mutation of Arg119 near the posterior wall of the enzyme's active site leading to disrupted conformation flexibility of HsPYCR2 near the cofactor substrate binding site, thus leading to decreased kinetics of cofactor substrate entrance and egress.[6] The Arg251Cys mutation has a profound effect on the thermostability and secondary structure of HsPYCR2 as determined by fluorescence-based thermal shift assays and circular dichroism, respectively.

The binding order of L-P5C and NAD(P)H to HsPYCR1 and HsPYCR2 enzymes was evaluated by product(s) inhibition studies using L-Pro, $NADP^+$, or NAD^+.[7] Collective analysis of Henri-Michaelis-Menten kinetic data and Hanes-Woolf plots of linear regressions indicate $NADP^+$ and NAD^+ are mixed noncompetitive inhibitors[8] of HsPYCR1 and 2 against NADPH and NADH substrates, respectively. L-Proline is a competitive inhibitor[8] of HsPCYR1 and 2 with respect to L-P5C substrate. Taken together, these modes of product inhibition support a proposed sequential-ordered binding mechanism for HsPYCR1 and HsPYCR2 enzymes.[7] Interestingly, serum levels of L-proline in healthy adult humans is reported to range from 125-633 μM with mean levels around 270 μM.[9,10] The apparent competitive inhibition constants for both HsPYCR1 and HsPYCR2 determined with L-proline (K_{IC}^{app} = 2.61 ± 0.25 mM and

145 ± 8 μM, respectively) highlight HsPYCR2's greater sensitivity to physiological L-proline concentrations, suggesting that it is susceptible to product feedback inhibition by L-proline. In terms of NAD^+, Yang et al.'s (2007) study estimated [NAD^+] in mitochondria of HEK293 cells is 245.6 μM using MALDI-MS, which corresponds to 2053 pmol NAD^+/mg mitochondrial protein.[11] NADH may be lower than NAD^+ levels (e.g., physiologic NAD^+/NADH ratio ~0.1-10 in mammalian cells)[12], and intracellular concentrations of $NADP^+$ and NADPH are even lower than their non-phosphorylated forms wherein the $NADP^+$ pool is predominantly in the reduced state.[13] Thus, the apparent competitive inhibition constants determined here for both HsPYCR1 and HsPYCR2 with $NADP^+$ and NAD^+, respectively (K_{IC}^{app} = 8.28 ± 1.36 mM and 792 ± 248 μM) as well as the corresponding apparent uncompetitive inhibition constants (K_{IU}^{app} = 3.92 ± 0.64 mM and 326 ± 102 μM) highlight again that HsPYCR2 is more susceptible to product feedback inhibition by NAD^+ than HsPCYR1. The physiologic levels of $NADP^+$ are not high enough to effectively inhibit HsPYCR1.

In chapter four, we performed in vitro experiments probing human PYCR-mediated reverse direction reactions, which involve the reduction of $NAD(P)^+$ into NAD(P)H using L-Pro, L-T4C, or DL-T2C as the reducing substrate with human PYCRs at biologically relevant pH 7.5. From these studies, we observed no substantial reverse activity of HsPYCR1 or HsPYCR2 with L-Pro or DL-T2C, however, substantial activity was observed with L-T4C. Upon further analysis of Henri-Michaelis-Menten saturation kinetics, we report that HsPYCR2 exhibits an apparent catalytic efficiency (136 M^{-1} s^{-1}) with varied concentrations of L-T4C that is nearly 10-fold higher than that of HsPYCR1 (13.7 M^{-1} s^{-1}) with varied

concentrations of L-T4C. Ligand inhibition kinetics evidence of L-Pro as a competitive inhibitor (K_{IC}^{app} = 15.7 mM) of HsPYCR1 with respect to L-T4C substrate. This data along with the 2.30 Å X-ray crystal structure of a HsPYCR1—L-T4C complex highly suggests that L-T4C binds at the same active site region as L-Pro in the enzyme. Taken together, this experimental evidence assigns a novel enzyme function to human PYCRs. We propose PYCRs be given the new name L-thiazolidine-4-and-L-pyrroline-5-carboxylate oxidoreductase (TPCOR) to embody both enzyme activities.

Upon encountering a PYCR1 inhibition assay protocol that included TCEP in the human PYCR-mediated reverse direction reaction,[14] we set out to further examine the enzymatic and nonenzymatic reactions between tris(alkyl)phosphine compounds THPP or TCEP and NAD^+ as detailed in chapter five. To that end, our body of evidence of the (NAD^+—tris(alkyl)phosphine) association reaction indicates the following: (i) the chemical reaction kinetics occurs rapidly within one second; (ii) optimal absorbance of the reaction product was observed at 334 nm; (iii) nearly identical observed rate constants, k_{obs}, with four various reaction buffers show that the association reactions are not dependent on the composition of the reaction buffer; and (iv) THPP demonstrates an overall larger apparent association equilibrium constant with NAD^+, K_a^{app}, than compared to TCEP's association with NAD^+ (35.1 ± 2.3 M^{-1} versus 20.1 ± 1.7 M^{-1}). NMR one-dimensional and two-dimensional spectroscopy of the nuclei ^1H, ^{13}C, and ^{31}P collectively resolved the chemical structure of the (NAD^+-tris(alkyl)phosphine) association reaction product molecule as a covalent adduct between the phosphorus of THPP or TCEP interacting at the C4 position of the

dihydronicotinamide ring of NAD^+. All in all, our in vitro findings concerning the (NAD^+—tris(alkyl)phosphine) association reaction serves as a cautionary tale when using TCEP or THPP in NAD^+-dependent enzyme activity assays due to artifactual background increases in absorbance around 340 nm by the reaction product molecule.

FUTURE DIRECTIONS

From chapters two and three, elucidation of the sequential-ordered binding mechanism of HsPYCR1 and HsPYCR2 has the potential to guide the development of new inhibitors and/or substrate analogs as molecular probes for modulating human PYCR activity. For instance, D'Aniello et al. (2020) consider HsPYCR1 to be a potential therapeutic target against cases of hepatocellular carcinoma and breast cancer, but hitherto, no specific enzyme inhibitors have been developed.[15] However, in the context of plants and development of herbicides specifically targeting and inhibiting plant P5CR activity, Forlani et al. (2008) have identified inhibitors with two phosphonic groups as the main structural feature for binding to the P5CR active site.[16] In that study, the authors kept the bisphosphonate scaffold while diligently exploring analogs of the inhibitor (3,5-dichlorophenyl)aminomethylenebisphosphonic acid.[16]

Additionally, previous studies that have profiled metabolic alterations in the blood and plasma of HsPYCR2-deficient patients found no significant decreases in L-proline .[5,17] However, it remains unknown what the concentrations of L-proline and of its related metabolites are in the relevant affected neurological tissue and cerebrospinal fluid (CSF) of these patients. Thus, an appropriate next step would be to examine if HsPYCR2 deficiency causes abnormal L-proline

bioavailability in patients, especially in the CSF.

Upon observing that HsPYCR1 and HsPYCR2 utilize L-T4C as a substrate in chapter four, the next prudent course of action should involve knockout studies of HsPYCR1, HsPYCR2, and of both isozymes combined with L-Pro starvation studies of human tissue cells supplied with doses of L-T4C in growth media. From these studies, the measured endpoints of cellular L-Cys levels and the various redox states of L-Cys could describe how L-Pro homeostasis and L-Cys homeostasis interact at the level of PYCR bifunctional enzyme activity. From early in vivo studies done by Mackenzie et al. (1957), L-T4C was found to be a great sulfur replacement for L-cystine (oxidized form of L-Cys) to supplement animals with low L-methionine diets and promote growth.[18]

Another set of studies could be done to explore if there is altered reactive nitrogen species (RNS) homeostasis with overexpressed HsPYCR1, HsPYCR2, and both isozymes. PYCR enzymes consume L-T4C, which is regarded as a major cellular nitrite scavenger. Taking L-T4C's capacity as a nitrite scavenger and probe for the detection of RNS a step further, Kumagai et al. (2004)'s duodenal contents reflux rat model with the intervention of L-thioproline curtailed pathological tissue damage by the presence of RNS, i.e. nitric oxide and peroxynitrite, and N-nitroso compounds in gastroduodenal reflux contents.[19] Recent advances in imaging methods and visualization tools could allow for specific detection of RNS. For instance, one method relies on an iridium(III) complex used as a near-infrared phosphorescent probe for examining the interplay between nitric oxide and superoxide species and for detecting intracellular peroxynitrite levels of organisms both in vitro and in vivo.[20] Another

novel approach involves the use of a chemiluminescent molecule (oxygen-embedded quinoidal pentacene) tethered to a near-infrared nanoprobe for non-invasive, in vivo, specific detection of peroxynitrite via a chemiluminescence resonance energy transfer mechanism.[21]

Aside from these novel research pursuits, L-proline metabolism is intimately linked with vital cellular processes including bioenergetics, anaplerotic reactions replenishing citric acid cycle intermediates, and cell signaling.[22] The role of PYCR at the intersection of L-Pro and L-Cys homeostasis and the potential involvement of PYCR in RNS balance via L-T4C would further expand our understanding of the numerous physiological roles of PYCR enzymes. From the two major biosynthetic routes of L-proline formation mentioned in chapter one, this work primarily addresses the L-glutamate route with an emphasis on the final reductive step. In conclusion, the entirety of this thesis dissertation accomplishes both structural and kinetic characterization of human PYCR enzymes responsible for L-proline biosynthesis.

REFERENCES

[1] Forlani, G., Makarova, K. S., Ruszkowski, M., Bertazzini, M., and Nocek, B. (2015) Evolution of plant δ(1)-pyrroline-5-carboxylate reductases from phylogenetic and structural perspectives, *Front Plant Sci 6*, 567.

[2] Phang, J. M. (1985) The regulatory functions of proline and pyrroline-5-carboxylic acid, *Curr Top Cell Regul 25*, 91-132.

[3] Adams, E., and Frank, L. (1980) Metabolism of proline and the hydroxyprolines, *Annu Rev Biochem 49*, 1005-1061.

[4] Tanner, J. J. (2008) Structural biology of proline catabolism, *Amino Acids 35*, 719-730.

[5] Nakayama, T., Al-Maawali, A., El-Quessny, M., Rajab, A., Khalil, S., Stoler, Joan M., Tan, W.-H., Nasir, R., Schmitz-Abe, K., Hill, R. S., Partlow, Jennifer N., Al-Saffar, M., Servattalab, S., LaCoursiere, Christopher M.,

Tambunan, Dimira E., Coulter, Michael E., Elhosary, Princess C., Gorski, G., Barkovich, A. J., Markianos, K., Poduri, A., and Mochida, Ganeshwaran H. (2015) Mutations in PYCR2, Encoding Pyrroline-5-Carboxylate Reductase 2, Cause Microcephaly and Hypomyelination, *The American Journal of Human Genetics 96*, 709-719.

[6] Sang, P., Hu, W., Ye, Y.-J., Li, L.-H., Zhang, C., Xie, Y.-H., and Meng, Z.-H. (2017) In silico screening, molecular docking, and molecular dynamics studies of SNP-derived human P5CR mutants, *Journal of Biomolecular Structure and Dynamics 35*, 2441-2453.

[7] Cornish-Bowden, A. (2012) *Fundamentals of enzyme kinetics*, 4th completely rev. and greatly enl. ed., Wiley-VCH, Weinheim.

[8] Yarlett, N., Wu, G., Waters, W. R., Harp, J. A., Wannemuehler, M. J., Morada, M., Athanasopoulos, D., Martinez, M. P., Upton, S. J., and Marton, L. J. (2007) Cryptosporidium parvum spermidine/spermine N1-acetyltransferase exhibits different characteristics from the host enzyme, *Molecular and biochemical parasitology 152*, 170-180.

[9] Inoue, H., Moritani, K., Date, Y., Kohashi, K., and Tsuruta, Y. (1995) Determination of free hydroxyproline and proline in human serum by high-performance liquid chromatography using 4-(5,6-dimethoxy-2-phthalimidinyl)phenylsulfonyl chloride as a pre-column fluorescent labelling reagent, *Analyst 120*, 1141-1145.

[10] Liang, S., Sanchez-Espiridion, B., Xie, H., Ma, J., Wu, X., and Liang, D. (2015) Determination of proline in human serum by a robust LC-MS/MS method: application to identification of human metabolites as candidate biomarkers for esophageal cancer early detection and risk stratification, *Biomed Chromatogr 29*, 570-577.

[11] Yang, H., Yang, T., Baur, J. A., Perez, E., Matsui, T., Carmona, J. J., Lamming, D. W., Souza-Pinto, N. C., Bohr, V. A., Rosenzweig, A., de Cabo, R., Sauve, A. A., and Sinclair, D. A. (2007) Nutrient-sensitive mitochondrial NAD+ levels dictate cell survival, *Cell 130*, 1095-1107.

[12] Lin, S. J., and Guarente, L. (2003) Nicotinamide adenine dinucleotide, a metabolic regulator of transcription, longevity and disease, *Curr Opin Cell Biol 15*, 241-246.

[13] Pollak, N., Dölle, C., and Ziegler, M. (2007) The power to reduce: pyridine nucleotides--small molecules with a multitude of functions, *Biochem J 402*, 205-218.

[14] Grünewald, S., Steckel, M., Husemann, M., Meyer, H., Han, W., and Ding, Z. (2019) Inhibitors and antagonists of human pycr1, Google Patents.

[15] D'Aniello, C., Patriarca, E. J., Phang, J. M., and Minchiotti, G. (2020) Proline Metabolism in Tumor Growth and Metastatic Progression, *Front Oncol 10*, 776.

[16] Forlani, G., Occhipinti, A., Berlicki, L., Dziedzioła, G., Wieczorek, A., and Kafarski, P. (2008) Tailoring the structure of aminobisphosphonates to target plant P5C reductase, *J Agric Food Chem 56*, 3193-3199.

[17] Zaki, M. S., Bhat, G., Sultan, T., Issa, M., Jung, H. J., Dikoglu, E., Selim, L., G. Mahmoud, I., Abdel-Hamid, M. S., and Abdel-Salam, G. (2016) PYCR2 mutations cause a lethal syndrome of microcephaly and failure to thrive, *Annals of neurology 80*, 59-70.

[18] MACKENZIE, C. G., and HARRIS, J. (1957) N-formylcysteine synthesis in mitochondria from formaldehyde and L-cysteine via thiazolidinecarboxylic acid, *J Biol Chem 227*, 393-406.

[19] Kumagai, H., Mukaisho, K., Sugihara, H., Miwa, K., Yamamoto, G., and Hattori, T. (2004) Thioproline inhibits development of esophageal adenocarcinoma induced by gastroduodenal reflux in rats, *Carcinogenesis 25*, 723-727.

[20] Wu, W., Zhang, C., Rees, T. W., Liao, X., Yan, X., Chen, Y., Ji, L., and Chao, H. (2020) Lysosome-Targeting Iridium(III) Probe with Near-Infrared Emission for the Visualization of NO/O, *Anal Chem 92*, 6003-6009.

[21] Wang, B., Wang, Y., Wang, Y., Zhao, Y., Yang, C., Zeng, Z., Huan, S., Song, G., and Zhang, X. (2020) Oxygen-Embedded Pentacene Based Near-Infrared Chemiluminescent Nanoprobe for Highly Selective and Sensitive Visualization of Peroxynitrite In Vivo, *Analytical Chemistry 92*, 4154-4163.

[22] Phang, J. M. (2019) Proline Metabolism in Cell Regulation and Cancer Biology: Recent Advances and Hypotheses, *Antioxid Redox Signal 30*, 635-649.

APPENDIX A

DL-P5C Substrate Stocks' Chemical Synthesis Protocol

DL-P5C Synthesis

The synthesis of DL-P5C followed the method of Williams and Frank[1] except the volume of each of the following components was reduced by two-fold: DL-5-hydroxylysine hydrochloride, sodium metaperiodate, glycerol, glycine, and HCl. After performing the reaction at 4 °C, the reaction mixture was loaded onto a 1.5 cm (inner diameter) x 43.5 cm (length) borosilicate glass column (Kimble Chase) packed with Dowex 50WX4 cation exchange resin that had been equilibrated with 2 M HCl. The column was then washed with 1 M HCl to elute the fractions. The concentration of DL-P5C in the collected fractions was determined by diluting a 4 µl sample of each fraction into 16 µl of 1 M HCl which was then added to 180 µl of 5 mM *o*-AB (prepared by diluting a 500 mM *o*-AB stock (in 100% ethanol) into 20 mM Glycine-HCl, pH 2.0), resulting in a final 200 µl volume. DL-P5C reacts with *o*-AB to form a yellow conjugate that can be detected at 443 nm (ε_{443} = 2590 M^{-1} cm^{-1}).[2] The DL-P5C/ *o*-AB mixtures (200 µl) were incubated at room temperature with mild shaker agitation for 24 h in a clear polystyrene 96-well flat bottom plate (Corning) covered in aluminum foil. Absorbance at 443 nm was then recorded using a Synergy 2 Multi-Mode Plate-Reader (BioTek) with *Gen5 Secure Reader Control and Data Analysis software (version 2.05.5, BioTek)*. The concentration of DL-P5C was determined using a modified equation of the Beer-Lambert-Bouguer law[3,4,5] which incorporates the mean absorbance of six replicates of a blank (5 mM *o*-AB in 20 mM Glycine-HCl, pH 2.0), a microplate-based path length-well volume correction factor (2.19) determined from IR absorbance

measurements[6] with 1 M HCl, and a dilution factor of 50-fold. Eluted fractions of DL-P5C in 1 M HCl were kept long-term as stock solutions at 4 °C.

$$[\text{DL-P5C}]\ (\text{mM}) = \left(\frac{((\text{sample mean } A_{443} - \text{blank mean } A_{443}) \times 2.19)}{(\varepsilon_{443\ \text{nm}} = 2.590\ \text{mM}^{-1}\ \text{cm}^{-1}) \times (1\ \text{cm})}\right) \times 50\ (\text{dilution factor})$$

Characterization of DL-P5C by Electrospray Ionization Mass Spectrometry

Liquid chromatography-electrospray ionization-multiple reaction monitoring (LC-ESI-MRM) mass spectrometry analysis was performed to verify the presence of DL-P5C in the samples. The LC-ESI-MRM analysis was performed on a 4000 QTrap from Sciex (Framingham, MA) operating in MRM analysis mode. The electrospray source was optimized for positive mode with the following parameters: declustering potential = 40 V, curtain gas = 30 L/min, ionization potential = 5500 V, temperature = 600 °C, ion source gas 1 = 60 and ion source gas 2 = 80. The samples were loaded into sample vials and held at 5 °C until the injection time. An Agilent LC 1200 HPLC system was used for the separation of the compounds, using a Waters X-Bridge Amide column (Waltham, MA) with dimensions of 4.6 mm x 100 mm. The flow rate was maintained at 0.5 mL/min with the gradient as follows: from 0 to 2 min 5% mobile phase A (20 mM ammonium acetate, 20 mM NH_4OH, pH = 9.5) and 95% mobile phase B (acetonitrile); from 2 to 20 min from 5% to 70% A, at 20.2 min 95% A, at 24 min 95% A, and at 24.2 min 5% A for 16 min duration for re-equilibration purposes.

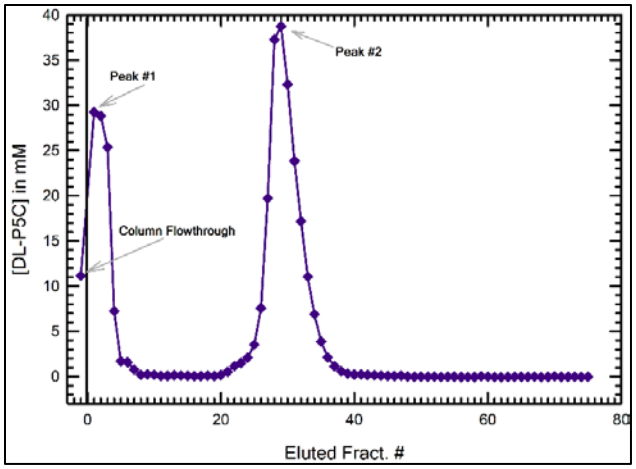

A

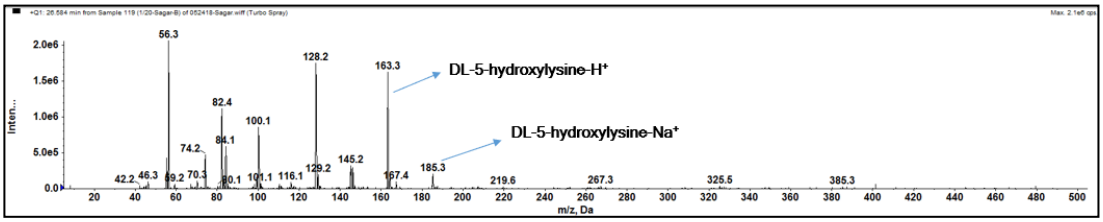

B

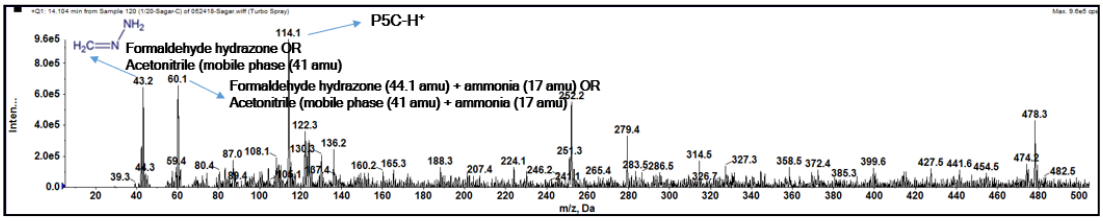

C

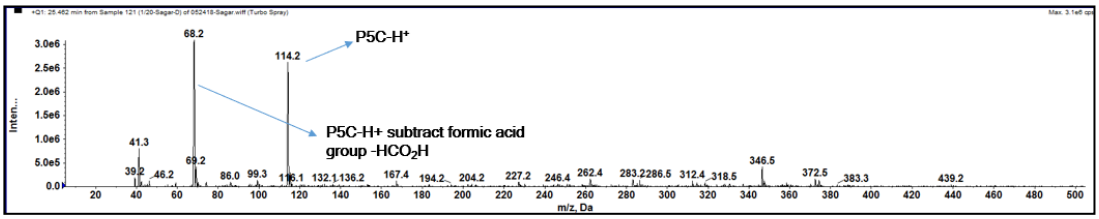

Appendix A Figure 1. Microplate-based DL-P5C concentration determinations and mass spectrometry analysis. The scatter plot summarizes microplate-based DL-P5C concentration determinations via *o*-AB colorimetric assay of absorbance measurements at 443 nm of one batch of chemically synthesized DL-P5C substrate in column eluted fractions. Then, liquid chromatography-mass spectrometry analysis was performed on three samples, prepared as (1/100) dilutions using acetonitrile solvent, from those eluted fractions as annotated in the scatter plot: (A) Column Wash Flowthrough sample, (B) Elution Peak #1 sample, and (C) Elution Peak #2 sample.

REFERENCES

[1] Williams, I., and Frank, L. (1975) Improved chemical synthesis and enzymatic assay of delta-1-pyrroline-5-carboxylic acid, *Anal Biochem 64*, 85-97.

[2] Mezl, V. A., and Knox, W. E. (1976) Properties and analysis of a stable derivative of pyrroline-5-carboxylic acid for use in metabolic studies, *Anal Biochem 74*, 430-440.

[3] Beer. (1852) Bestimmung der Absorption des rothen Lichts in farbigen Flüssigkeiten, *Annalen der Physik 162*, 78-88.

[4] Lambert, J. H., and Klett, E. (1760) *Photometria sive de mensura et gradibus luminis, colorum et umbrae*, Klett.

[5] Bouguer, P. (1729) *Essai d'optique sur la gradation de la lumière*, chez Claude Jombert, ruë S. Jacques, au coin de la ruë des Mathurins, à l ….

[6] (2015) Microplate-Based Pathlength Correction Method for Photometric DNA Quantification Assay, SP&A Application Laboratory, Thermo Fisher Scientific Inc., Vantaa, Finland.

APPENDIX B

Extended Methods and Procedure for HsPYCR2 Protein Purification

Recombinant protein expression (pKA8H/PYCR2) vector DNA constructs were first transformed into DNA propagation host *E. coli* XL1-Blue Supercompetent Cells (Agilent Technologies), which were grown on separate LB Agar Miller plates containing 50 µg/ml ampicillin. Then, the recombinant protein expression pKA8H vector DNA constructs were transformed into protein expression host *E. coli* BL21 (DE3) pLysS competent cells (Novagen-EMD Millipore Sigma), which were likewise grown on separate LB Agar Miller plates containing 50 µg/ml ampicillin and 34 µg/ml chloramphenicol (Chem-Impex International). Using this pKA8H expression vector construct resulted in proteins with an N-terminal octahistidine tag followed by a tobacco etch virus protease cleavage site.

Next, from those latter growth plates, a pipette-tip picked single colony of cells was inoculated into 15 ml starter liquid growth culture containing TB liquid media (prepared from the recipe in Sambrook et al. 1989 consisting of tryptone, yeast extract, glycerol, and water),[1] 50 µg/ml ampicillin, and 34 µg/ml chloramphenicol. Then starter culture was grown for 17 h overnight in an incubator-shaker at 37 °C, 180 rpm. To scale up culture size, we transferred 2.5 ml starter culture into each of six 2 L flasks containing 1 L of TB liquid media and 50 µg/ml ampicillin to shake at 37 °C, 180 rpm, until reaching nearly synchronized cell densities associated with $OD_{600} \approx 0.8\text{-}1.0$. At that point, the incubation temperature was lowered to 18 °C and the six flasks of culture were induced with 0.4 mM IPTG for cultures shaken at 180 rpm for 10 h. Then, we added 100 µg/ml chloramphenicol

to the six flasks of culture to be continued shaken at 180 rpm and 18 °C for 2 additional hours to arrest ribosomal translation of bacterial proteins to further improve the solubility of the target overexpressed recombinant protein by means of affording the bacterial cells to divert their chaperone-assisted folding capabilities towards the target protein without continuous generation of aggregation-prone proteins.[2]

Next, we harvested cells via repeated rounds of large rotor centrifugation (Avanti J-E High-Speed Centrifuge, Beckman Coulter) at relative centrifugal force (5400 x g) for 20 min at 4 °C to process all 6 L of culture into two 1000-ml centrifugation polypropylene bottles (Beckman Coulter), with supernatants decanted off and cell pellets stored at -80 °C overnight to promote cell lysis by freezing. Then with a metal spatula, we transferred cell pellets from both centrifugation bottles into a common glass beaker and let pellets thaw at room temperature on the lab countertop for 30 min. Next, the combined cell pellets were resuspended and lysed in NPI-5 cell lysis buffer (5 mM imidazole, 500 mM NaCl, 50 mM NaH_2PO_4, pH 7.5) with the addition of 500 µM Tris(3-hydroxypropyl)phosphine (THPP) reducing agent (Strem Chemicals), 0.01% TritonX-100 detergent (Amresco), 0.01% Brij-35 polyoxyethylene detergent (Santa-Cruz Biotechnology), 10 mM βOG, and a mixture of five protease inhibitors: (i) 500 mM ε-amino-N-caproic acid dissolved in water, (ii) 50 mM PMSF dissolved in acetone, (iii) 2 mM leupeptin hemisulfate dissolved in water, (iv) 8 mM N-tosyl-L-phenylalanine chloromethyl ketone dissolved in ethanol, and (v) 13 mM N-α-p-tosyl-L-lysine chloromethyl ketone (Bachem) dissolved in water. The cell suspension was then subjected to sonication at knob setting 6 for total

processing time of 5 min with settings 5 s-pulse on and 15 s-pulse off, on a Sonic Dismembrator (Model F 550, Fisher Scientific). Next, cell lysates were poured into four 25 ml-centrifugation tubes fitted with stoppers and caps, to be subjected to small rotor 4 °C centrifugation at relative centrifugal force (30960 x g) for 1.5 hr before obtaining supernatants of target protein solution.

After that, the target protein was purified by application into a borosilicate glass column (Kimble Chase) of 2.5 cm (diam.) x 24 cm (height) packed with 25-ml resin bed of Ni^{2+}-nitrilotriacetic acid Superflow resin (Qiagen) for motor-driven pulsatile tubing flow-immobilized metal affinity column chromatography in 4 °C cold room. The column purification proceeded with column volumes (CV) of an increasing imidazole concentration gradient (5 CV of 5 mM → 10 CV of 60 mM → 6 CV of 500 mM imidazole) of 50 mM NaH_2PO_4-based buffers applied into column until final protein elution into automated glass test tube fraction collector set at 2 ml per fraction. Next, Bio-Safe Coomassie Blue G250 Stain (Bio-Rad) exposure-based SDS-PAGE of two precast 15-well gels 4-20 % Tris/Gly (Bio-Rad, Mini-Protean TGX) was performed with 20 µl-aliquots of 20 eluted fraction tubes chosen randomly from 50 total tubes, where each aliquot was chemically reduced with SDS-Loading Buffer and (β)2-Mercaptoethanol (Acros Organics) and thermally reduced by 10 min boil at 100 °C, all ultimately to determine which eluted protein fractions to pool together. Next, in 4 °C cold room, the pooled protein fractions were collected into a regenerated cellulose dialysis tubing sac (Dialysis Snakeskin Tubing, ThermoFisher Scientific-Pierce Biotech) clipped closed at both ends and dialyzed at moderate stir atop stirring plate for three separate periods (24 hr→5 hr→5 hr) into fresh 1 L dialysis buffer (50 mM HEPES,

250 mM NaCl, 0.5 mM EDTA, 500 µM THPP reducing agent, 10% (v/v) glycerol, pH 7.5).

Then, we performed two methods of protein concentration: initially concentrating the large volume of dialyzed protein in 4 °C cold room using 5 kDa PLCC low bind 44.5 mm diameter ultrafiltration disc (EMD Millipore-Sigma) with an ultrafiltration stirrer cell (Model 8050, Amicon, EMD Millipore-Sigma) under airflow $N_{2(g)}$-pressure until approximately 5 ml concentrated protein obtained, and if protein appeared visibly free of any aggregates/precipitates, then prepared 1 ml-aliquots in 2 ml microtubes that are shock-frozen in liquid nitrogen followed by piercing tube lids with a fine needle and subjecting them to stand in a tube holder for freeze-dry vacuum lyophilization (FreeZone Bulk Tray Dryer, Labconco) carried out 3-5 h until approximately 250 µl concentrated protein remained in microtubes. For these lyophilized microtube samples, we subjected them to microdialysis in 4 °C cold room with inverted 15K MWCO Tube-O-Dialyzer tubes (G Biosciences-Geno Technology) at moderate stir atop stirring plate for three separate periods (24 hr→5 hr→5 hr) into fresh 500 ml dialysis buffer. Protein concentration was quantified by 660 nm Pierce Protein Dye Assay (ThermoFisher Scientific-Pierce Biotech) with bovine serum albumin standards' curve prepared by spectrophotometric measurements using 1 cm-path length 1.5 ml polystyrene cuvettes (USA Scientific) with a Varian Cary Bio 50 UV-Vis Spectrophotometer (Agilent Technologies). At this point, all protein samples were distributed into 500 µl aliquots that were shock-frozen in liquid nitrogen and stored at -80 °C. Samples of purified wild-type, R251C mutant, and R119C mutant enzymes were subjected to SDS-PAGE under reducing conditions and visualized all together on

a Bio-Safe Coomassie Blue G250-stained 4-20% gradient precast polyacrylamide-Tris-Gly HCl, 10-well MP TGX gel (Fig. 3.2).

REFERENCES

[1] Sambrook, J., Fritsch, E. F., and Maniatis, T. (1989) *Molecular cloning: a laboratory manual*, Cold spring harbor laboratory press.

[2] de Marco, A., Deuerling, E., Mogk, A., Tomoyasu, T., and Bukau, B. (2007) Chaperone-based procedure to increase yields of soluble recombinant proteins produced in E. coli, *BMC Biotechnol 7*, 32.